nature catalysis

Supplementary information

https://doi.org/10.1038/s41929-026-01609-5

Unlocking reaction pathways for CO_2 and CO electrocatalytic reduction to C_{3+} hydrocarbons and oxygenates using plasma activation

In the format provided by the authors and unedited

Table of contents

Supplementary notes	2
Design of plasma-electrocatalytic conversion	11
Plasma-electrocatalytic CO_2 conversion	16
Influence of plasma on electrolyzer feed gas and catalysts	21
Plasma-electrocatalytic CO conversion	34
Plasma-electrocatalytic CO_2+CO conversion	41
Plasma diagnostics and kinetic simulations	54
Reaction mechanisms study	69
Supplementary Tables	80
Supplementary References	86

Supplementary Note 1: Design of electrocatalytic reduction of plasma-activated CO_2 or CO

The Cu catalyst layer on the GDE was positioned on the side opposite to the plasma activation region of the polytetrafluoroethylene (PTFE) membrane, thereby avoiding direct exposure of the catalyst to the plasma and minimizing plasma-induced changes to the catalyst structure. The hydrophobic GDE prevents crossover of water into the plasma zone, enabling hydrogenation reactions to occur only through electrocatalysis and not in the plasma region, which contains only CO_x and He.

Supplementary Note 2: Plasma-induced CO_2 dissociation and its impact on electrocatalysis

The decrease in CO and O_2 generation with increasing plasma power might be attributed to more filamentary plasma characteristics, such that lower fractions of the feed gas are treated by plasma. Hydrocarbons and oxygenates were not observed in the plasma effluent, which is consistent with the lack of supply of H-containing reactants to the plasma tube (i.e., water from the electrolyte does not diffuse through the GDE into the plasma region).

The plasma reaction products can affect the electrocatalytic reaction, particularly since the reduction of O_2 (equation (1)) is thermodynamically favored compared to CO_2RR as shown in equations (2-5). Given that metallic Cu also has O_2 reduction reaction (ORR) activity, the reduction of O_2 to H_2O competes with CO_2RR.[1,2]

$$O_2 + 4H^+ + 4e^- = 2H_2O \ (E_0 = 1.230 \text{ V}) \quad (1)$$

$$CO_2 + 2H^+ + 2e^- = CO + H_2O \ (E_0 = -0.106 \text{ V}) \quad (2)$$

$$CO_2 + 8H^+ + 8e^- = CH_4 + 2H_2O \ (E_0 = 0.169 \text{ V}) \quad (3)$$

$$2CO_2 + 12H^+ + 12e^- = C_2H_4 + 4H_2O \ (E_0 = 0.064 \text{ V}) \quad (4)$$

$$2CO_2 + 12H^+ + 12e^- = C_2H_5OH + 3H_2O \ (E_0 = 0.084 \text{ V}) \quad (5)$$

The charge consumption due to ORR was estimated by comparing the amount of O_2 in the CO_2 plasma effulent with that in the plasma-coupled electrocatalysis effluent, assuming that all O_2 was electrochemically reduced to H_2O, not H_2O_2 (**Fig. 3c** and **Supplementary Fig. 11c**).

Supplementary Note 3: Electrocatalytic reduction of a mixed CO_2+CO feed

In previous work, electrocatalytic reduction of a mixed CO_2 + CO feed that simulated flue gas was reported to outperform pure CO_2 conversion to multi-carbon products.[3,4] However, these studies focused on enhancing the generation of C_2H_4. To the best of our knowledge, there have been no reports on a mixed CO_2+CO feed demonstrating either an expanded product spectrum or enhanced C_{3+} product formation.

Practically, co-feeding CO_2 and CO could be achieved by optimizing an upstream CO_2 reduction process to generate CO in the desired ratio, such as through a plasma or thermocatalytic reverse water gas shift reaction or via electrocatalytic CO_2 reduction to CO. Mixtures of CO_2 and CO may also be obtained directly from certain flue gas sources.[5] Alternatively, strategies to remove O_2 from a CO_2 plasma could be employed, e.g., by using a post-plasma carbon bed,[6,7] to attain an O_2-free gas for electrocatalysis. By engineering the plasma process to enhance selectivity, the formation of O_2 byproducts could be suppressed while promoting activation toward specific plasma species. Although several potential strategies could be employed to obtain a CO_2 or CO feed practically, the results herein demonstrate the significant enhancement in the generation of C_{3+} hydrocarbons and oxygenates during CO_2 or CO plasma-electrocatalysis.

Supplementary Note 4: Plasma kinetic simulations

Plasma kinetic modeling enabled identification of potential reactive chemical species, such as vibrational and electronic excitation modes and ground state reactive species. The experimental setup

and modeling were linked via the plug flow reactor approximation, with microdischarge filaments represented as a series of temporal pulses.[8] This approach simplified the generation and relaxation of species, providing qualitative analysis and hypothesizing the effects of plasma activation on electrocatalysis.

The parameters such as reduced electric field, current, and electron temperature govern electron kinetics and the consequent excitation of heavy particles. Vibrational excitation was studied in this context because it facilitated dissociation of CO_2 via lower energy barriers compared to other pathways.[9] Vibrational excitation, which leads to vibrational-translational (V-T) non-equilibrium, where vibrational temperatures exceed gas (translational-rotational) temperatures, can also enhance surface reaction rates. For example, while excitation of the lowest-energy vibrational states may be insufficient to trigger homogeneous gas-phase reactions, such excited molecules may encounter significantly reduced dissociation barriers on catalytic surfaces.[10]

Although the model for plasma kinetic simulations was validated for low-pressure conditions,[11] its applicability was extended to atmospheric pressure in this study by including three-body reactions between neutral species, interactions with charged particles, and three-body electron-ion recombination. The inclusion of electron-ion recombination was particularly crucial for the stability of the simulations, as their absence would result in an unreasonably high ionization degree (approaching 10%) under the studied conditions. Moreover, despite the significant pressure difference between the previous study (6.7 mbar) and this study (1 bar), both discharges operated in a non-thermal regime where thermal chemistry held limited influence. Consequently, while thermal processes were included in the kinetic scheme, the lack of model validation for conditions involving substantial gas heating was not a limiting factor. In addition, both discharges exhibited only mild vibrational-translational non-equilibrium, ensuring the validity of the assumptions and scaling laws used in previous work.[11]

The set of vibrational relaxation rates used in the vibrational energy balance equations was adopted from previous work.[11] Moreover, vibrational deactivation of CO by collisions with helium atoms was included based on the rates reported by Billing and Cacciatore,[12] with a rate coefficient of 1.66×10^{-24}

$e^{(35.48 - 157*T_g^{1/3} + 193*T_g^{2/3})}$ cm^3/s. Transitions involving higher vibrational levels (up to level 5) were scaled according to the Schwartz–Slawsky–Herzfeld (SSH) theory.[13]

The detailed chemical kinetics were modified and added considering electron-impact processes (**Supplementary Table 5**). The formation of solid carbon in the gas-phase was included,[14] while the carbon surface reaction scheme was taken from previous research.[15] Reverse rates were computed from the detailed balance principle, with enthalpy and entropy as function of temperature for each species taken from the NASA polynomials.[16]

The simulation domain was obtained by dividing the reactor into slices, each corresponding to the width of a single microdischarge (2 mm), based on estimates from similar conditions.[17] The input flow rate for the simulations was calculated using equation (6).

$$Q_{slice} = Q_{tot} \times \frac{V_{slice}}{V_{tot}} \quad (6)$$

where Q_{slice} is the flow rate for a single slice, Q_{tot} is the total flow rate, and V_{slice} and V_{tot} represent the volume of a single slice and the total reactor volume, respectively.

The time between consecutive microdischarges within the same reactor slice was derived from the microdischarge frequency f_{MD} and the gas residence time (t_{res}) inside the plasma zone. The total number of microdischarges a gas volume experiences was given by equation (7).

$$N_{MD,total} = f_{MD} \times t_{plasma\ on} \quad (7)$$

where $t_{plasma\ on}$ is the total plasma-on time per second. The number of microdischarges per slice is calculated by equation (8).

$$N_{MD,slice} = \frac{N_{MD,total}}{N_{slices}} \quad (8)$$

where N_{slices} is the number of slices in the reactor. The time between two consecutive microdischarges within a slice is then given by equation (9).

$$t_{between\ MD} = t_{res}/N_{MD,\ slice} \quad (9)$$

Using the reactor geometry (12 cm plasma zone, 1 cm tube inner diameter), N_{slices}= 31.4, and based on the gas residence time (t_{res} = 9.5 s), the calculated time between microdischarges was approximately 1×10^{-4} s. These numbers are kept the same for all conditions investigated, as the microdischarge frequency remains nearly constant.

The power input during $t_{plasma\ on}$ was calculated from the charge per microdischarge q_{MD} and the applied voltage U_{MD} (equation 10):

$$P_{MD} = (q_{MD} \times U_{MD})/t_{MD,lifetime} \quad (10)$$

where $t_{MD,lifetime}$ was the microdischarge duration, which was set to 15 ns based on estimates from for similar conditions.[18] The power density was obtained by dividing the power input by the microdischarge volume, calculated assuming a cylindrical shape, and was then used as input parameter for the model.

To mimic plug flow behavior, a continuous stirred-tank reactor (CSTR) model without inflow and outflow terms was employed. This approximation captured the effects of plasma-induced reactions within the reactor slices.

Supplementary Note 5: Reactivity of carbon suboxide (C_3O_2)

C_3O_2 has been used as a precursor to C_3H_6 and C_3H_8 in catalytic hydrogenation due to its high reactivity.[19,20] In addition, C_3O_2 has been reported to spontaneously polymerize at room temperature.[21] Solids with chemical composition similar to C_3O_2 polymers formed from the monomer were also detected in an atmospheric pressure CO plasma.[22]

Supplementary Note 6: *In situ* Raman control experiments using plasma-activated He, CO_2, or CO

While feeding plasma-activated He, H_2 from HER was the only detected product; accordingly, no peaks were observed in the Raman spectrum. This result confirms that plasma activation in the absence of carbon-containing gases cannot generate any CO_2RR or CORR intermediates on the Cu surface and that the observed *in situ* Raman signals did not originate from plasma-induced artifacts or decomposition of the reactor or electrode components (**Supplementary Fig. 62**). In *in situ* Raman spectra obtained during plasma-activated CO_2RR (**Supplementary Fig. 63**), reaction intermediates corresponding to *CHO and *(H)OCCOH were observed with enhanced intensities compared to plasma-activated CO_2+CO reduction, supporting promoted CO_2 activation and enhanced C-C coupling to multi-carbon products. Raman spectra collected under plasma-activated CO_2 electrocatalysis also exhibited Cu oxide peaks over a wider potential range, which can be attributed to the presence of O_2 derived from CO_2 plasma splitting. This experiment also showed higher J than plasma-activated CO_2+CO reduction (**Supplementary Fig. 61**), which resulted in significant bubble formation on the Cu surface and limited the collection of Raman measurements at more negative potentials. *In situ* Raman spectra were also collected during plasma-activated CORR (**Supplementary Fig. 64**), showing signals corresponding to $*CO_{rotation}$, *CHO, *(H)OCCOH, and $*CO_{atop}$, and providing further mechanistic insights when compared with plasma-activated CO_2+CO. Reaction intermediates such as *(COOH), *COH, and *OC were observed under CO_2+CO conditions but were absent with CO only, suggesting that these species are generated through CO_2-derived pathways. In contrast, $*CO_{atop}$ intermediates exhibited stronger intensities in plasma-activated CORR, implying that they are associated with CO-derived pathways. However, C deposition in plasma-activated CORR caused unstable and inhomogeneous plasma, as described earlier.

Supplementary Note 7: Considerations for plasma kinetic simulation results

The absolute quantities reported from simulation results may not reflect those of the real system, although we expect the trends—e.g., that vibrationally excited CO exhibits a longer lifetime than vibrationally excited CO_2—to be accurate. Considering that our modeling was based on 0-dimensional

or pseudo-1-dimensional approximations, species spatial evolution, distribution, and mass transport in plasma activation processes were not considered. Moreover, the enhanced peak intensities corresponding to *CHO, *COH, and *(H)OCCOH intermediates observed in *in situ* Raman analysis cannot be adequately explained if C_3O_2 generated through plasma activation is assumed to be the only plasma species that reaches the electrocatalyst. For the enhancement of these intermediates, C_3O_2-derived species would need to decompose and subsequently adsorb onto the catalyst surface; however, such a process is less likely given the intrinsic reactivity and polymerization tendency of C_3O_2.[21] In addition, the enhanced formation of these surface species was similarly observed in plasma-activated CORR and plasma-activated CO_2RR, whereas for the latter the formation of C_3O_2 was predicted to be negligible in the simulation. Taken together, these observations suggest that plasma species other than C_3O_2 are involved in the electrocatalytic reactions on Cu surface.

Supplementary Note 8: Economic feasibility and future perspectives for plasma-electrocatalysis

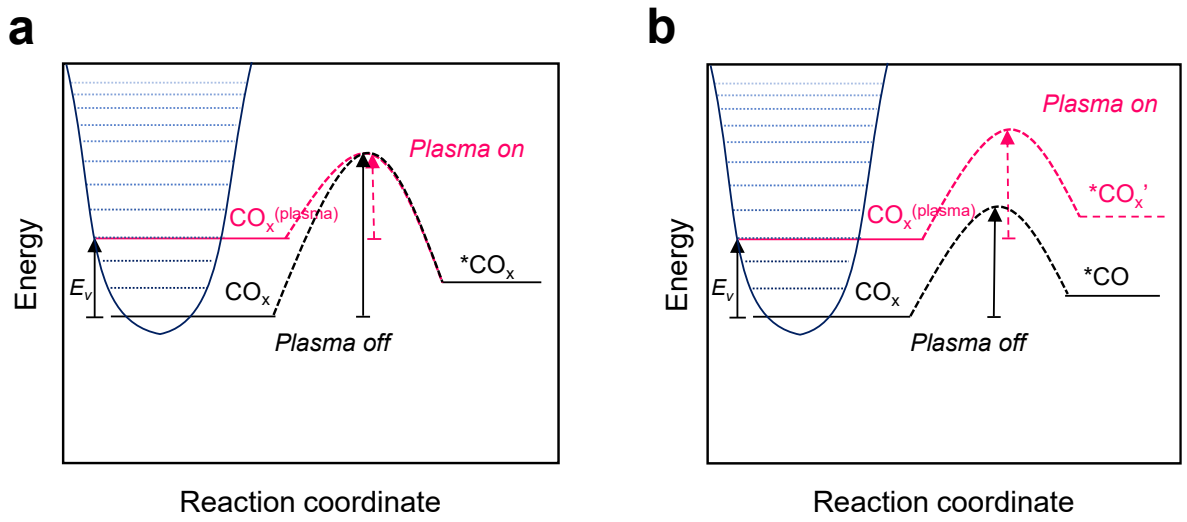
We evaluated the energy consumption per unit product (C_2H_5OH and C_3H_7OH) for plasma-coupled electrocatalysis compared to conventional electrocatalysis to provide preliminary assessment of economic feasibility (**Supplementary Fig. 65**). The analysis suggests that, for both products, even modest improvement in overall energy efficiency of product generation would justify a substantial amount of energy consumption from plasma activation. For example, if the current energy efficiency of CO_2-to-C_2H_5OH electrocatalysis (~20%) could be improved to 30% by coupling with plasma activation, an additional energy consumption of up to 1.53 MJ mol^{-1} would be justifiable. This trend is even more pronounced for C_3H_7OH: improving the overall energy efficiency from the current level of ~10% to 20% would justify an additional energy consumption of up to 6.37 MJ mol^{-1}. In other words, because current electrocatalytic CO_2-to-multicarbon products conversion processes already consume substantial energy due to limited energy efficiency and high thermodynamic energy requirements, achieving an improvement in energy efficiency via plasma activation can render the associated energy overhead acceptable. Therefore, pre-activating CO_2 or CO by plasma can provide a compelling strategy to

improve production rates for C_{3+} hydrocarbons and oxygenates, rather than feeding pure CO or modifying catalytic active sites through high-cost strategies such as alloying with noble metals, surface engineering, and composites. Overall, enhancing the conversion toward total liquid products such as alcohols can provide substantial economic and technological advantages,[23] as these products not only possess high market value but also exhibit high energy density, making them suitable for storage and transportation in a final mixed liquid product stream.[24] Liquid products can be readily condensed from the post-conversion gas stream, which can reduce separation costs.[25]

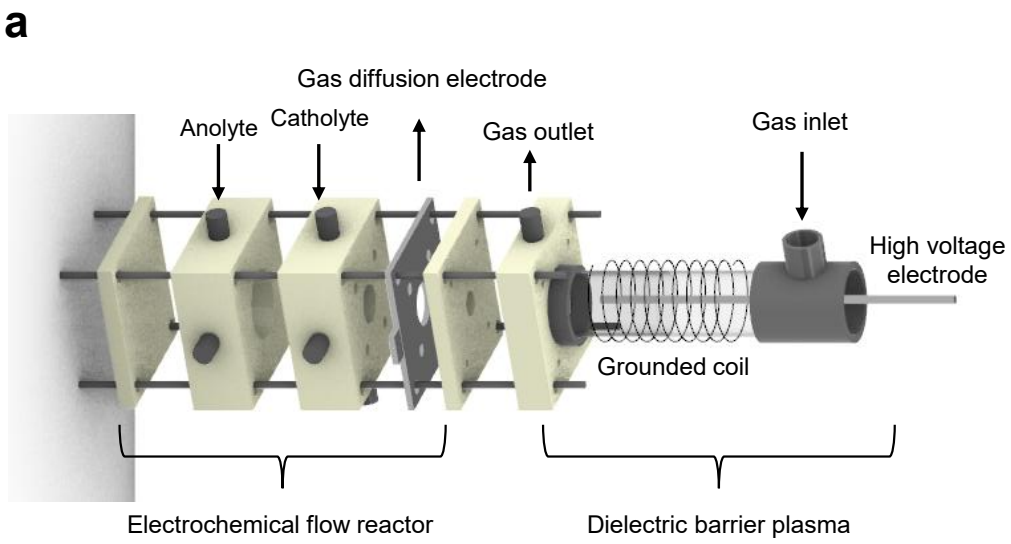
The demonstration of a plasma-electrocatalytic CO_2 reduction process reported herein illustrates the possibilities for one-step and rapid synthesis of a range of multi-carbon products, but vast unexplored directions remain to improve the product selectivity, product generation rates, and energy efficiency. For example, both plasma and electrocatalytic components can be tuned separately: The plasma activation process can be engineered to control the selectivity and formation rate of activated states and to optimize energy consumption (**Supplementary Fig. 66**). To illustrate the substantial enhancement possibilities, we find that reducing the discharge gap from 3 mm to 1 mm lowers power consumption from 46.9 W to 1.4 W, while still achieving similar enhancement in alcohols generation (**Supplementary Fig. 67**). Beyond DBD plasmas, other plasma types designed to target generation of species that can be utilized by electrocatalytic reduction may enable greater overall efficiency, such as gliding arc or microwave plasma for vibrationally excited species generation. Concurrently, electrocatalyst design strategies can focus on efficient reduction of oxidized C-C coupled species derived from C_3O_2. Catalyst properties can be tailored through alloying or structural modification to enhance hydrogenation activity rather than CO adsorption strength, or to tune binding affinities optimized for plasma-generated species including vibrationally excited CO_2 or CO molecules.

Fundamental understanding of the plasma-electrocatalyst coupling will reveal ways to further optimize and control the product generation pathways. Comprehensive investigations may tune the reactions toward specific desired products and gain additional insight into the coupling mechanisms through catalyst design, modification of the porous characteristics of the GDE, developing methods to improve

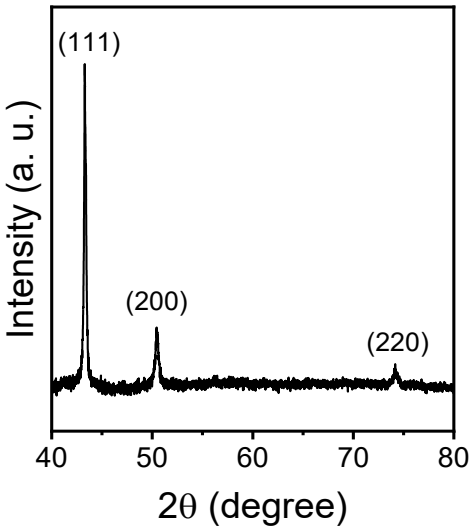
198 *in situ* characterization during plasma-electrocatalysis, and manipulating the plasma chemistry and
199 physics.



Supplementary Fig. 1 | **a-b**, Schematic reaction diagram comparing activation energy barrier for CO_2/CO conversion pathways starting from ground or plasma-activated states. (**a**) Ground and plasma-activated CO_x were activated to $*CO_x$ state, adsorbing on catalyst surface. (**b**) Ground and plasma-activated CO_x were activated to different energy states.



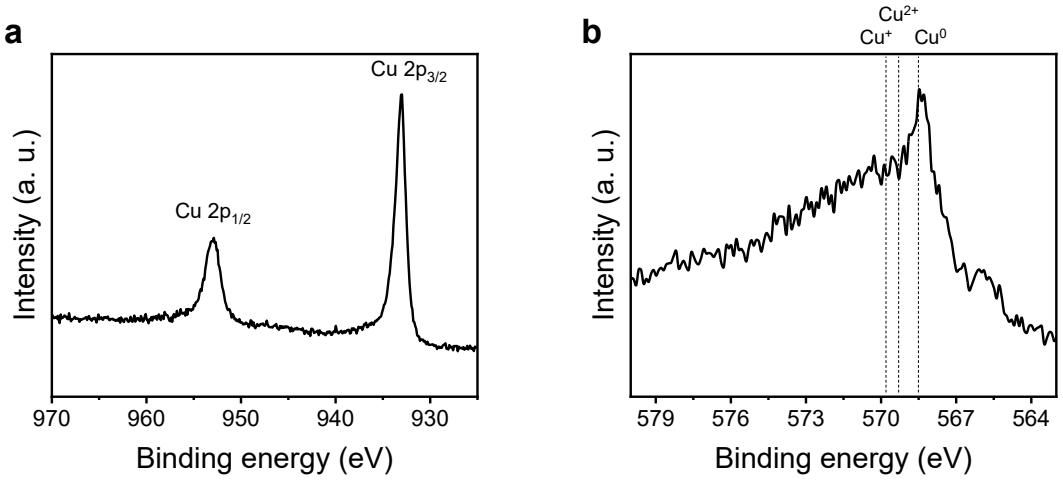
Supplementary Fig. 2 | **a-b**, (**a**) Schematic illustration and (**b**) photograph of the plasma-electrocatalysis combined flow reactor for CO_2/CO conversion.



211

212 **Supplementary Fig. 3** | XRD analysis of Cu phase in as-prepared gas diffusion electrode (GDE).
213 Metallic Cu film with 400 nm thickness was deposited at a rate of 0.2 nm sec^{-1}.

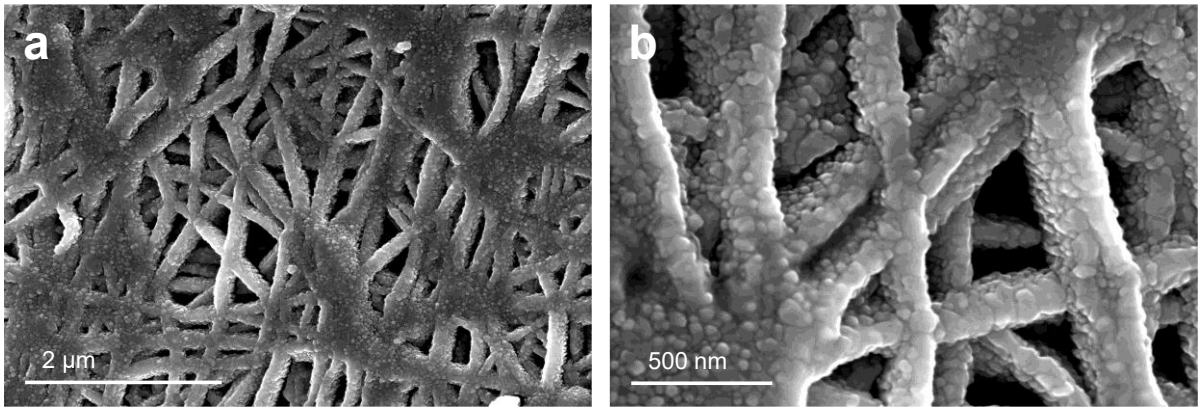
214



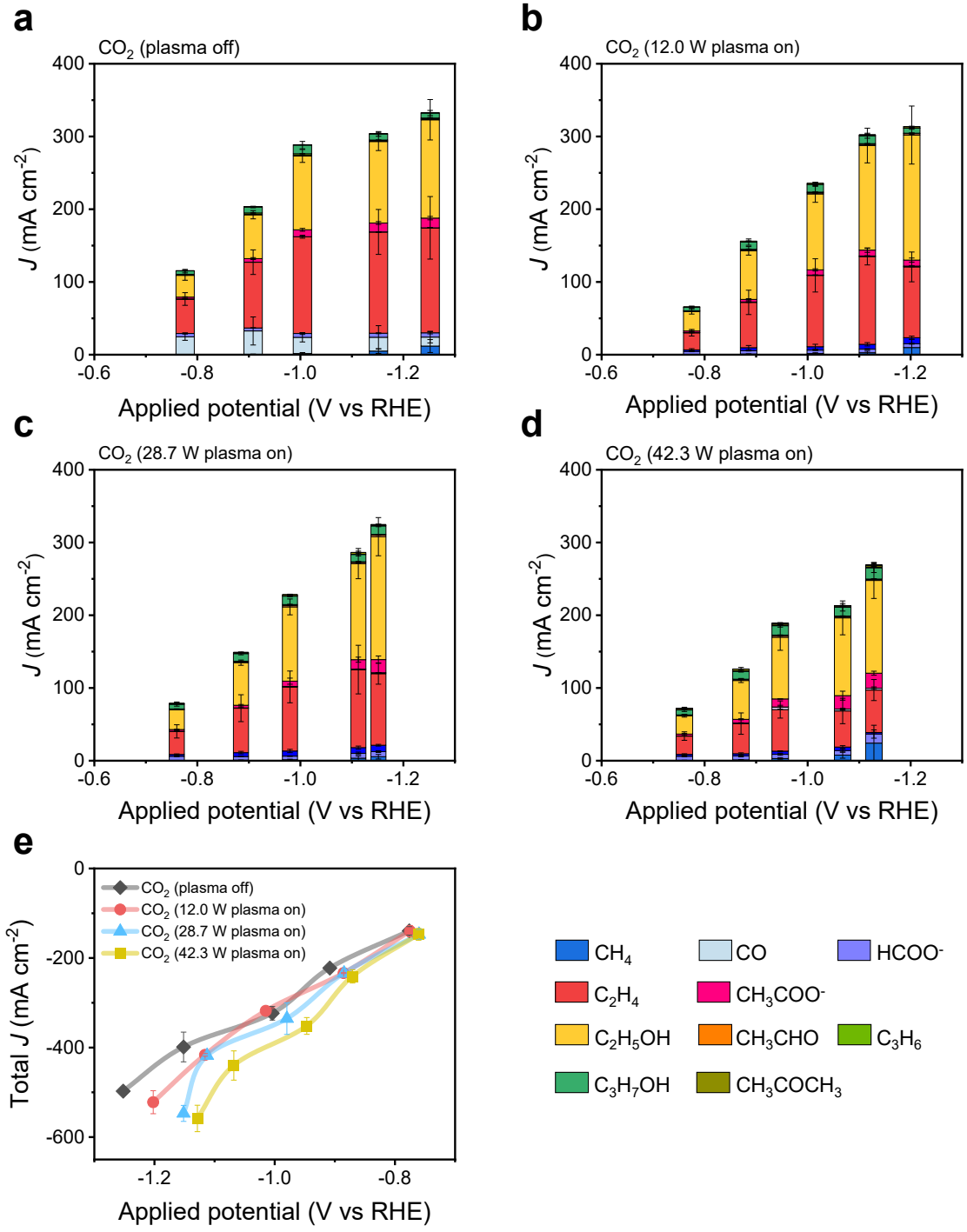
215

216 **Supplementary Fig. 4 | a-b,** XPS analysis of Cu oxidation states in as-prepared GDE. Metallic Cu film
217 with 400 nm thickness was deposited at a rate of 0.2 nm sec^{-1}. (**a**) Cu 2p and (**b**) Cu LMM spectra.

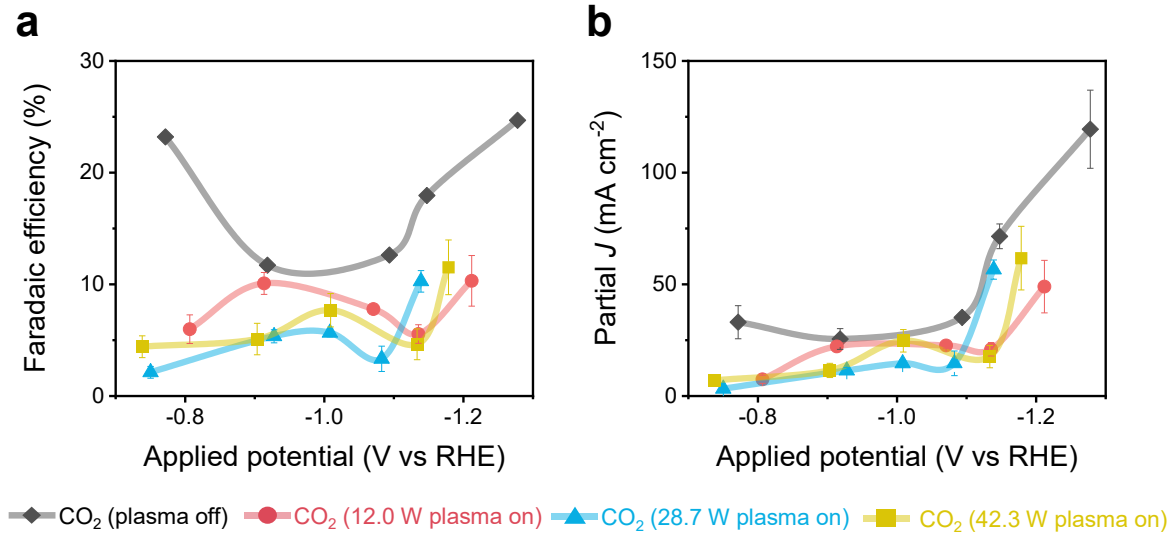
218



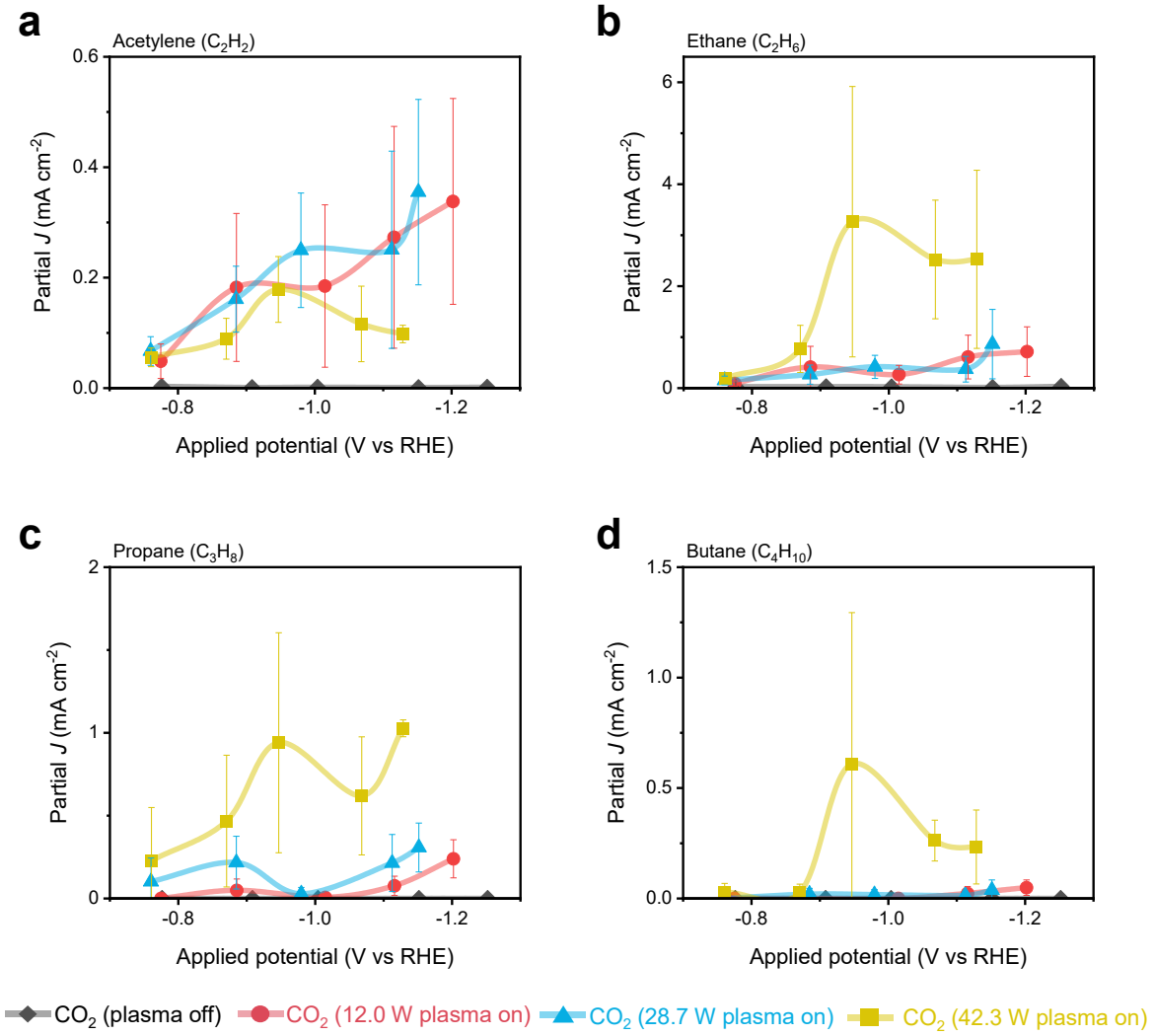
Supplementary Fig. 5 | a-b, Microstructure of as-prepared Cu GDE. (**a**) Low and (**b**) high magnification images. Metallic Cu film with 400 nm thickness was deposited on commercial polytetrafluoroethylene membrane at a rate of 0.2 nm sec^{-1}.



Supplementary Fig. 6 | a-d, Product distribution of electrochemical conversion of ground state (plasma off) and plasma-activated CO_2 at different plasma powers. (**a**) Plasma off, (**b**) 12.0 W plasma, (**c**) 28.7 W plasma, and (**d**) 42.3 W plasma. **e**, Comparison of current density (*J*) versus applied potential. A mixed gas feed of 40 ml min^{-1} CO_2 and 10 ml min^{-1} He was supplied. Each data point represents the mean and standard deviation of three independent measurements.

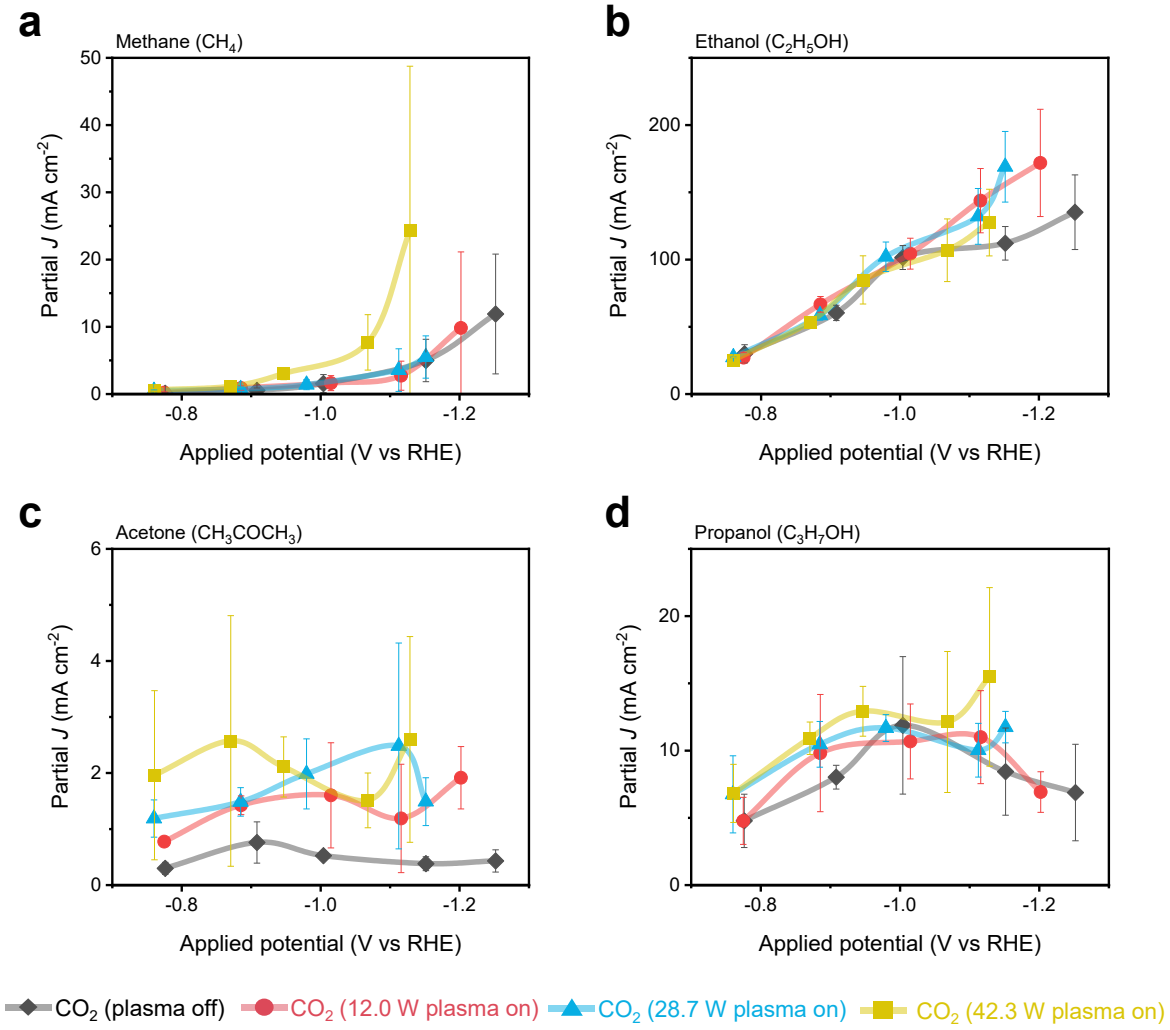


Supplementary Fig. 7 | a-b, Evaluation of hydrogen evolution reaction (HER) during plasma off and plasma-activated CO_2 electrochemical reduction at different plasma powers. (**a**) Faradaic efficiency (FE) and (**b**) partial *J* versus applied potential. Each data point represents the mean and standard deviation of three independent measurements.

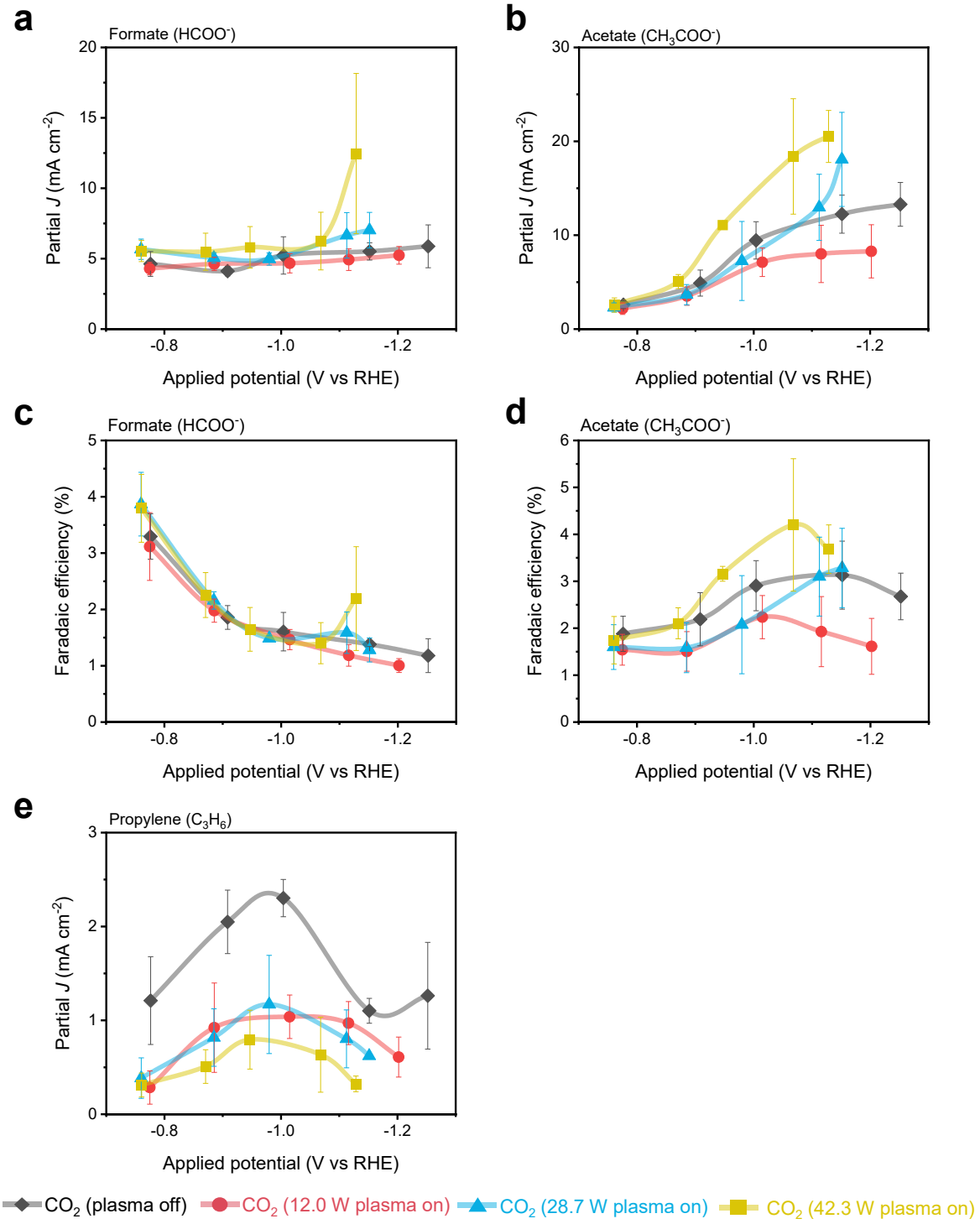


235

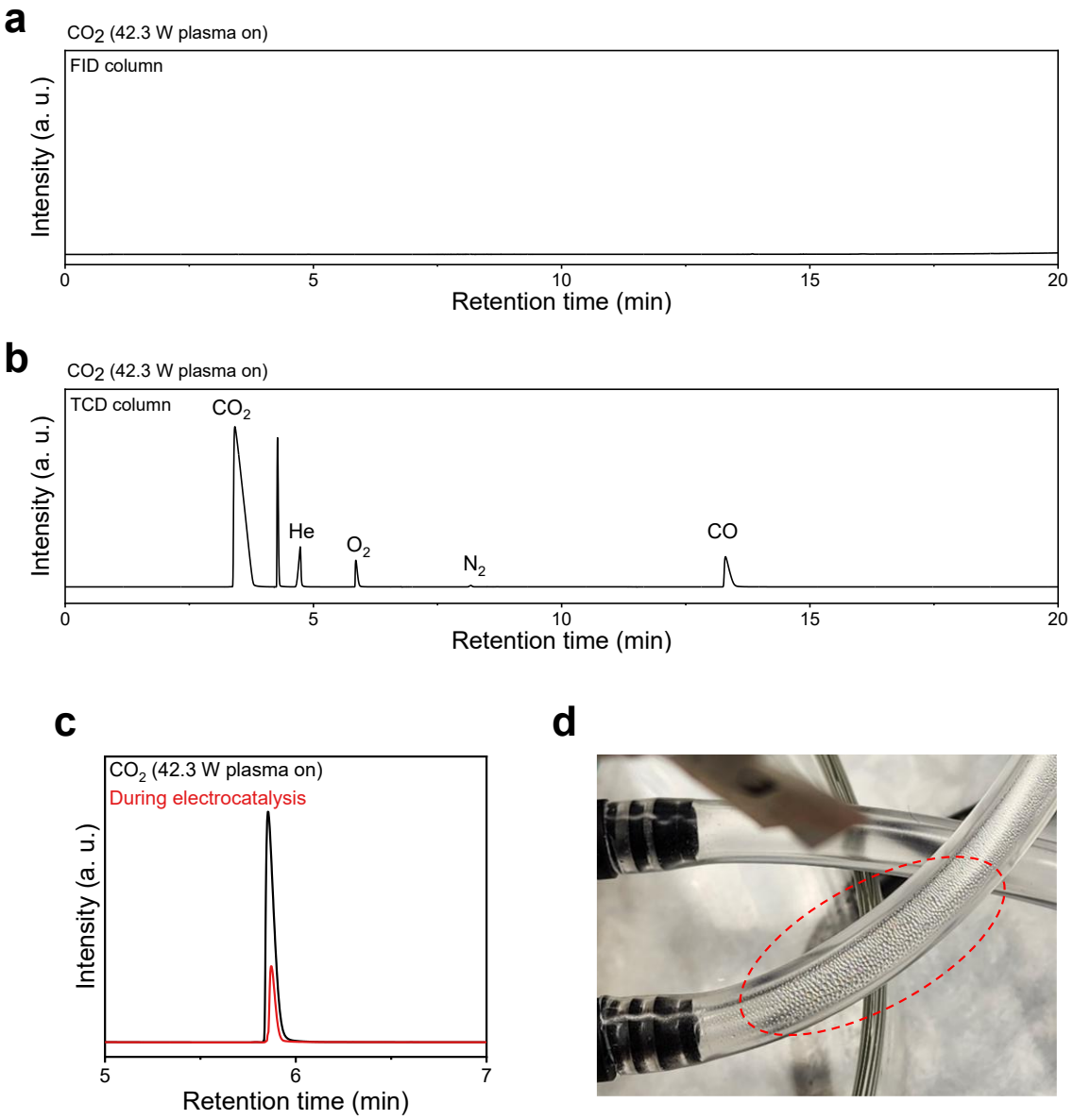
236 **Supplementary Fig. 8** | **a-d,** Partial *J* versus applied potential at different plasma powers and with
237 plasma off for products that were exclusively detected with plasma coupling compared to
238 electrocatalysis-only. Partial *J* of (**a**) C_2H_2, (**b**) C_2H_6, (**c**) C_3H_8, and (**d**) C_4H_{10}. Each data point represents
239 the mean and standard deviation of three independent measurements.



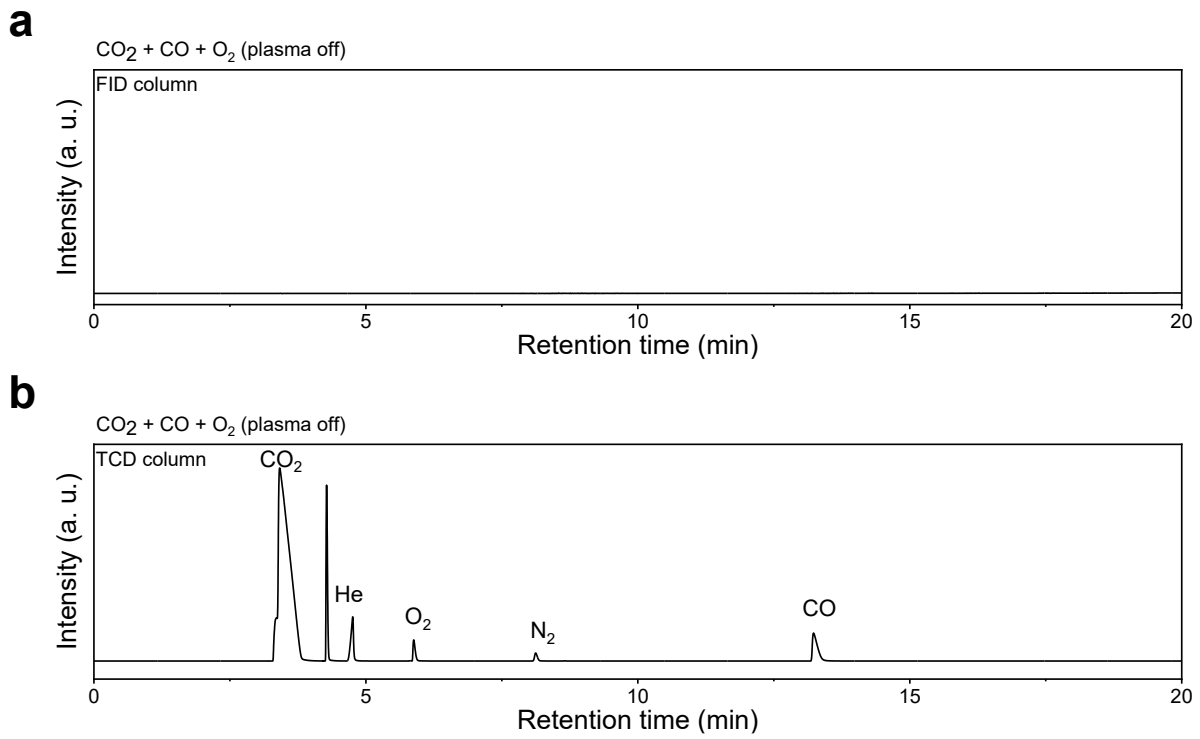
Supplementary Fig. 9 | a-d, Partial *J* versus applied potential for products that showed an increase in generation rate with plasma coupling at different powers compared to electrocatalysis-only. Partial *J* of (**a**) CH_4, (**b**) C_2H_5OH, (**c**) CH_3COCH_3, and (**d**) C_3H_7OH. Each data point represents the mean and standard deviation of three independent measurements.



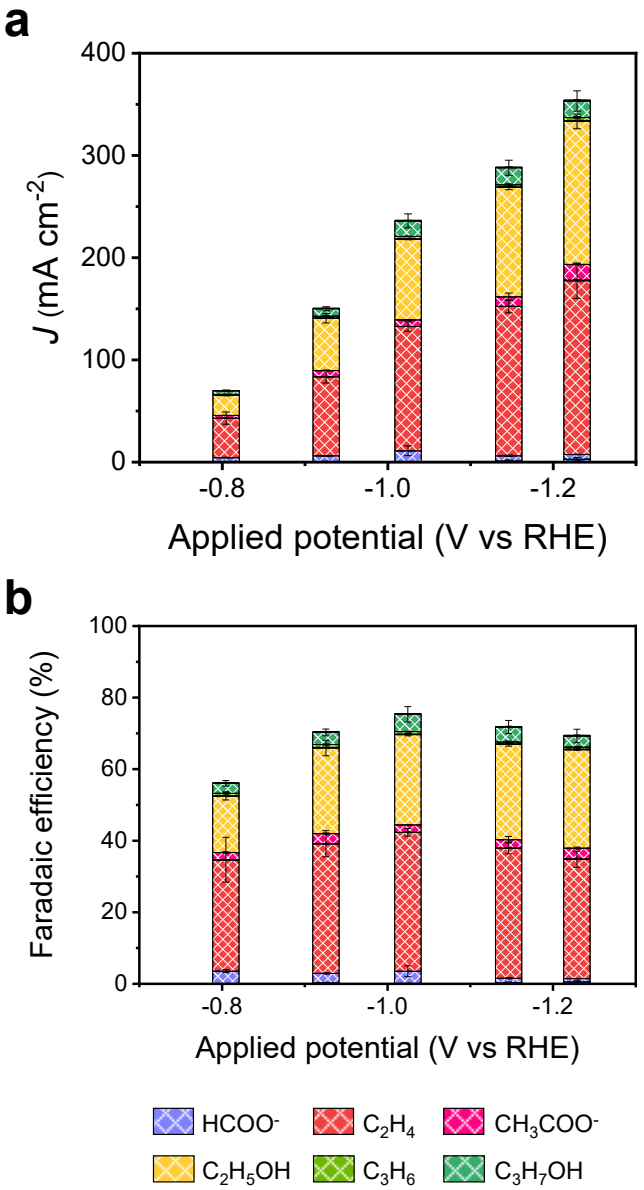
Supplementary Fig. 10 | **a-d,** Partial *J* and FE versus applied potential for (**a, c**) carboxylic acids, $HCOO^-$, and (**b, d**) CH_3COO^-, which showed similar FE with plasma coupling compared to electrocatalysis-only. (**a, b**) Partial *J* and (**c, d**) FE for ground-state CO_2 and plasma-activated CO_2 electrochemical reduction at different powers. **e**, Partial *J* of C_3H_6 for plasma off and plasma-activated CO_2 reduction at different powers. Each data point represents the mean and standard deviation of three independent measurements.



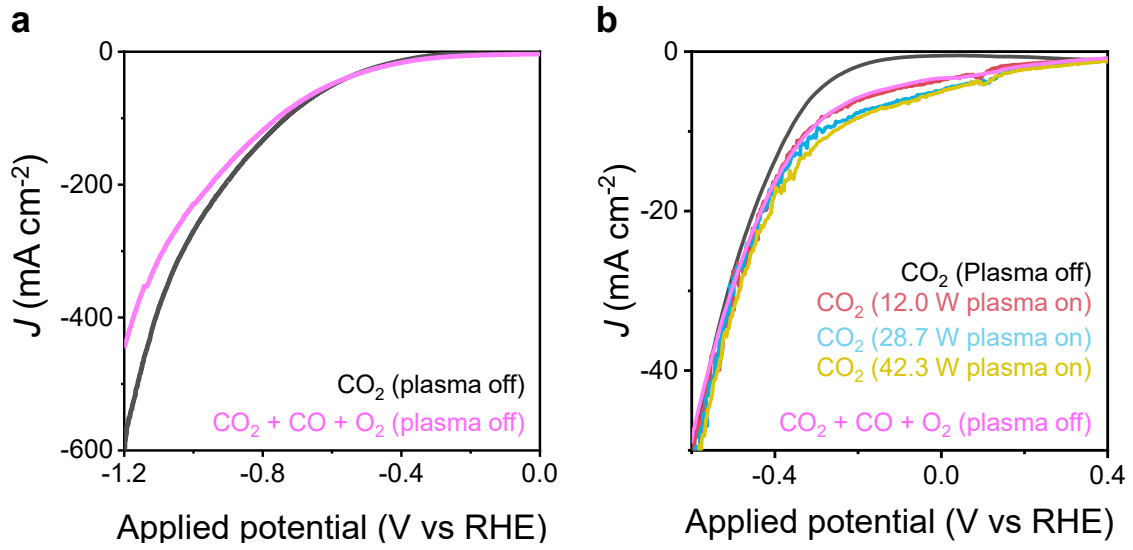
Supplementary Fig. 11 | **a-b,** Gas chromatogram of 42.3 W plasma-activated CO_2. Gas chromatogram of (**a**) flame ionization detector (FID) and (**b**) thermal conductivity detector (TCD) columns. **c,** O_2 peak before and during coupling with electrocatalytic reaction. **d,** Photograph of condensed H_2O at gas outlet generated from oxygen reduction reaction on Cu GDE. A mixed gas feed consisting of 40 ml min^{-1} CO_2 and 10 ml min^{-1} He was used.



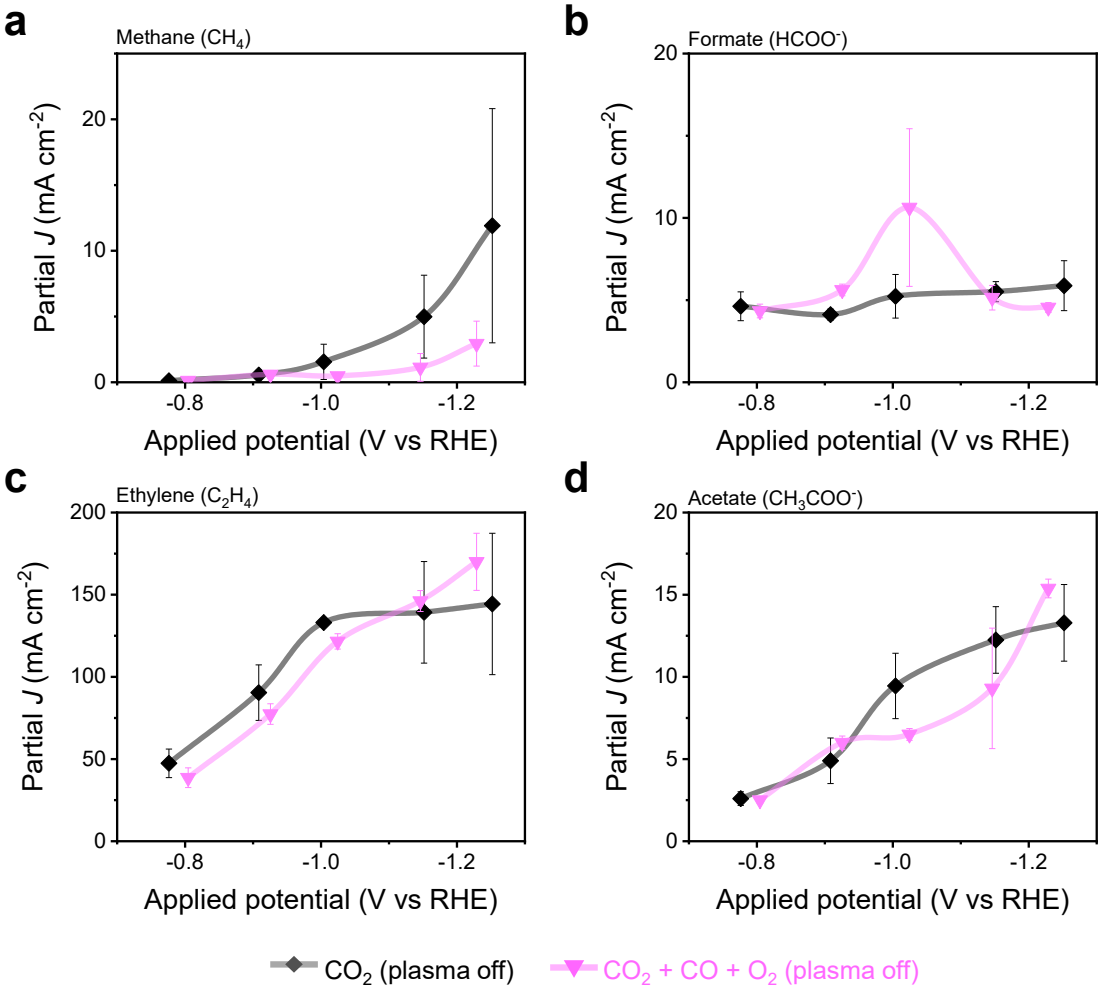
Supplementary Fig. 12 | **a-b,** Gas chromatogram of CO_2+CO+O_2 gas mixture (plasma off) for control experiment, including a gas feed consisting of 38 ml min^{-1} CO_2 + 10 ml min^{-1} He + 1.7 ml min^{-1} CO + 0.7 ml min^{-1} O_2. (**a**) FID and (**b**) TCD column.



Supplementary Fig. 13 | **a-b,** Electrocatalytic conversion of the CO_2 + CO + O_2 mixed gas (plasma off) control experiment. (**a**) Partial *J* and (**b**) FE distribution versus applied potential. The flow rates of the gases in the mixed feed gas were 38 ml min^{-1} CO_2 + 10 ml min^{-1} He + 1.7 ml min^{-1} CO + 0.7 ml min^{-1} O_2. Each data point represents the mean and standard deviation of three independent measurements.

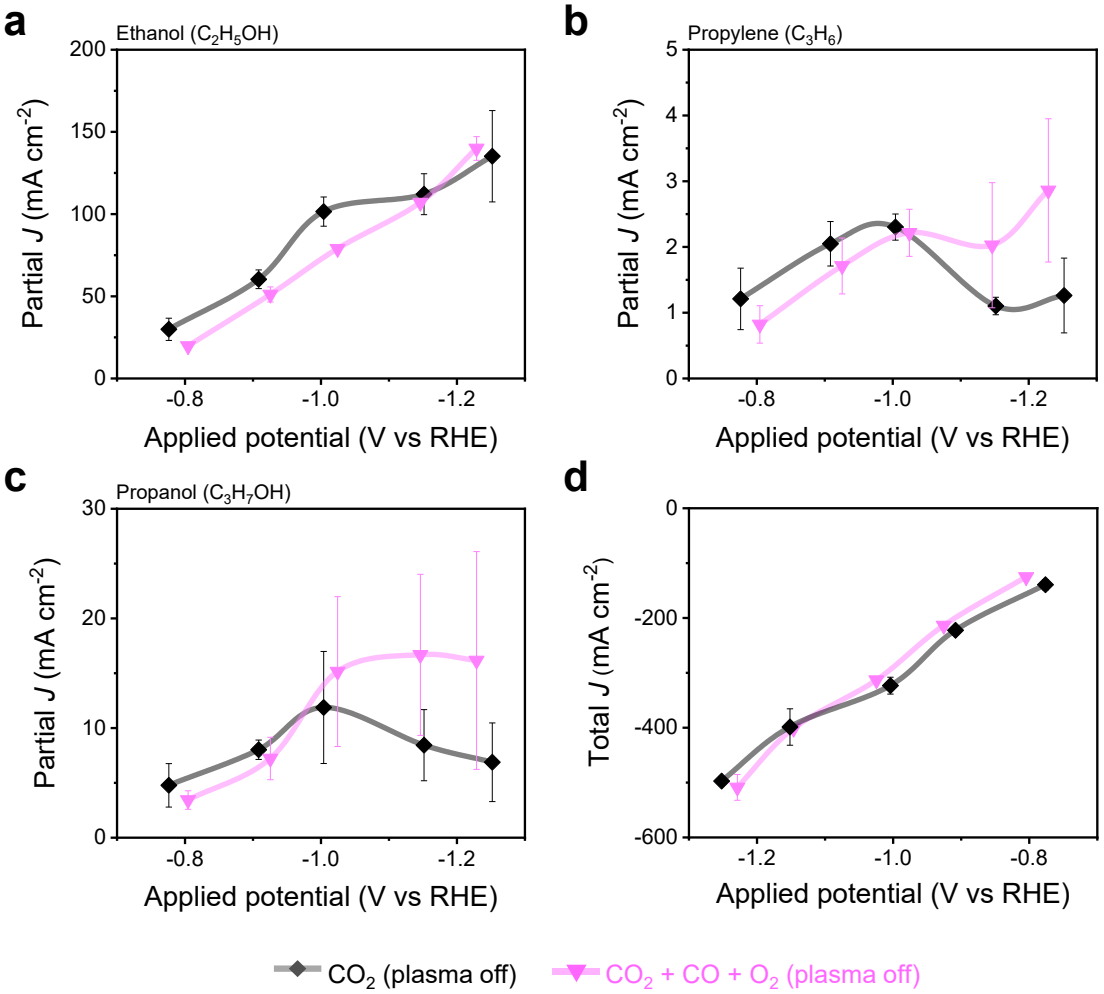


Supplementary Fig. 14 | Total current density for CO_2 electrocatalysis, plasma-electrocatalysis, and mixed-gas control experiment. a, Linear sweep voltammetry (LSV) of CO_2 electrocatalysis and CO_2 + CO + O_2 mixed gas control with a gas composition comparable to that of the plasma-activated CO_2 effluent, without plasma activation. **b,** LSV of the mixed-gas control compared with CO_2 plasma-electrocatalysis using different plasma powers ranging from 12.0 to 42.3 W. Plasma-off operation (electrocatalysis-only) was used as a control. All measurements were performed in 1 M KOH electrolyte at a scan rate of 1 mV s^{-1}. Each point is the averaged value of three independent measurements.



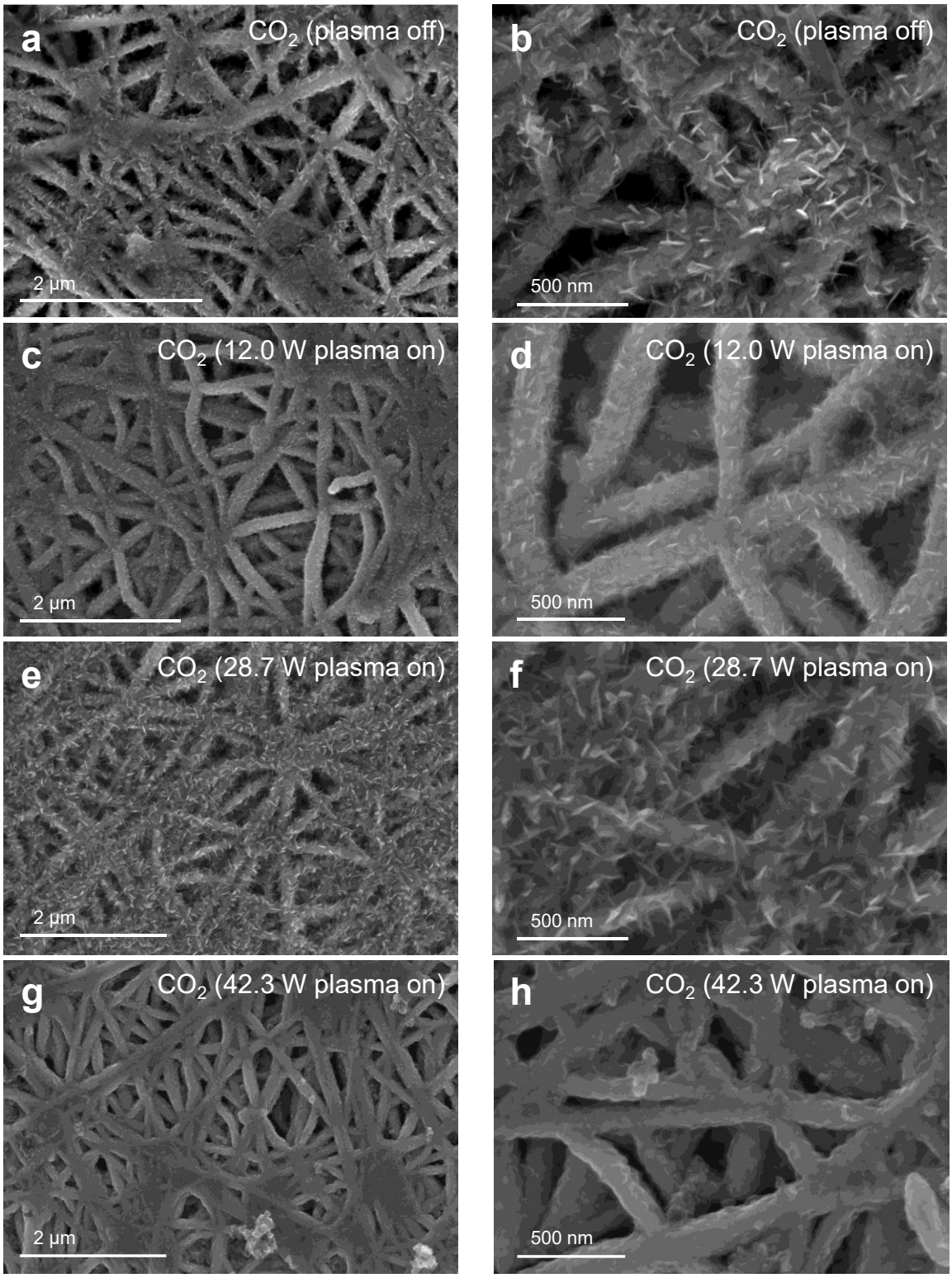
278

279 **Supplementary Fig. 15 | a-d,** Partial *J* comparison between electrocatalytic conversion of CO_2 (plasma
280 off) and CO_2 + CO + O_2 mixed feed (plasma off; simulated plasma effluent) versus applied potential.
281 Partial *J* of (**a**) CH_4, (**b**) $HCOO^-$, (**c**) C_2H_4, and (**d**) CH_3COO^-. For the CO_2 conversion, a mixture of 40
282 ml min^{-1} CO_2 + 10 ml min^{-1} He was fed. For the conversion of the simulated plasma effluent, a mixture
283 of 38 ml min^{-1} CO_2 + 10 ml min^{-1} He + 1.7 ml min^{-1} CO + 0.7 ml min^{-1} O_2 was fed. Each data point
284 represents the mean and standard deviation of three independent measurements.

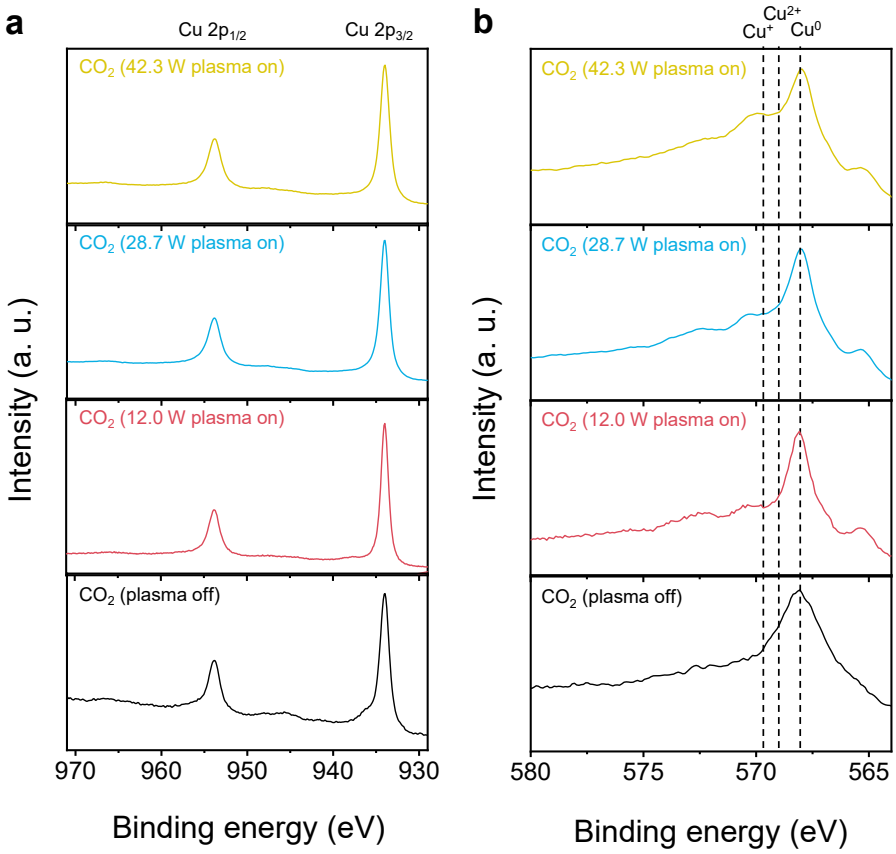


285

286 **Supplementary Fig. 16 | a-c,** Partial *J* comparison between electrocatalytic conversion of CO_2 (plasma
287 off) and CO_2 + CO + O_2 mixture gases (plasma off) versus applied potential. Partial *J* of (**a**) C_2H_5OH,
288 (**b**) C_3H_6, and (**c**) C_3H_7OH. **d**, Total *J* was compared between CO_2 (plasma off) and CO_2 + CO + O_2
289 mixture gases (plasma off) versus applied potential. For the CO_2 conversion, mixed gas of 40 ml min^{-1}
290 CO_2 + 10 ml min^{-1} He was fed. For the mixture gases conversion, mixed gas of 38 ml min^{-1} CO_2 + 10
291 ml min^{-1} He + 1.7 ml min^{-1} CO + 0.7 ml min^{-1} O_2 was fed. Each data point represents the mean and
292 standard deviation of three independent measurements.



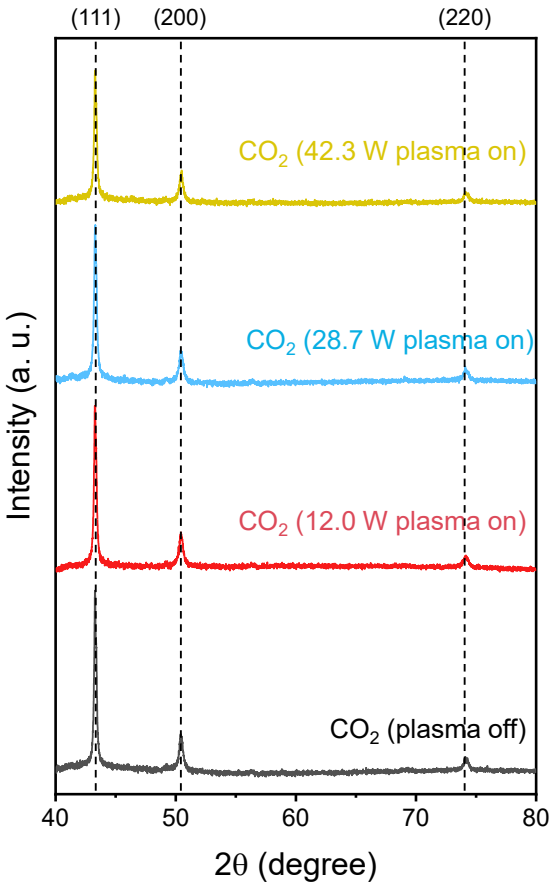
Supplementary Fig. 17 | **a-h,** Microstructure analysis of Cu GDE after electrocatalytic conversion of (**a, b**) plasma off CO_2, (**c, d**) 12.0 W plasma-activated CO_2, (**e, f**) 28.7 W plasma-activated CO_2, and (**g, h**) 42.3 W plasma-activated CO_2. The reactions were conducted for 1 hour at -1.7 V (vs RHE, before IR compensation) in 1 M KOH electrolyte. (**a, c, e, g**) Low and (**b, d, f, h**) high magnification. A mixed gas feed consisting of 40 ml min^{-1} CO_2 + 10 ml min^{-1} He was used.



299

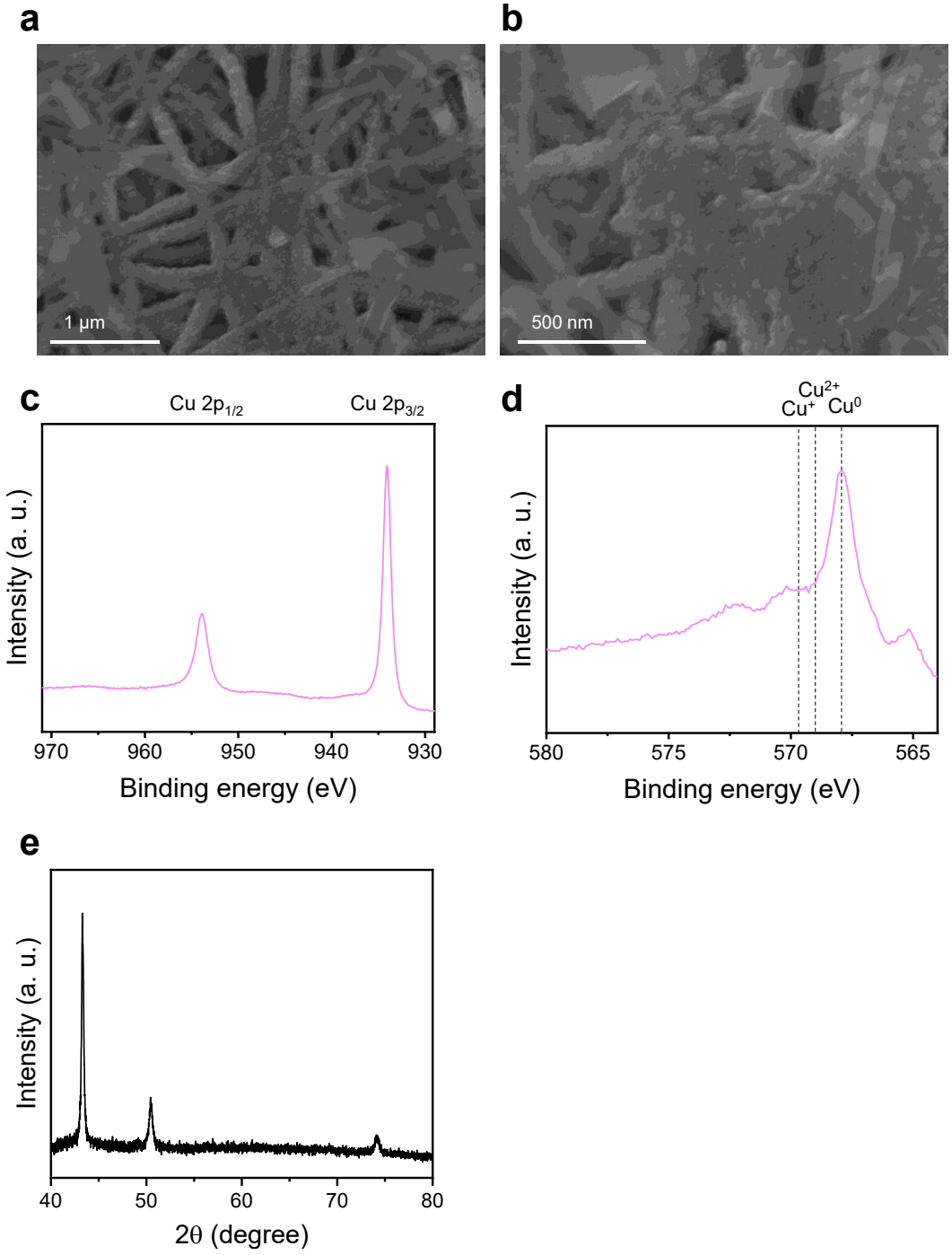
300 **Supplementary Fig. 18 | XPS analysis of Cu oxidation states after electrocatalytic conversion of**
301 **ground state CO_2 (plasma off) and plasma-activated CO_2 at different powers. a**, Cu 2p and **b**, Cu
302 LMM spectra. Peaks at 567.8 eV in Cu LMM spectra correspond to Cu^0 state. A shoulder peak at 572.5
303 eV indicates the presence of native/subsurface oxide. The reactions were conducted for 1 hour at -1.7
304 V (vs RHE, before IR compensation) in 1 M KOH electrolyte. A mixed gas feed consisting of 40 ml
305 min^{-1} CO_2 + 10 ml min^{-1} He was used. The surface layer was etched before XPS analysis using a C_{60}
306 gun. Peaks were calibrated based on C 1s spectrum as an internal standard.

307



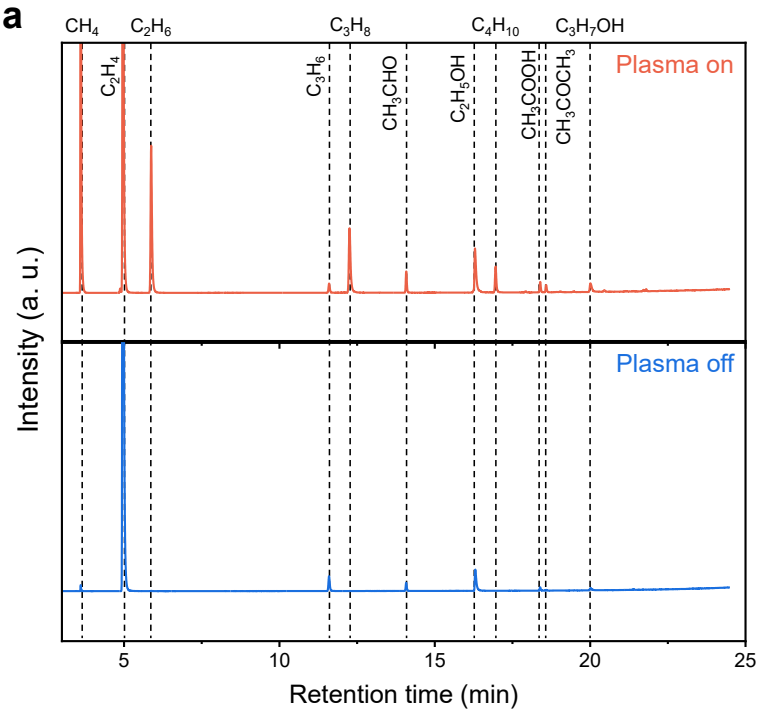
308

309 **Supplementary Fig. 19** | XRD pattern of Cu GDE after electrocatalytic conversion of ground state CO_2
310 (plasma off) and plasma-activated CO_2 at different powers. The experiments were conducted for 1 hour
311 at -1.7 V (vs RHE, before IR compensation) in 1 M KOH electrolyte.



312

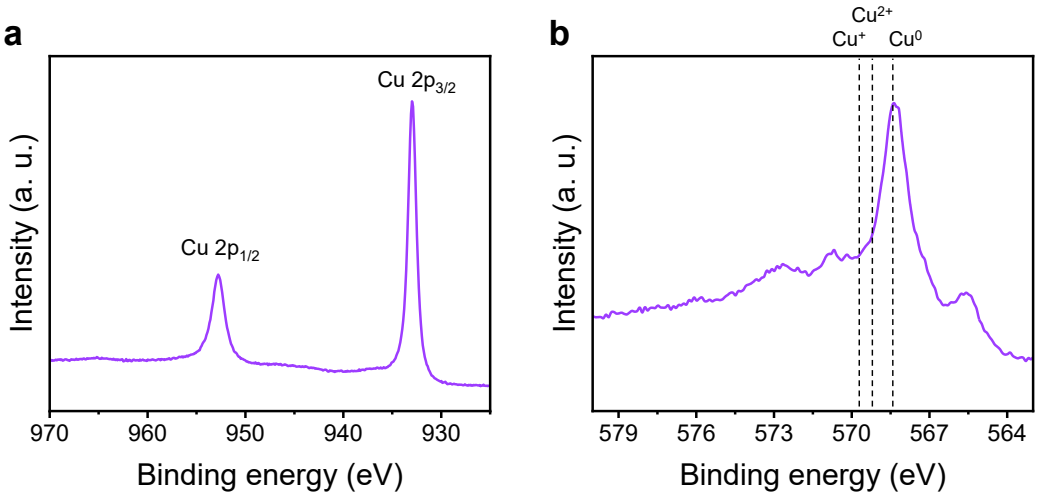
313 **Supplementary Fig. 20 | a-e,** Analysis on microstructure, oxidation state, and phase of Cu GDE after
314 electrocatalytic CO_2 + CO + O_2 (plasma off) conversion. (**a**) Low and (**b**) high magnification SEM
315 images. (**c**) XPS Cu 2p spectrum, (**d**) XPS Cu LMM spectrum, and (**e**) XRD pattern. The flow rates of
316 the mixed feed gases were 38 ml min^{-1} CO_2, 10 ml min^{-1} He, 1.7 ml min^{-1} CO, and 0.7 ml min^{-1} O_2. The
317 experiment was conducted for 1 hour at -1.7 V (vs RHE, before IR compensation) in 1 M KOH
318 electrolyte.



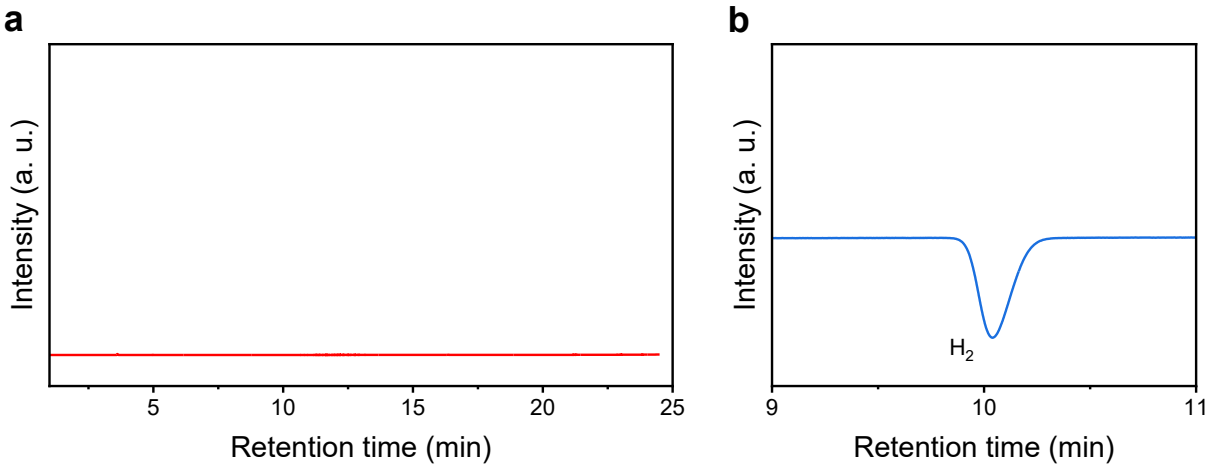
b

Product	Plasma on (μmol L^{-1})	Plasma off (μmol L^{-1})
CH_4	2766.0	15.1
C_2H_4	1628.9	3012.9
C_2H_6	436.2	0.5
C_2H_5OH	314.8	139.0
C_3H_8	156.0	0
C_3H_7OH	60.5	15.6
C_4H_{10}	37.6	0

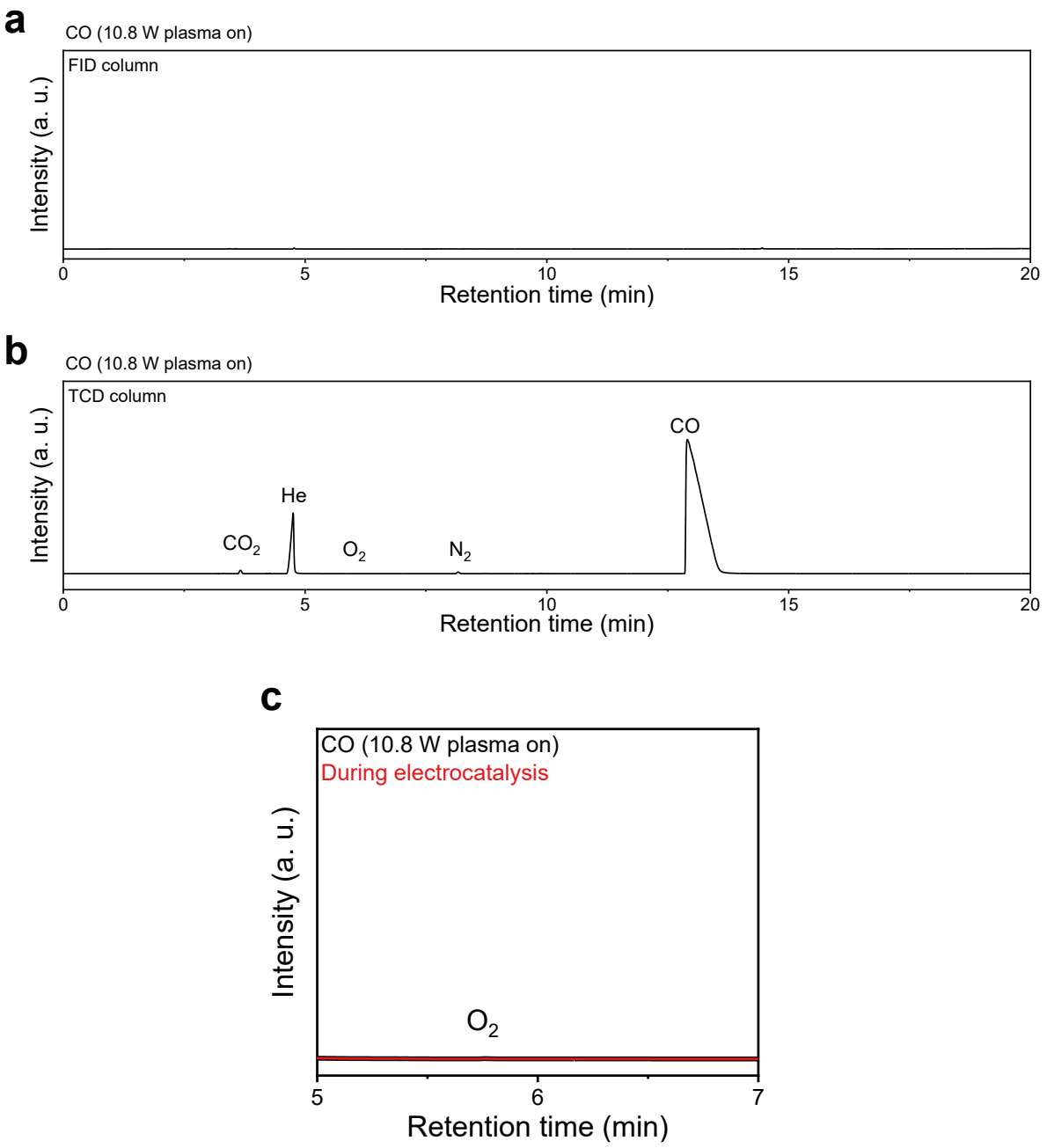
Supplementary Fig. 21 | Gas chromatograms showing product evolution during plasma on/off modulation in CO_2 + CO plasma-electrocatalysis. a-b, Gas phase products were analyzed by GC during sequential plasma-on/plasma-off electrocatalysis using the same catalyst. A mixed gas of 30 ml min^{-1} CO_2 + 10 ml min^{-1} CO + 10 ml min^{-1} He was supplied. A constant potential of -2 V (vs RHE, before IR compensation) was applied for 1 h, with plasma activation turned on during the first 30 min, followed by plasma-off (electrocatalysis only) operation for the remaining 30 min. (**a**) Gas chromatograms show the corresponding evolution of gas products upon plasma on/off with same y-axis scale. 1 M KOH solution was used as an electrolyte. (**b**) Product concentrations of major chemicals detected in the effluent gas stream from the reactor.



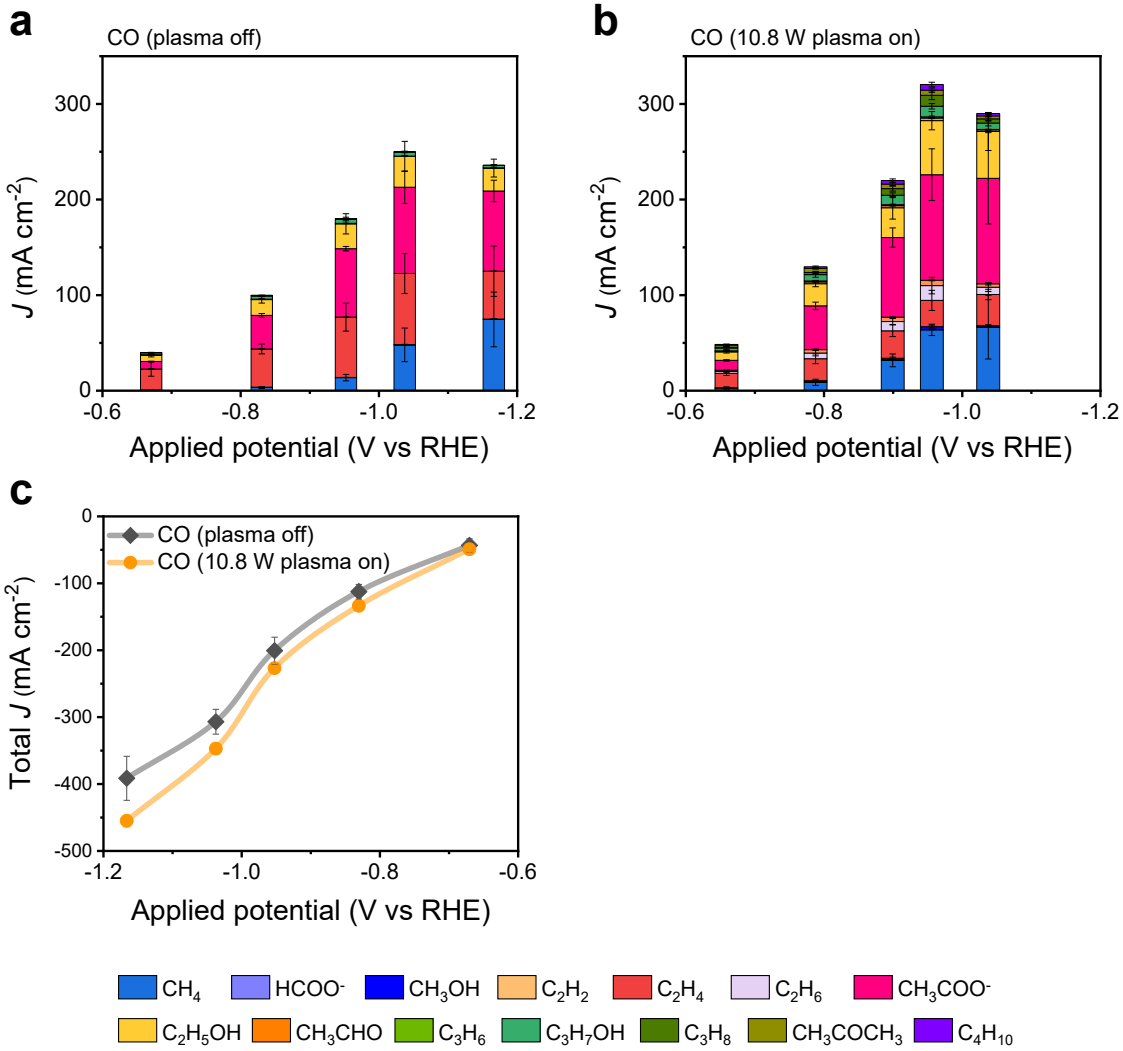
Supplementary Fig. 22 | Chemical state analysis of Cu catalysts after sequential plasma on/off operation. The chemical state of Cu was analyzed following a sequential plasma on/off experiment. A constant potential of -2 V (vs. RHE, before IR compensation) was applied for 1 h, with plasma-electrocatalysis during the first 30 min followed by electrocatalysis-only operation for the subsequent 30 min. **a,** Cu 2p XPS spectra. **b,** Cu LMM Auger spectra. Prior to XPS analysis, the samples were etched by a C_{60} gun to expose the catalyst surface.



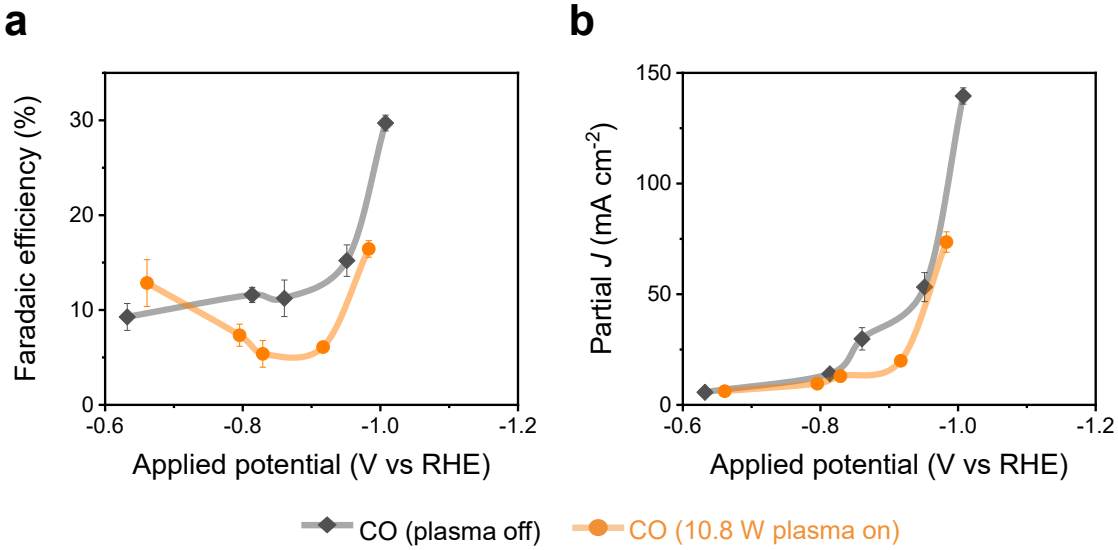
Supplementary Fig. 23 | Gas product analysis of He plasma-electrocatalysis. a-b, Gas phase products generated in He plasma-electrocatalysis were analyzed under He feed of 50 mL min^{-1} with an applied potential of -2 V (vs. RHE, before IR compensation). The product gas stream was characterized by GC using (**a**) FID column and (**b**) TCD column. He was employed as the internal carrier gas for the TCD column, resulting in an inverted H_2 signal.



Supplementary Fig. 24 | **a-c,** Gas chromatogram of 10.8 W plasma-activated CO. (**a**) FID and (**b**) TCD columns. (**c**) Magnified TCD column around O_2 peak. O_2 peaks were compared before and during coupling with electrocatalytic conversion. O_2 was not detected. A mixed gas feed consisting of 30 ml min^{-1} CO and 20 ml min^{-1} He was used.

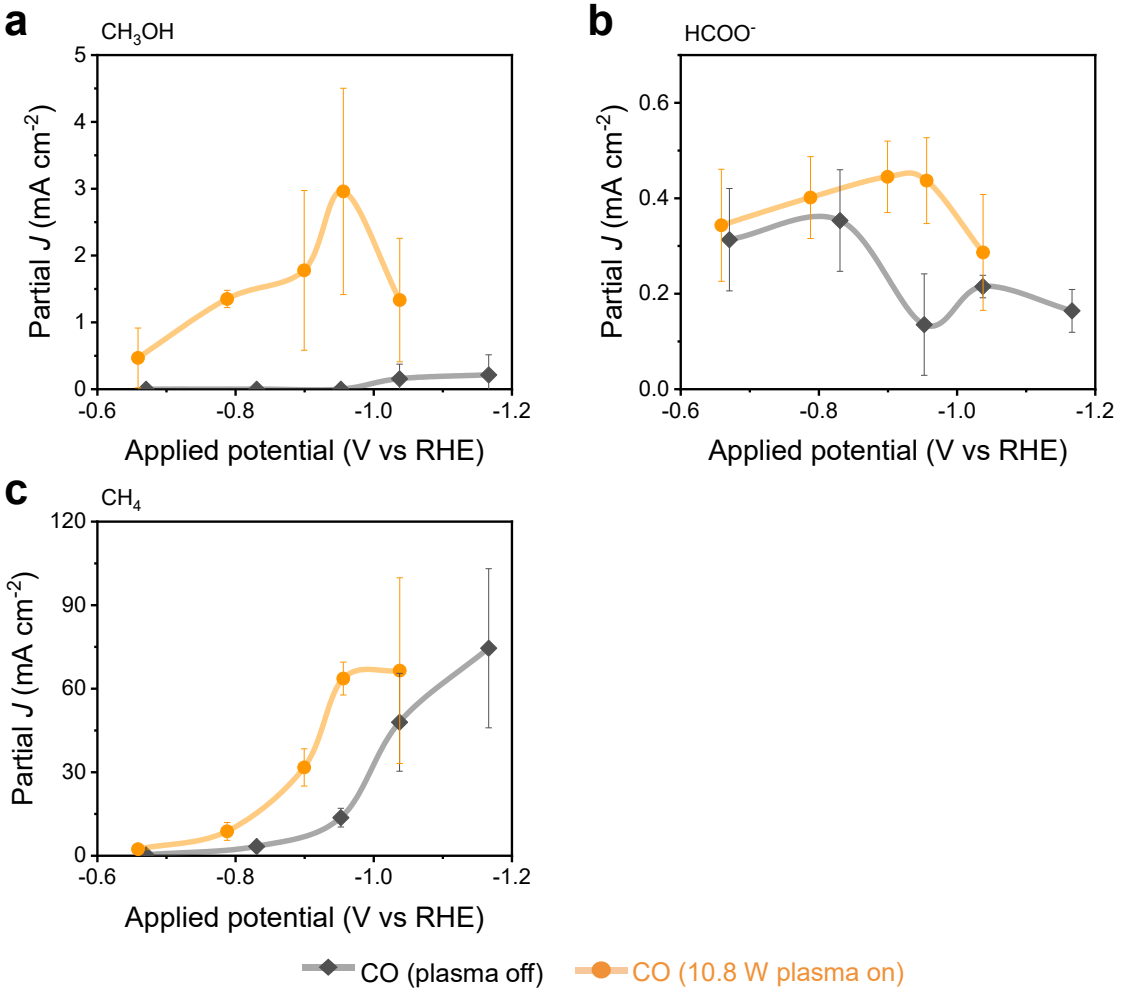


Supplementary Fig. 25 | **a-c,** Electrocatalytic conversion of CO with and without plasma. Product distribution of electrochemical conversion of (**a**) ground state CO (plasma off) and (**b**) 10.8 W plasma-activated CO versus applied potential. (**c**) Total *J* comparison. A mixed gas feed consisting of 30 ml min^{-1} CO and 20 ml min^{-1} He was supplied. Each data point represents the mean and standard deviation of three independent measurements.



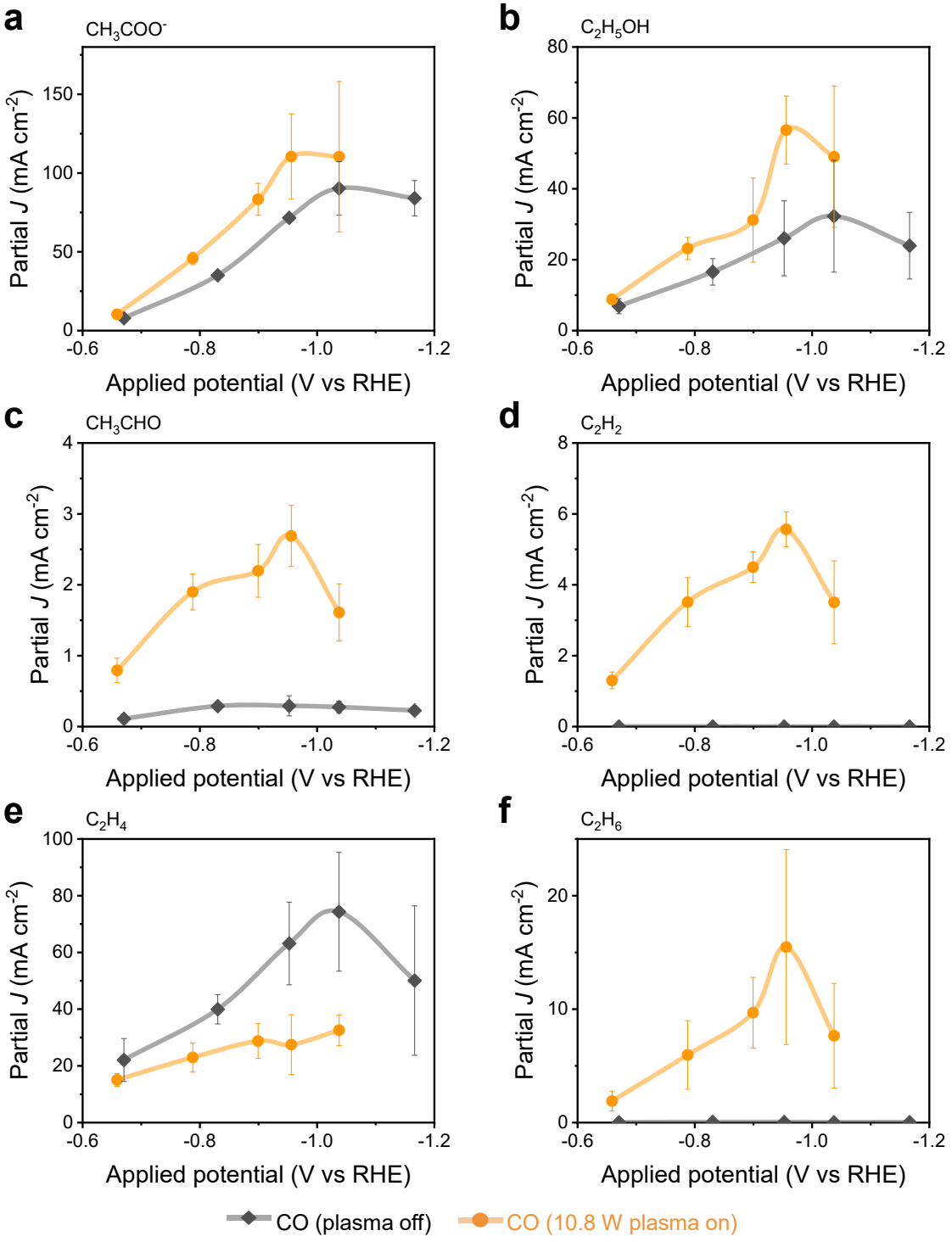
356

357 **Supplementary Fig. 26** | **a-b,** Evaluation of HER during ground state (plasma off) CO and 10.8 W
358 plasma-activated CO electroreduction. Comparison of (**a**) FE and (**b**) partial *J* versus applied potential.
359 A mixed gas feed consisting of 30 ml min^{-1} CO and 20 ml min^{-1} He was supplied. Each data point
360 represents the mean and standard deviation of three independent measurements.

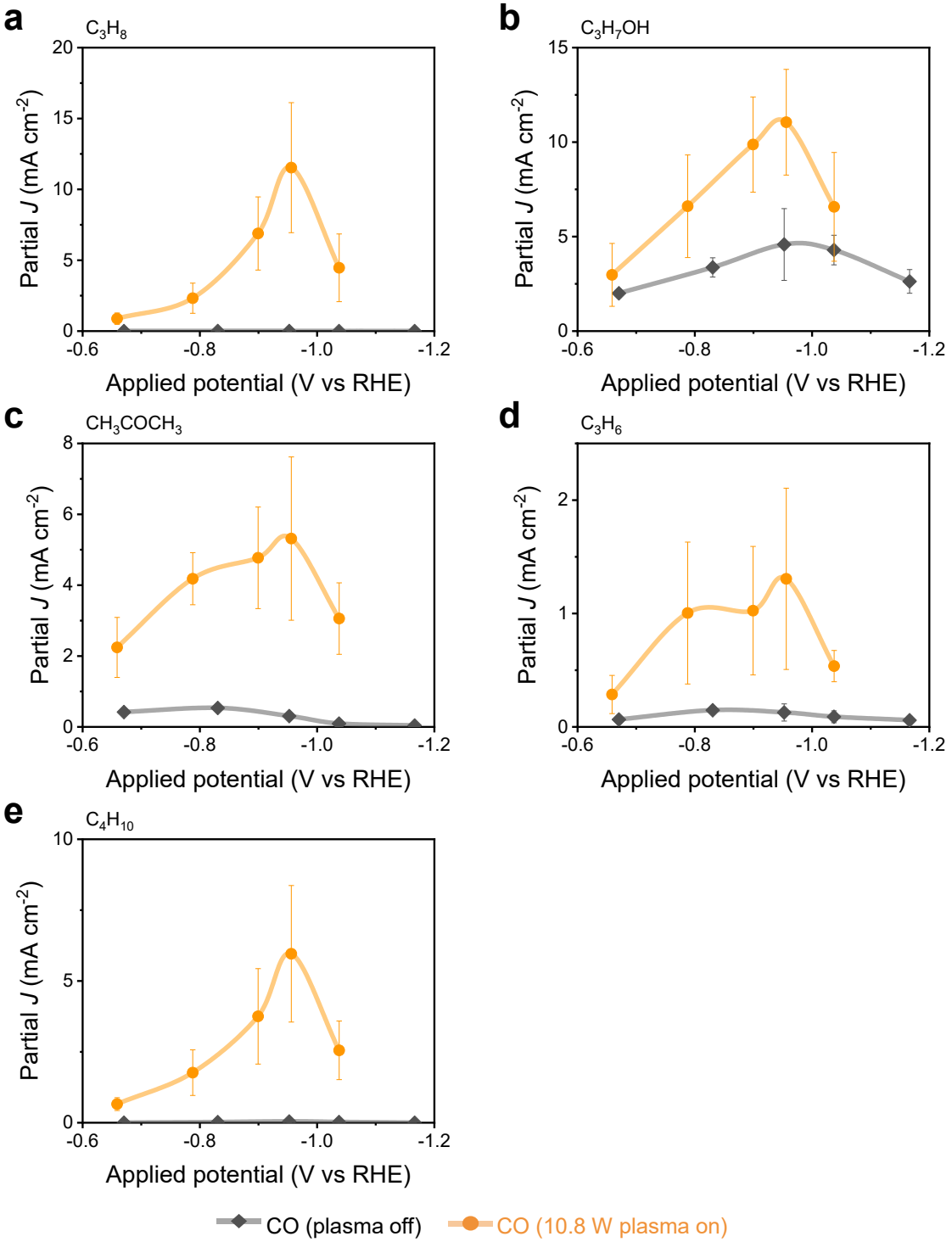


361

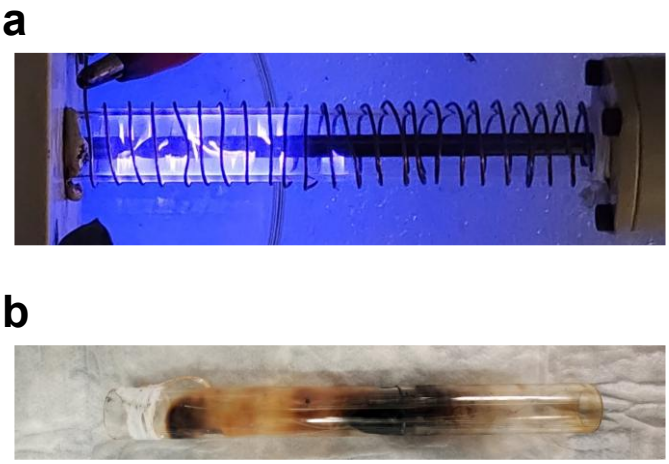
362 **Supplementary Fig. 27** | **a-c,** Comparison of partial *J* for C_1 products between electrocatalytic
363 conversion of ground state CO (plasma off) and 10.8 W plasma-activated CO. Partial *J* of (**a**) CH_3OH,
364 (**b**) $HCOO^-$, and (**c**) CH_4. A mixed gas feed consisting of 30 ml min^{-1} CO and 20 ml min^{-1} He was
365 supplied. Each data point represents the mean and standard deviation of three independent
366 measurements.



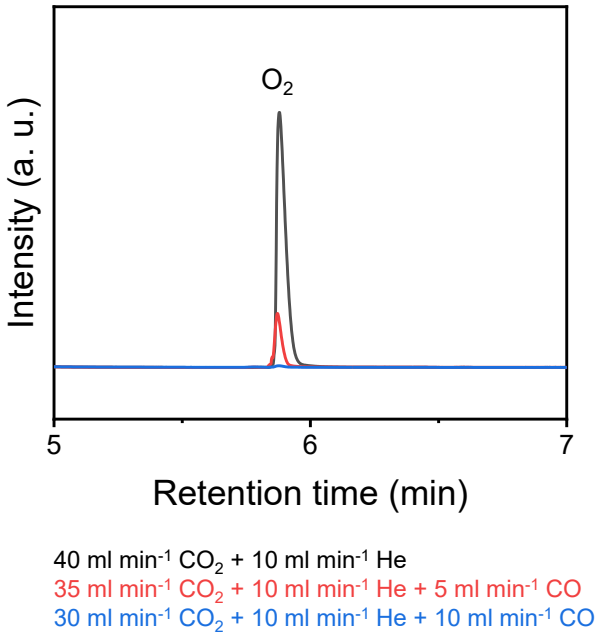
Supplementary Fig. 28 | a-f, Comparison of partial *J* for C_2 products between electrocatalytic conversion of ground state CO (plasma off) and 10.8 W plasma-activated CO. Partial *J* of (**a**) CH_3COO^-, (**b**) C_2H_5OH, (**c**) CH_3CHO, (**d**) C_2H_2, (**e**) C_2H_4, and (**f**) C_2H_6. A mixed gas feed consisting of 30 ml min^{-1} CO and 20 ml min^{-1} He was supplied. Each data point represents the mean and standard deviation of three independent measurements.



Supplementary Fig. 29 | **a-e,** Comparison of partial *J* for C_{3+} products between electrocatalytic conversion of ground state CO (plasma off) and 10.8 W plasma-activated CO. Partial *J* of (**a**) C_3H_8, (**b**) C_3H_7OH, (**c**) CH_3COCH_3, (**d**) C_3H_6, and (**e**) C_4H_{10}. A mixed gas feed consisting of 30 ml min^{-1} CO and 20 ml min^{-1} He was supplied. Each data point represents the mean and standard deviation of three independent measurement.



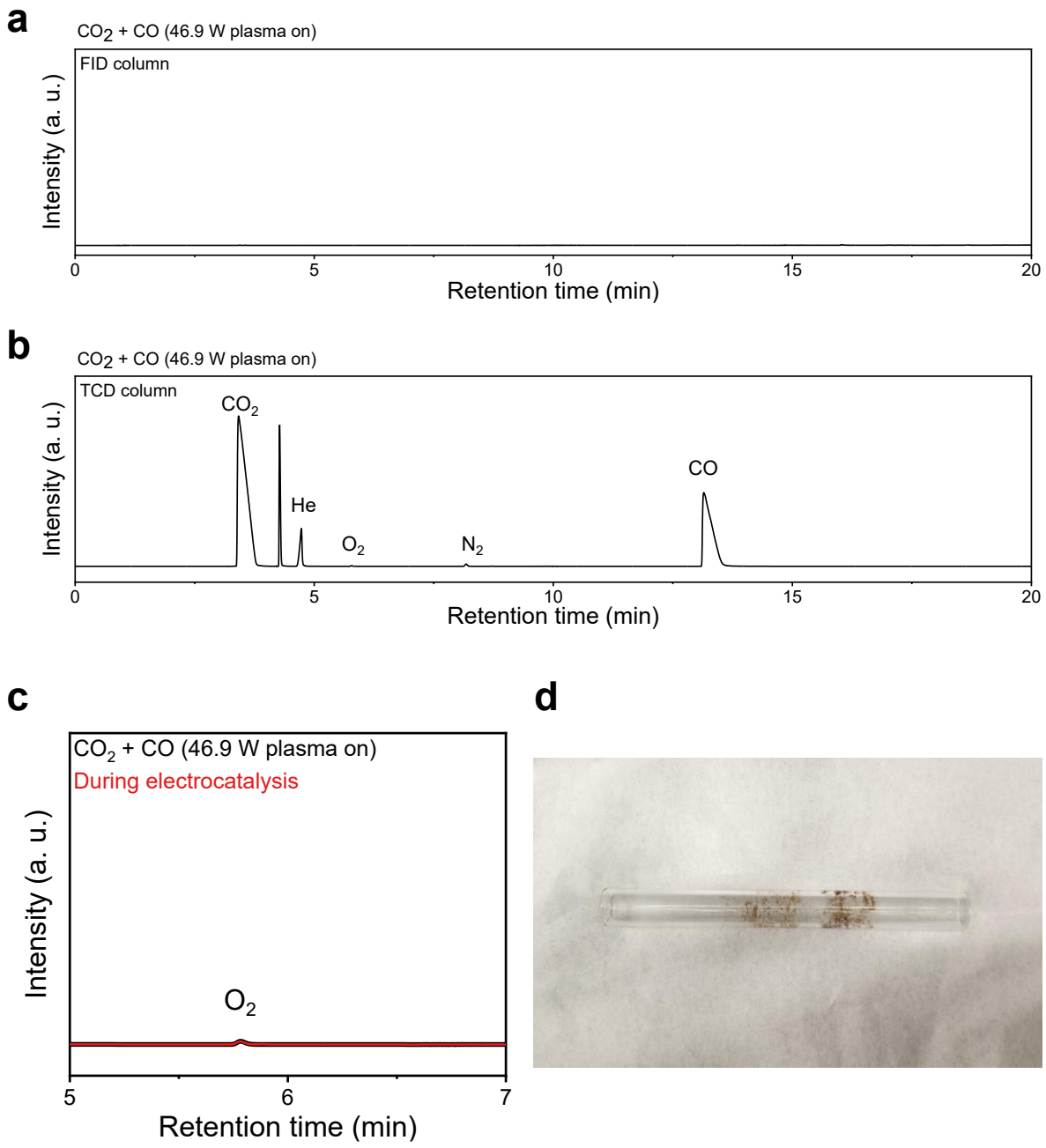
Supplementary Fig. 30 | a-b, (**a**) Photograph of filamentary CO plasma at 10.8 W power and (**b**) C deposition on the quartz tube wall after plasma operation. The flow rates of the gases in the mixed feed were 30 ml min^{-1} CO and 20 ml min^{-1} He.



385

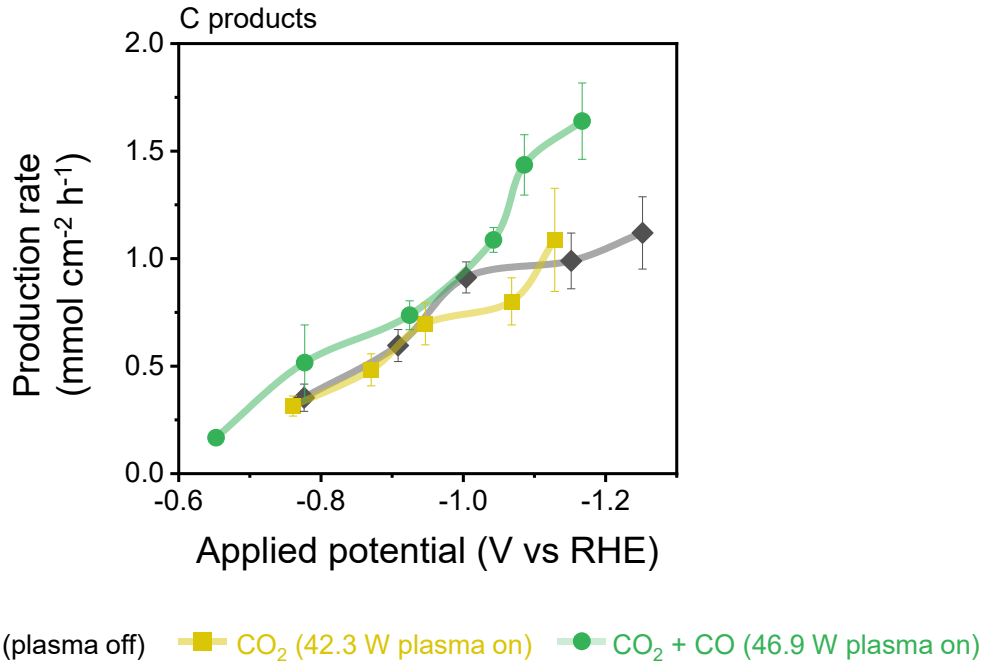
386 **Supplementary Fig. 31** | Gas chromatogram of plasma-activated CO_2+CO with different feed
387 compositions. The TCD chromatogram was magnified around the O_2 peak.

388



389

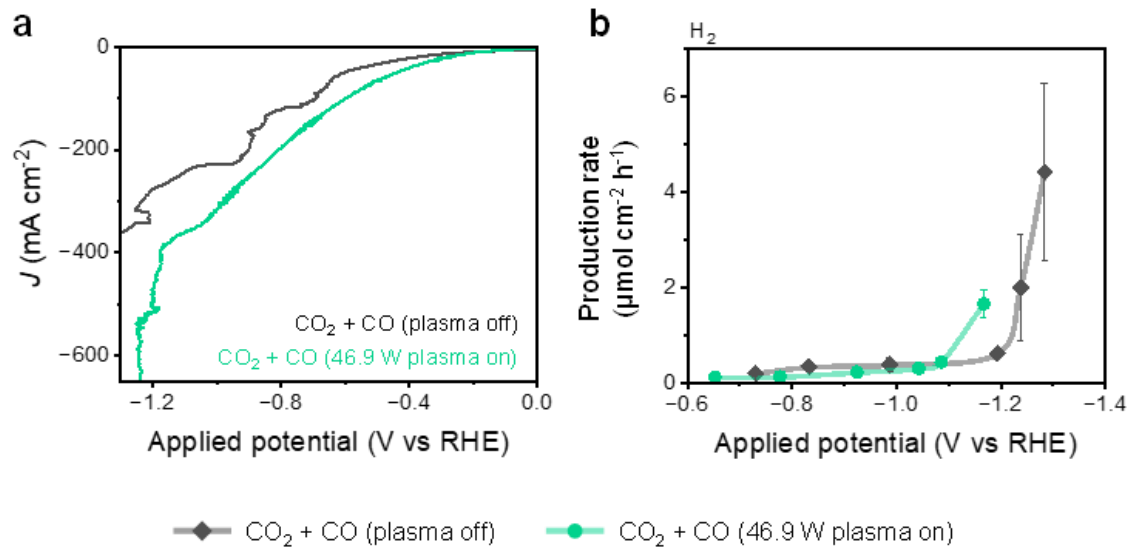
390 **Supplementary Fig. 32** | **a-c,** Gas chromatogram of 46.9 W plasma-activated CO_2+CO. (**a**) FID and
391 (**b**) TCD columns. (**c**) Magnified TCD column around the O_2 peak. The O_2 peak remained unchanged
392 before and during coupling with electrocatalytic conversion, which suggested the absence of oxygen
393 reduction. **d,** Image of the quartz tube after plasma operation. C deposition was mitigated compared to
394 CO plasma at 10.8 W. The flow rates of gases in the mixed feed were 30 ml min^{-1} CO_2 + 10 ml min^{-1}
395 He + 10 ml min^{-1} CO.



396

397 **Supplementary Fig. 33 | Comparison of total production rate for C-containing products between**
398 **ground state CO_2, 42.3 W plasma-coupled CO_2, and 46.9 W plasma-coupled CO_2 + CO conversion.**

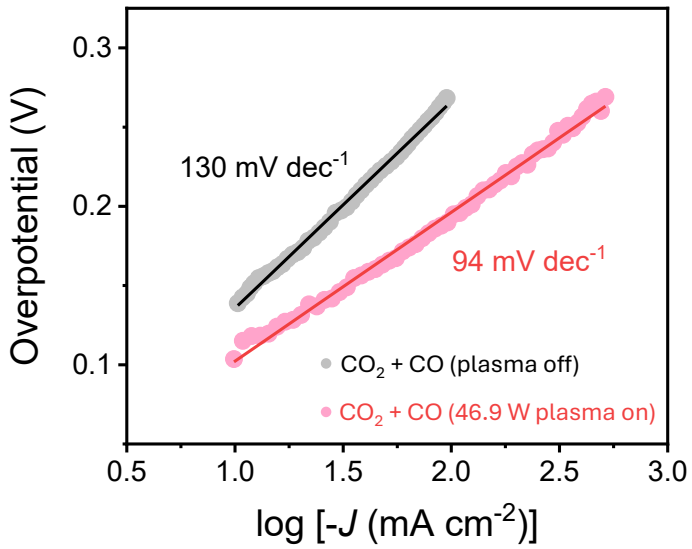
399



400

401 **Supplementary Fig. 34 | Evaluation of reaction activity and HER during plasma-electrocatalytic**
402 **CO_2 + CO conversion. a,** LSV curves collected without (plasma off) and with 46.9 W plasma activation
403 of CO_2 + CO at a scan rate of 1 mV sec^{-1} in 1 M KOH electrolyte. **b,** Comparison of production rates
404 of H_2. A mixed gas was supplied consisting of 30 ml min^{-1} CO_2, 10 ml min^{-1} CO, and 10 ml min^{-1} He.
405 Each data point represents the mean of three independent measurements.

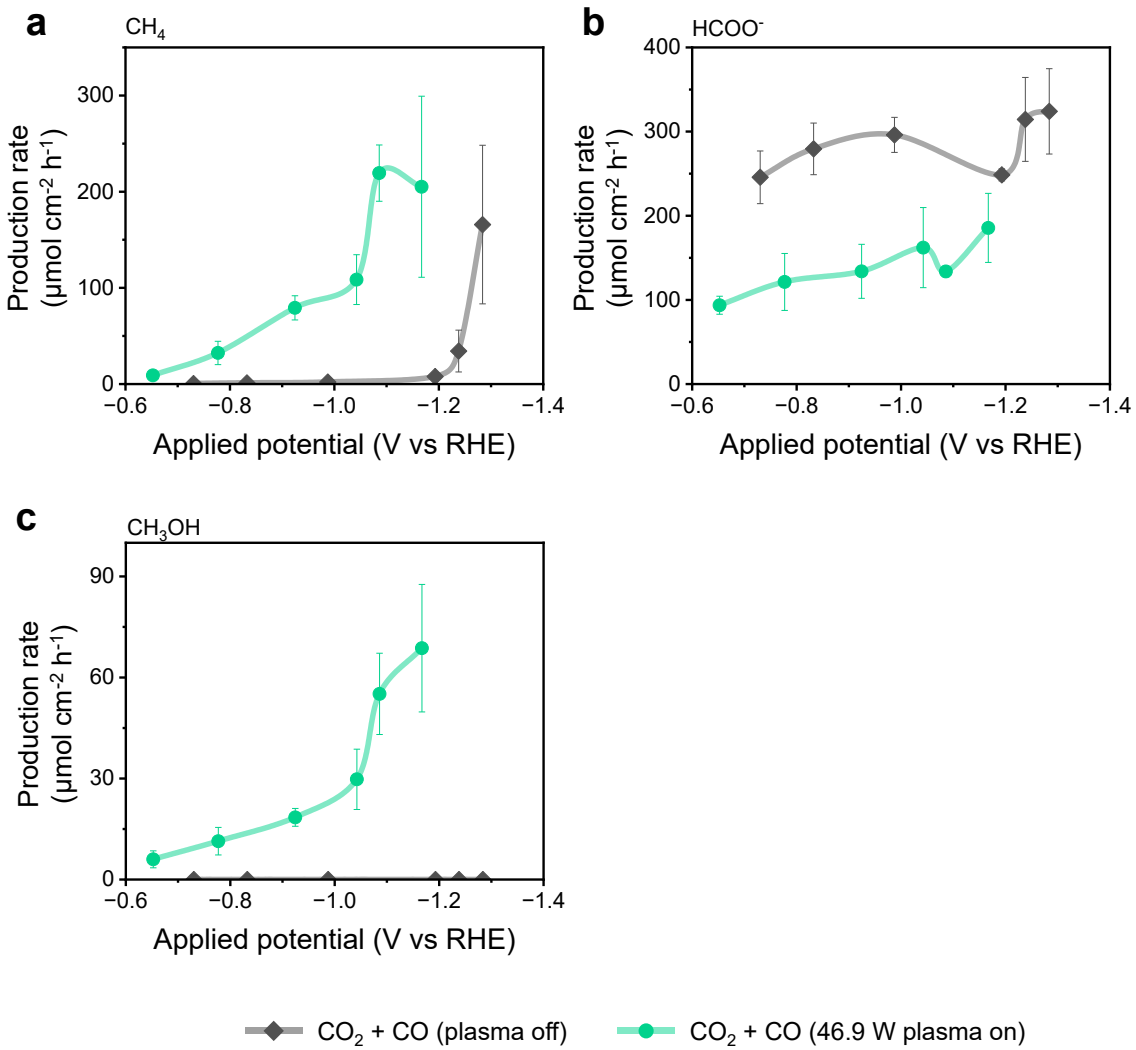
406



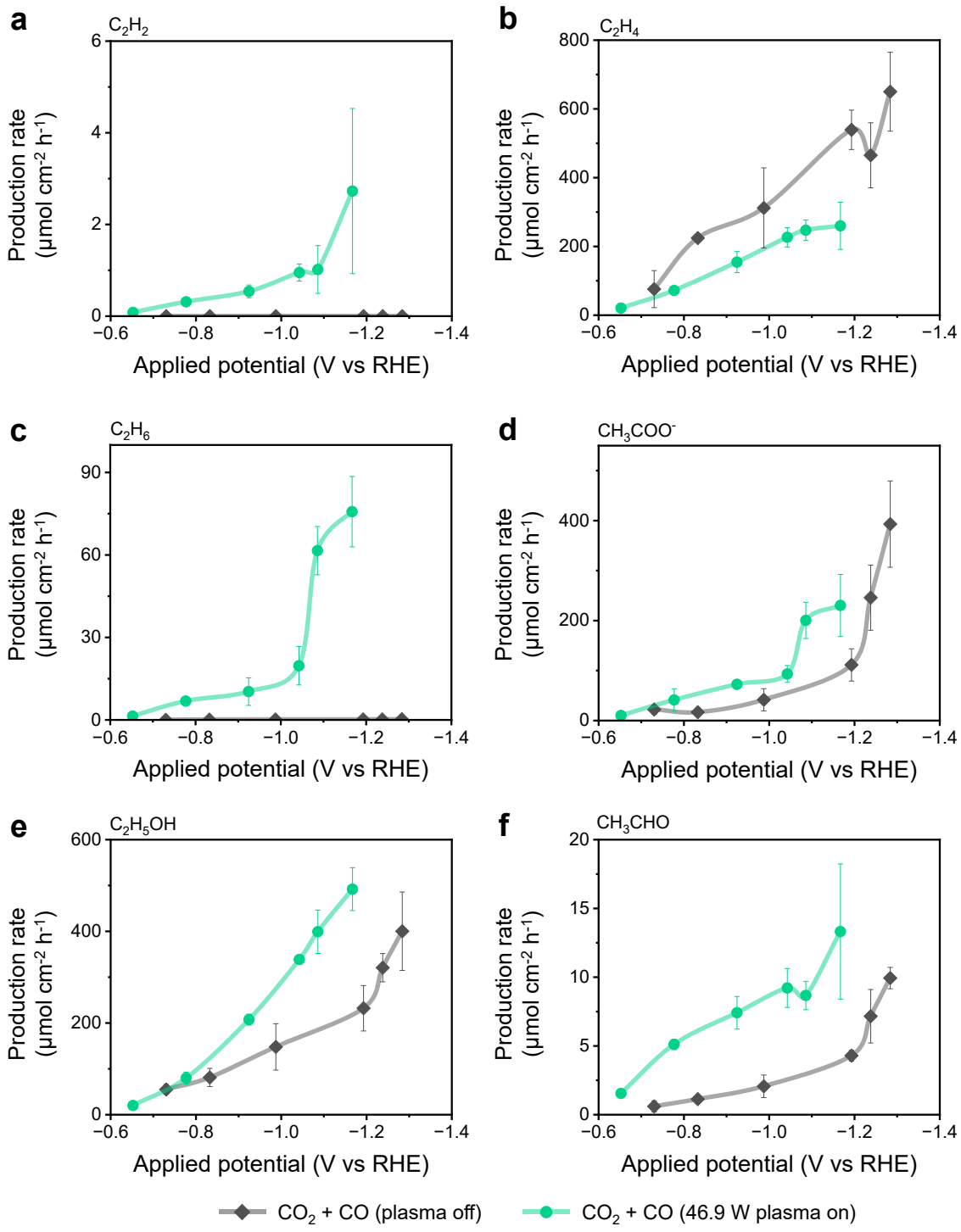
407

408 **Supplementary Fig. 35 | Tafel slope analysis for plasma-activated versus ground-state CO_2+CO**
409 **electroreduction.** The Tafel plots were obtained in the potential range where the slopes remain constant.
410 Potential was swept at the scan rate of 1 mV sec^{-1} with and without plasma activation of CO_2+CO in 1
411 M KOH electrolyte. A mixed gas of CO_2+CO+He was supplied with a ratio of 3:1:1.

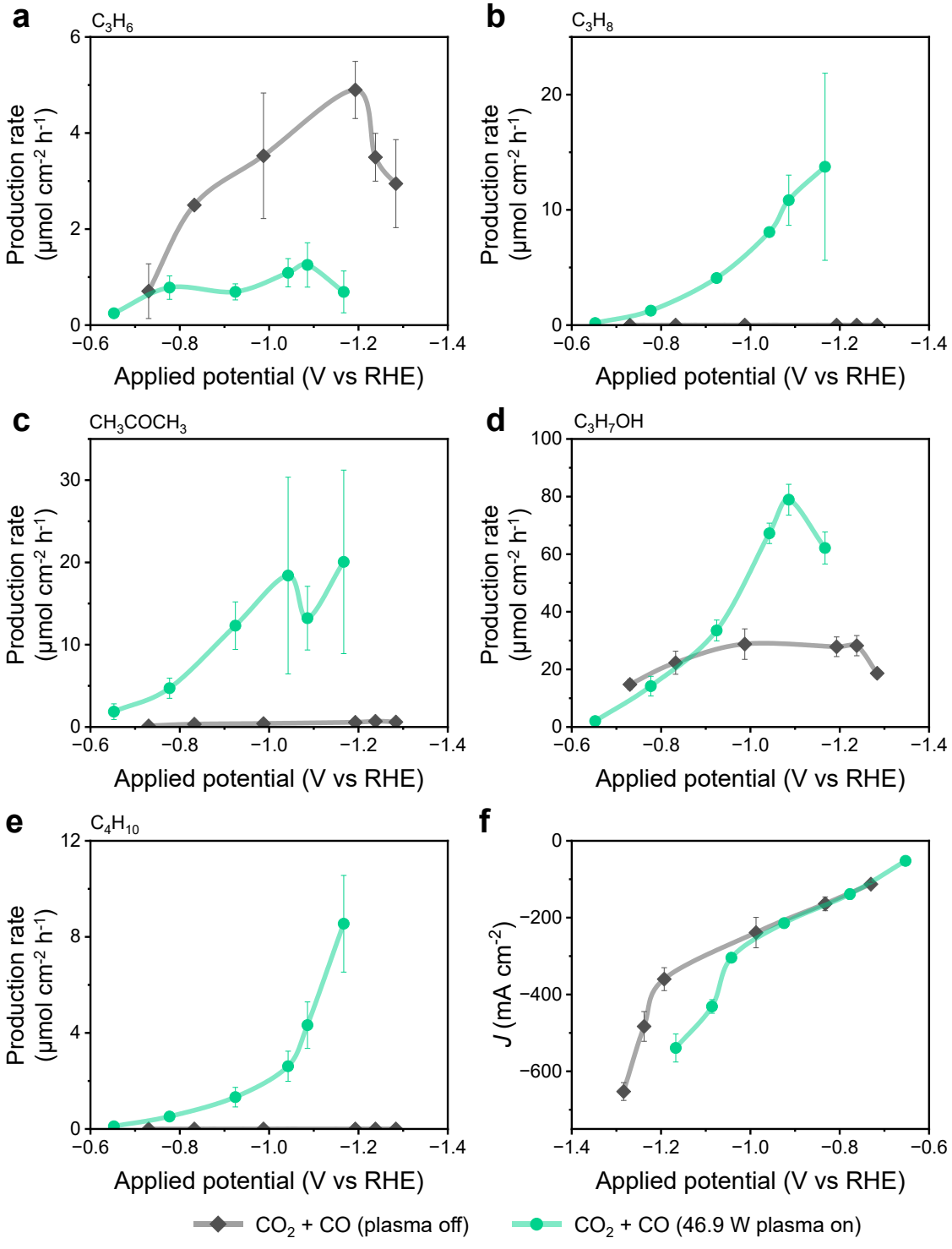
412



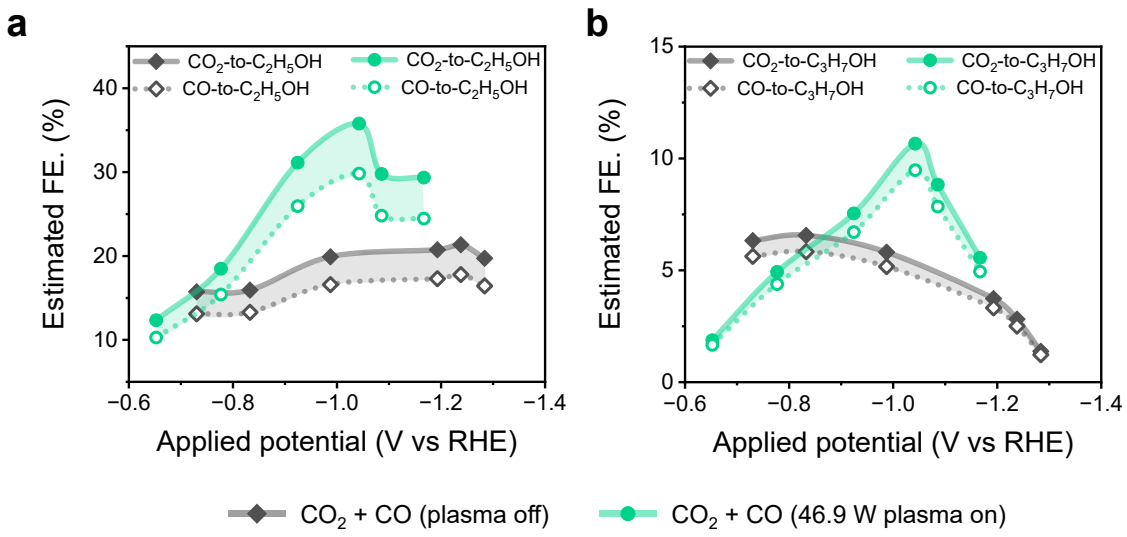
Supplementary Fig. 36 | **a-c,** Evaluation of C_1 product formation during electroreduction of ground state (plasma off) CO_2 + CO and 46.9 W plasma-activated CO_2 + CO. Comparison of production rates of (**a**) CH_4, (**b**) $HCOO^-$, and (**c**) CH_3OH versus applied potential. A mixed gas feed consisting of 30 ml min^{-1} CO_2, 10 ml min^{-1} CO, and 10 ml min^{-1} He was used. Each data point represents the mean and standard deviation of three independent measurements. At -1.2 V for plasma-electrocatalytic experiments, three independent samples (six in total) were additionally analyzed to improve the reliability of the measurements.



Supplementary Fig. 37 | **a-f,** Evaluation of C_2 product formation during electroreduction of ground state (plasma off) CO_2 + CO and 46.9 W plasma-activated CO_2+CO. Comparison of production rates of (**a**) C_2H_2, (**b**) C_2H_4, (**c**) C_2H_6, (**d**) CH_3COO^-, (**e**) C_2H_5OH, and (**f**) CH_3CHO versus applied potential. A mixed gas feed consisting of 30 ml min^{-1} CO_2, 10 ml min^{-1} CO, and 10 ml min^{-1} He was used. Each data point represents the mean and standard deviation of three independent measurements. At -1.2 V for plasma-electrocatalytic experiments, three independent samples (six in total) were additionally analyzed to improve the reliability of the measurements.

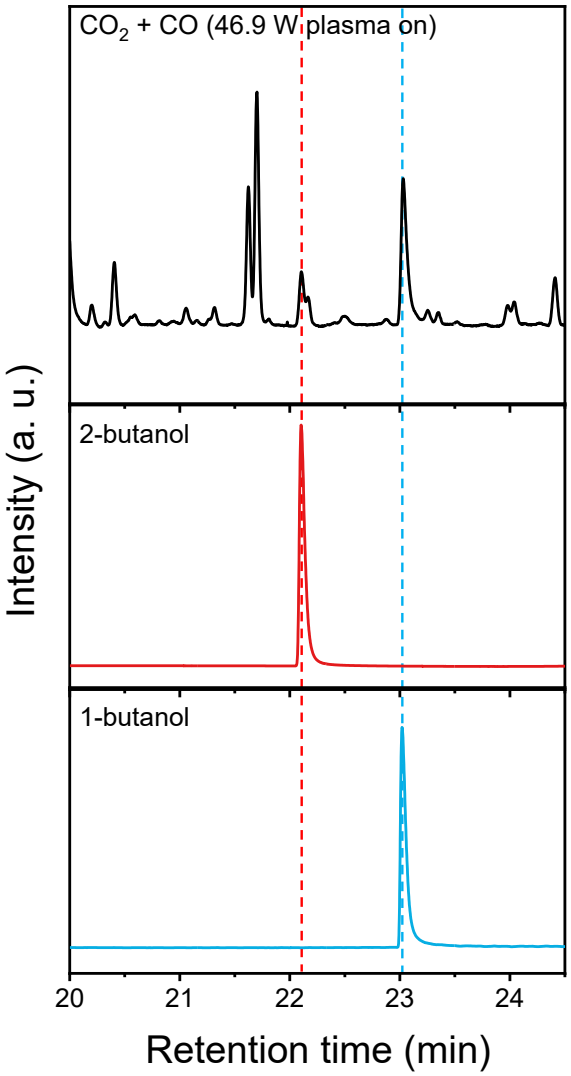


Supplementary Fig. 38 | **a-f,** Evaluation of C_{3+} product formation and total reaction activity during electroreduction of ground state (plasma off) CO_2 + CO and 46.9 W plasma-activated CO_2+CO. Comparison of production rates of (**a**) C_3H_6, (**b**) C_3H_8, (**c**) CH_3COCH_3, (**d**) C_3H_7OH, (**e**) C_4H_{10}, and (**f**) total *J* versus applied potential. A mixed gas feed consisting of 30 ml min^{-1} CO_2, 10 ml min^{-1} CO, and 10 ml min^{-1} He was used. Each data point represents the mean and standard deviation of three independent measurements. At -1.2 V for plasma-electrocatalytic experiments, three independent samples (six in total) were additionally analyzed to improve the reliability of the measurements.

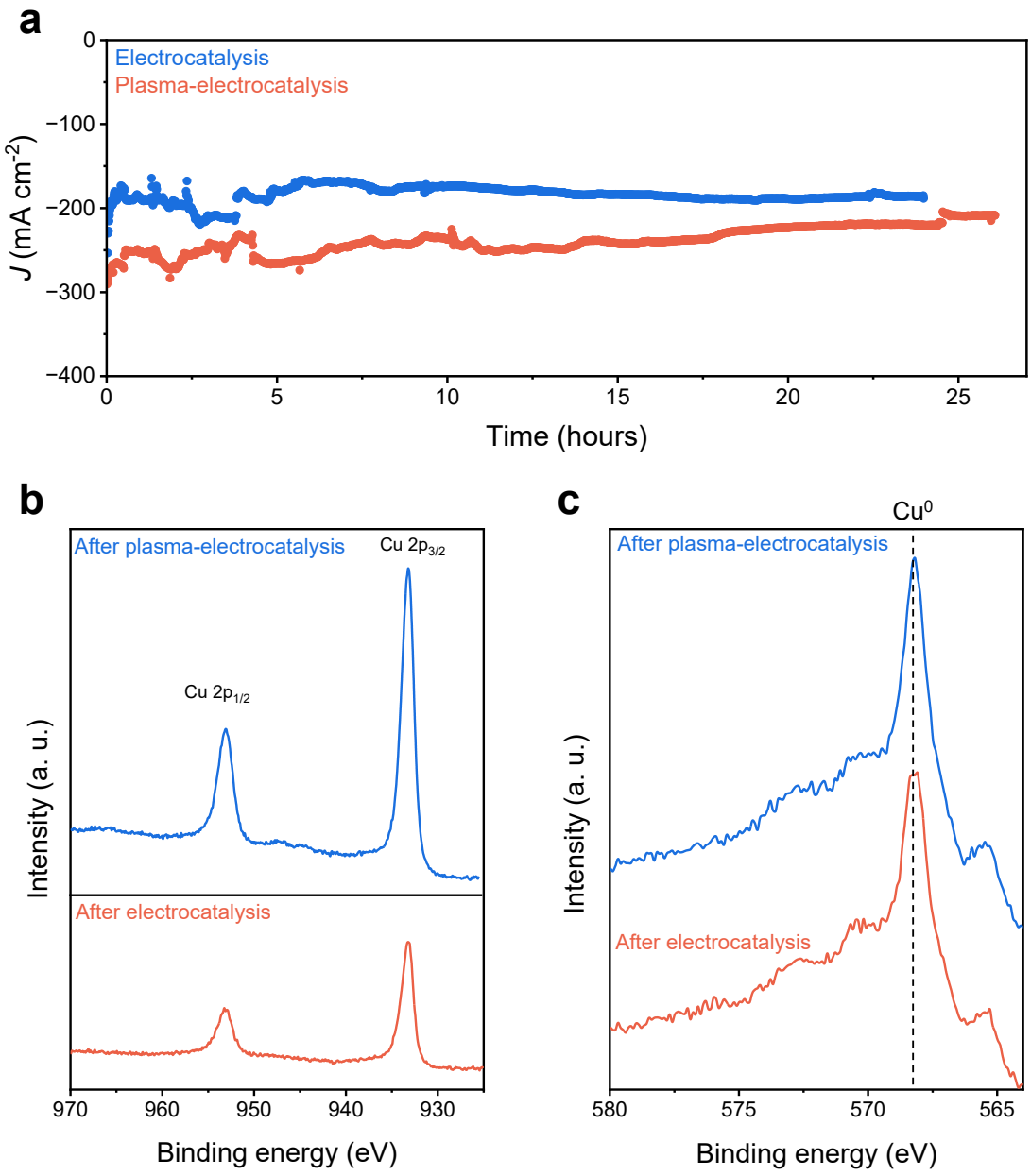


439

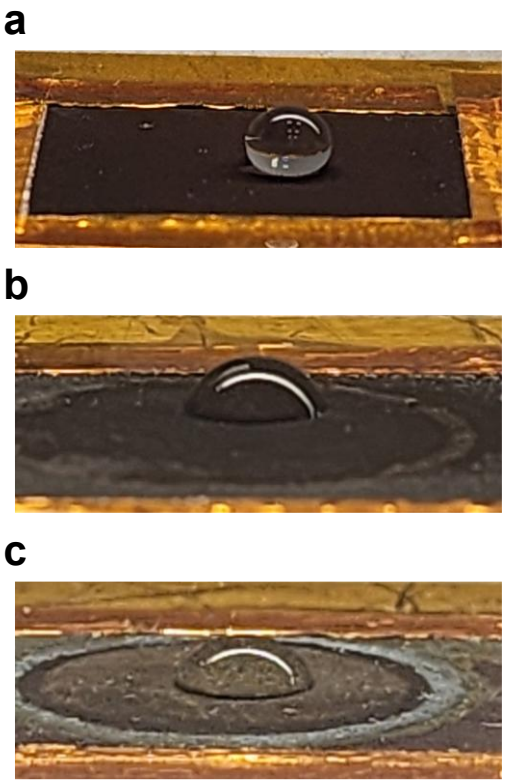
440 **Supplementary Fig. 39 | Electrocatalytic alcohols generation using plasma-activated (plasma on)**
441 **and ground state (plasma off) CO_2 and CO conversion. a-b,** Alcohols selectivity was compared
442 between plasma-activated CO_2 + CO (plasma on) with ground-state CO_2 + CO (plasma-off)
443 electroreduction. Estimated FE for (**a**) C_2H_5OH and (**b**) C_3H_7OH, where FE was calculated by assuming
444 either pure CO_2 or pure CO as the reactant. A mixed gas feed of CO_2 (30 mL min^{-1}), CO (10 mL min^{-1}),
445 and He (10 mL min^{-1}) was supplied, with/without a plasma power input of 46.9 W. All measurements
446 were conducted in 1 M KOH electrolyte. Each data point in (**a**) and (**b**) represents the mean and standard
447 deviation of three independent measurements. At -1.2 V for plasma-electrocatalytic experiments, three
448 independent samples (six in total) were additionally analyzed to improve the reliability of the
449 measurements.



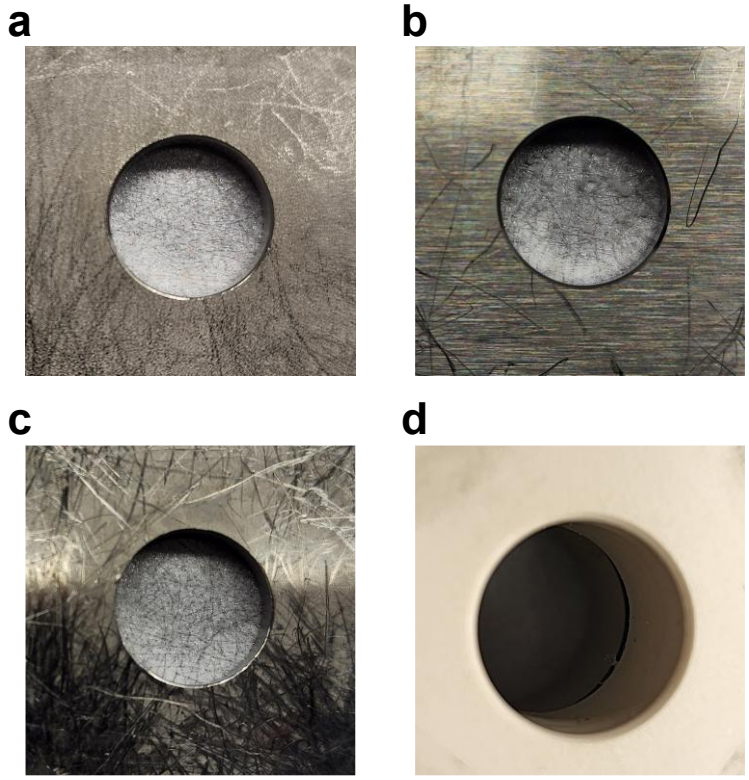
Supplementary Fig. 40 | FID gas chromatogram of electroreduction of 46.9 W plasma-activated CO_2+CO at -1.1 V, magnified around 1, 2-butanol peaks (top). Standard chemicals were analyzed (2-butanol, middle, and 1-butanol, bottom). The flow rates of gases in the mixed feed were 30 ml min^{-1} CO_2 + 10 ml min^{-1} He + 10 ml min^{-1} CO. The reaction was conducted in 1 M KOH electrolyte.



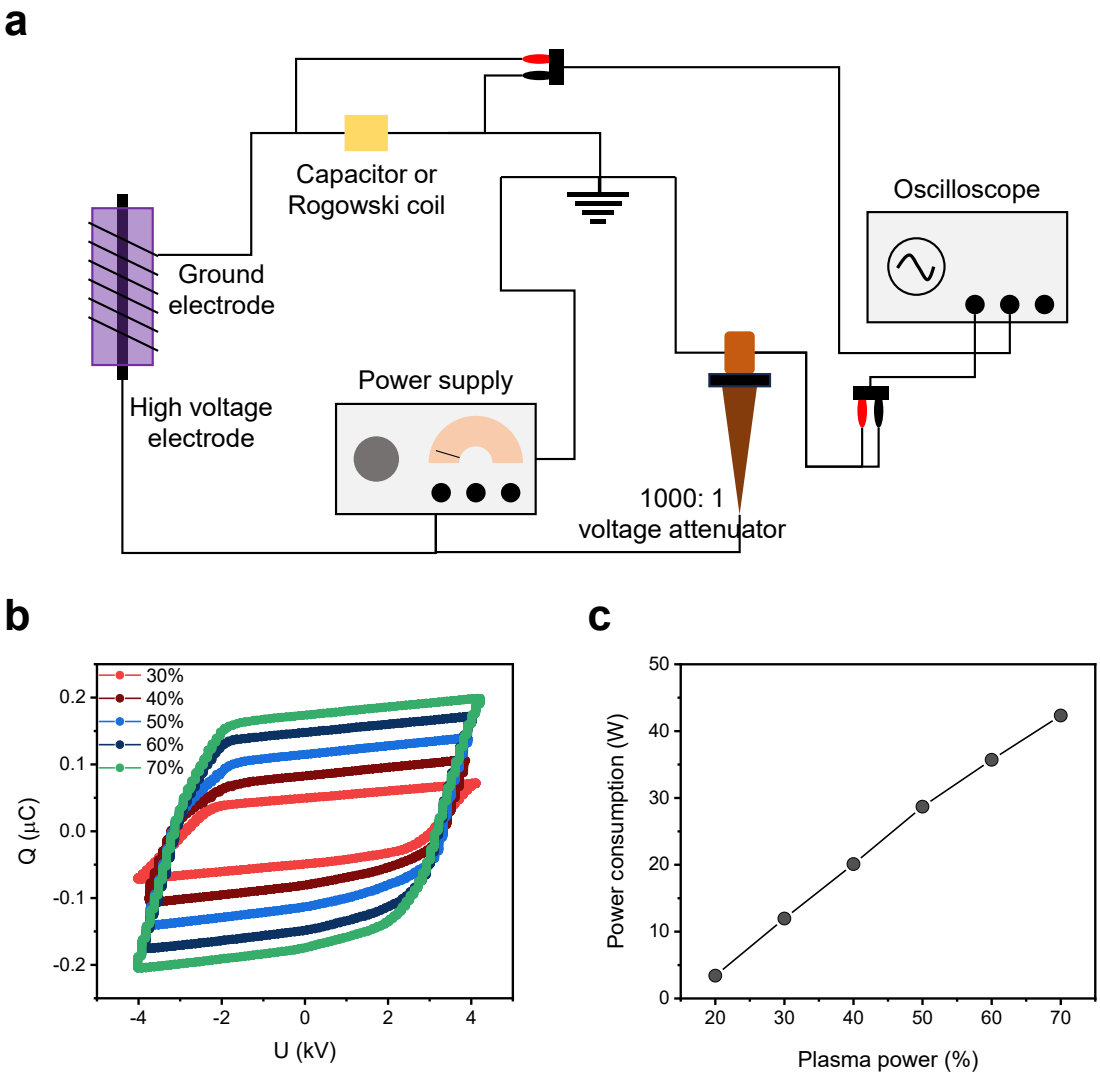
Supplementary Fig. 41 | Long-term operation of plasma-electrocatalysis and electrocatalysis, and post-reaction chemical state analysis of Cu catalysts. a, Evolution of total current density during prolonged operation at a constant potential of -1.4 V (vs. RHE, before IR compensation). A mixed gas feed of CO_2 (30 mL min^{-1}), CO (10 mL min^{-1}), and He (10 mL min^{-1}) was supplied. 1 M KOH solution was used as an electrolyte. **b-c,** Post-reaction analysis on catalyst chemical state. (**b**) Cu 2p XPS spectra and (**c**) Cu LMM Auger spectra after 25 hours of operation. The surface layer was etched before XPS analysis using a C_{60} gun. Peaks were calibrated based on C 1s spectrum as an internal standard.



Supplementary Fig. 42 | Surface hydrophobicity of Cu GDEs before and after reactions. Water droplet contact--angle images were collected to evaluate changes in surface hydrophobicity of Cu GDE. **a,** Water contact image of the Cu GDE before reaction. **b,** Water contact image after electrocatalysis-only reaction. **c,** Image after plasma-electrocatalysis. Reactions were conducted for 2 hours at an applied potential of -2 V (vs. RHE, before IR compensation) in 1 M KOH electrolyte with a mixed gas feed of CO_2 (30 mL min^{-1}), CO (10 mL min^{-1}), and He (10 mL min^{-1}). Gas was plasma-activated at a power input of 46.9 W.

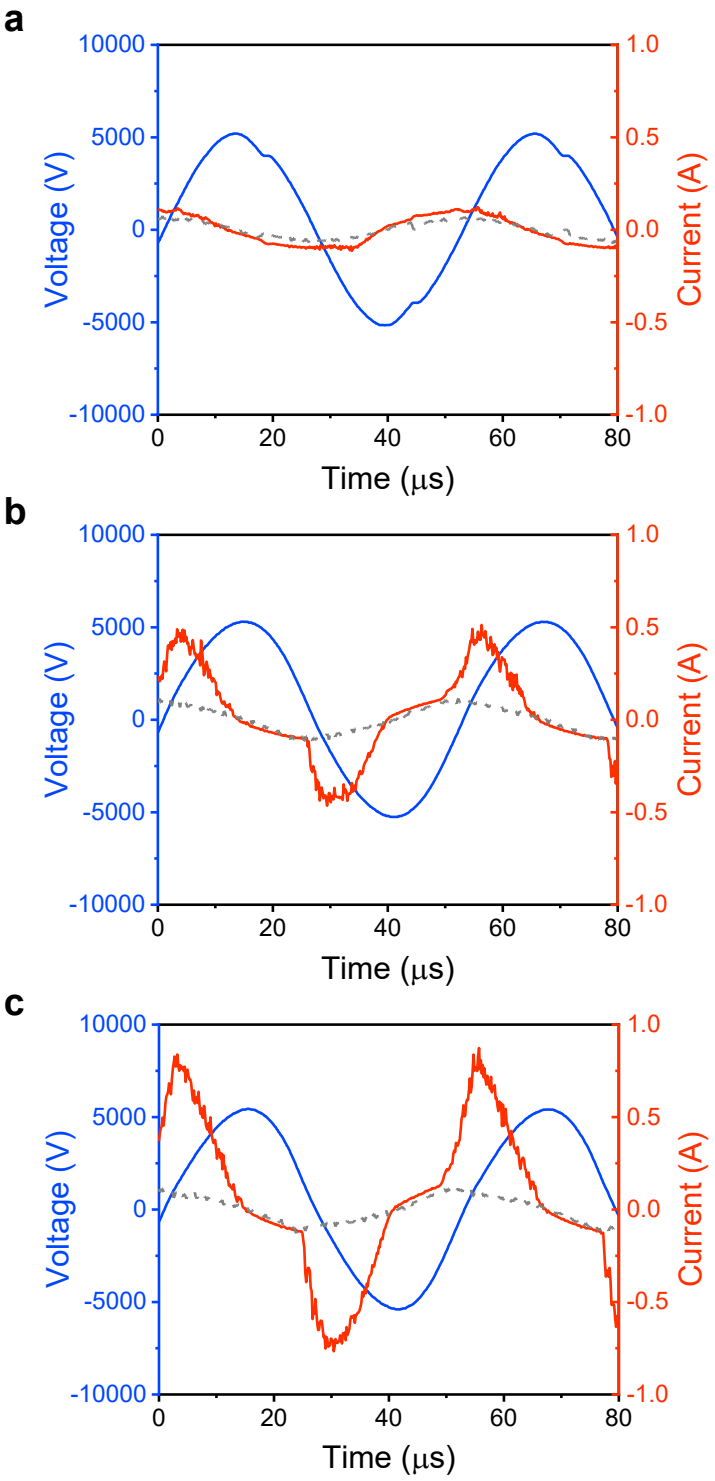


Supplementary Fig. 43 | Post-reaction images of the GDE backside and plasma-electrocatalysis coupling region. a, Image of GDE backside before reaction. **b,** Backside view of the GDE after electrocatalysis-only conversion. **c,** Backside view of the GDE after plasma-electrocatalysis. **d,** Image of the gas transport pathway following a series of electrocatalytic and plasma-electrocatalytic experiments.

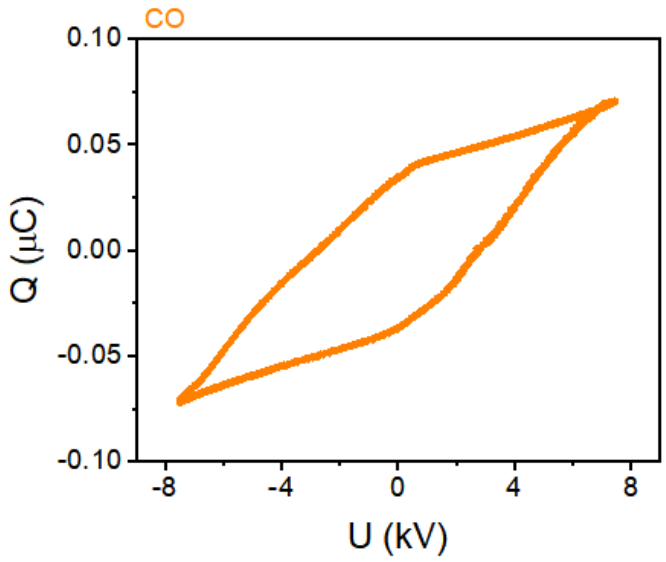


482

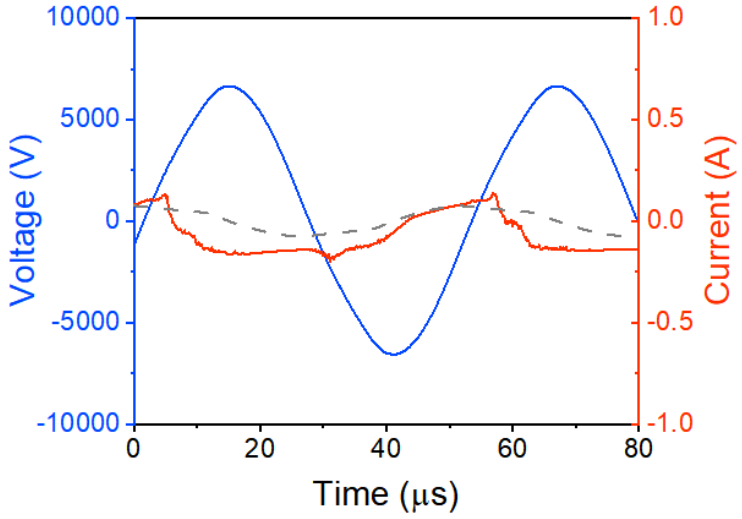
483 **Supplementary Fig. 44 | a-c,** Measurement of power consumption and microdischarge current of DBD
484 plasma. (**a**) Electrical circuit for the measurements, including a capacitor for power measurements and
485 a Rogowski coil for microdischarge analysis. (**b**) Lissajous plots of CO_2 plasma at different powers. (**c**)
486 Power consumption was measured using the internal area of the Lissajous plots. A mixed gas feed
487 consisting of 40 ml min^{-1} CO_2 and 10 ml min^{-1} He was supplied.



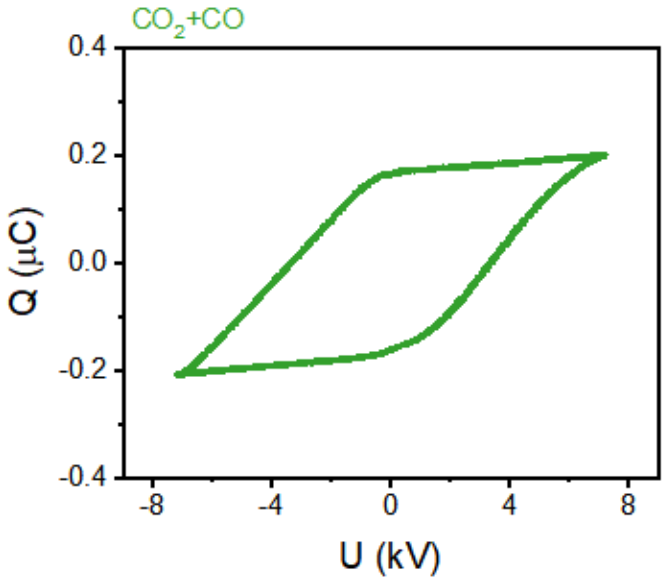
Supplementary Fig. 45 | **a-f,** Measurements and characterization of microdischarge current of CO_2 plasma at **a,** 12.0 W, **b,** 28.7 W, and **c,** 42.3 W. A mixed gas feed consisting of 40 ml min^{-1} CO_2 and 10 ml min^{-1} He was supplied. Measurements were processed based on previous work.[26] Blue and red lines show voltage and microdischarge current, respectively. The grey dashed line represents displacement current.



Supplementary Fig. 46 | Lissajous plot of 10.8 W plasma-activated CO. A mixed gas feed consisting of 30 ml min^{-1} CO and 20 ml min^{-1} He was supplied.

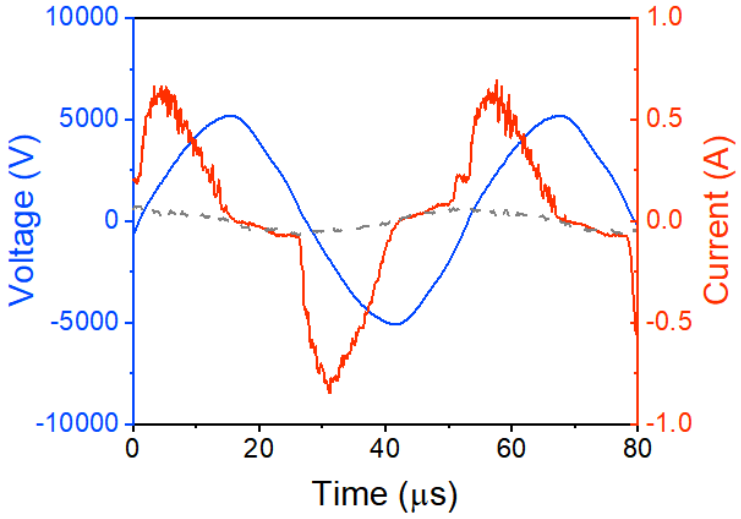


Supplementary Fig. 47 | Measurement and characterization of microdischarge current of CO plasma at 10.8 W. A mixed gas feed consisting of 30 ml min^{-1} CO and 20 ml min^{-1} He was supplied. Measurements were processed based on previous work.[26] Blue and red lines show voltage and microdischarge current. The grey dashed line represents displacement current.



503

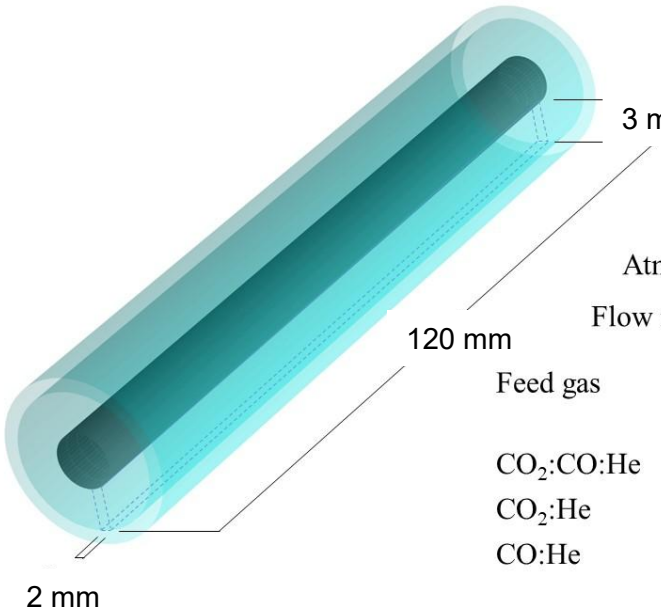
504 **Supplementary Fig. 48** | Lissajous plot of 46.9 W plasma-activated CO_2+CO. A mixed gas feed
505 consisting of 30 ml min^{-1} CO_2, 10 ml min^{-1} CO, and 10 ml min^{-1} He was supplied.



506

507 **Supplementary Fig. 49 | a-b,** Measurement and characterization of microdischarge current of CO_2+CO
508 plasma at 46.9 W. A mixed gas feed consisting of 30 ml min^{-1} CO_2, 10 ml min^{-1} CO, and 10 ml min^{-1}
509 He was supplied. Measurements were processed based on previous work.[26] Blue and red lines show
510 voltage and microdischarge current. The grey dashed line represents displacement current.

511



Simulation conditions

Atmospheric pressure, $T_g = 400$ K

Flow rate = 50 mL/min × V_{slice} / $V_{reactor}$

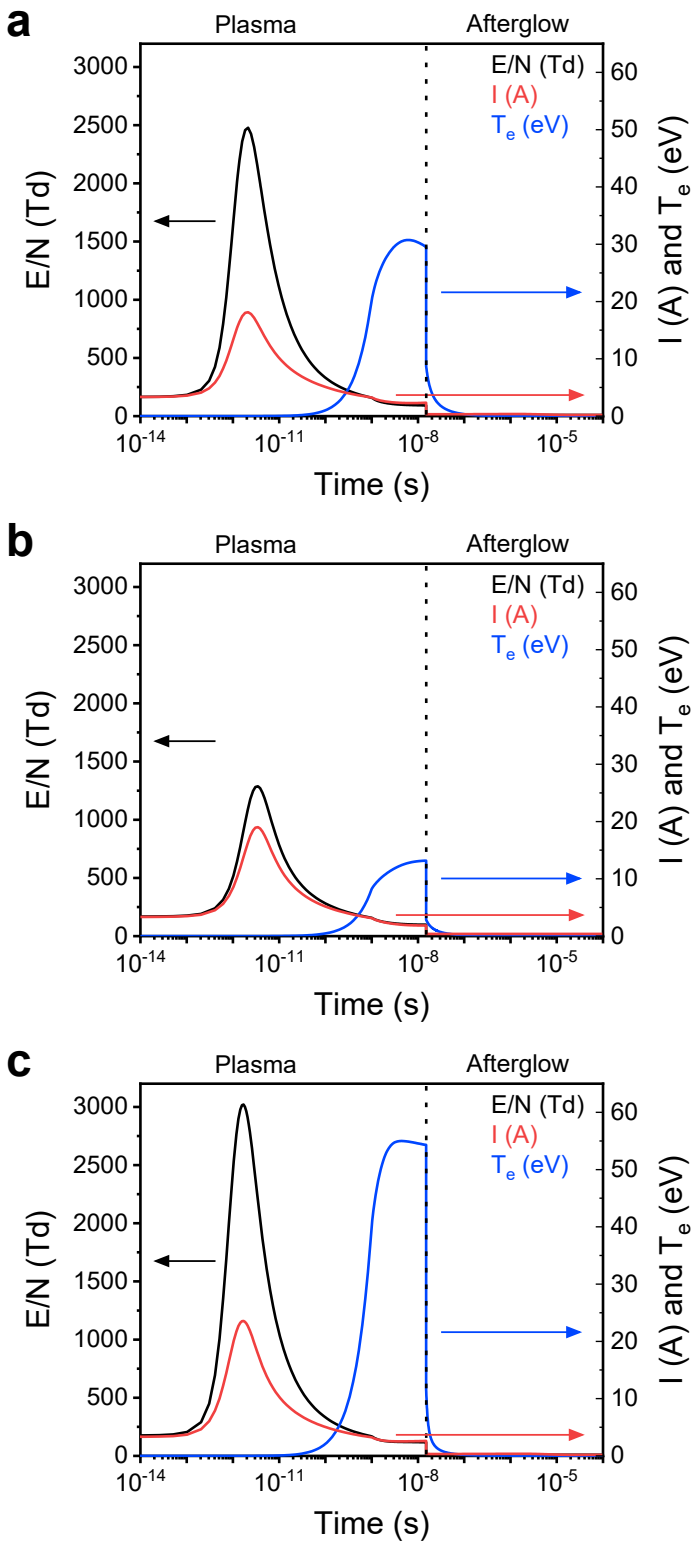
Feed gas	Feed ratio	Power (W)	Power per µdischarge (kW)
CO_2:CO:He	60:20:20	46.9	378
CO_2:He	80:20	42.3	186
CO:He	60:40	10.8	71

512

513 **Supplementary Fig. 50** | Modeling conditions for plasma simulation. Sketch of the plasma zone, with
514 simulation volume outlined by dashed boundaries. Simulation conditions are described.

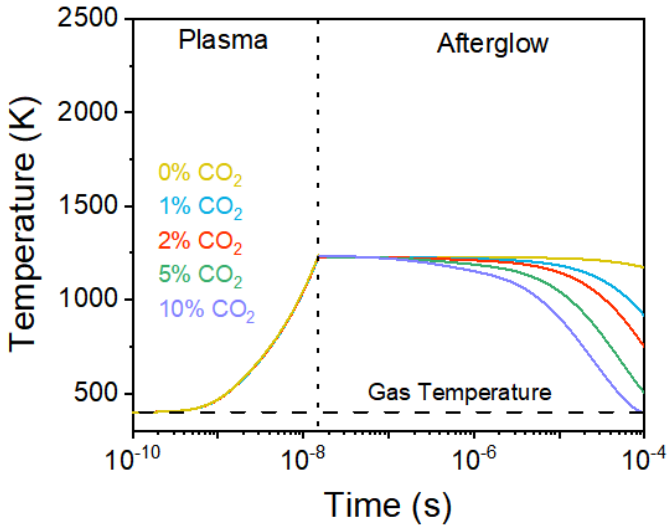
515

516



517

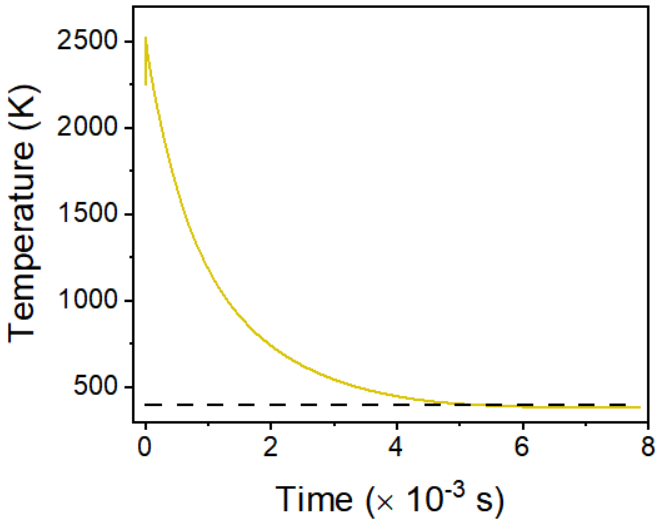
518 **Supplementary Fig. 51** | Calculated reduced electric field (E/N, i.e., ratio of electric field over gas
519 number density), current (I) and electron temperature (T_e) as a function of time for the first pulse for (**a**)
520 80% CO_2 + 20% He, (**b**) 60% CO + 40% He, and (**c**) 60% CO_2 + 20% CO + 20% He. The end of the
521 plasma pulse and the beginning of the afterglow region are marked by a vertical dashed line.



522

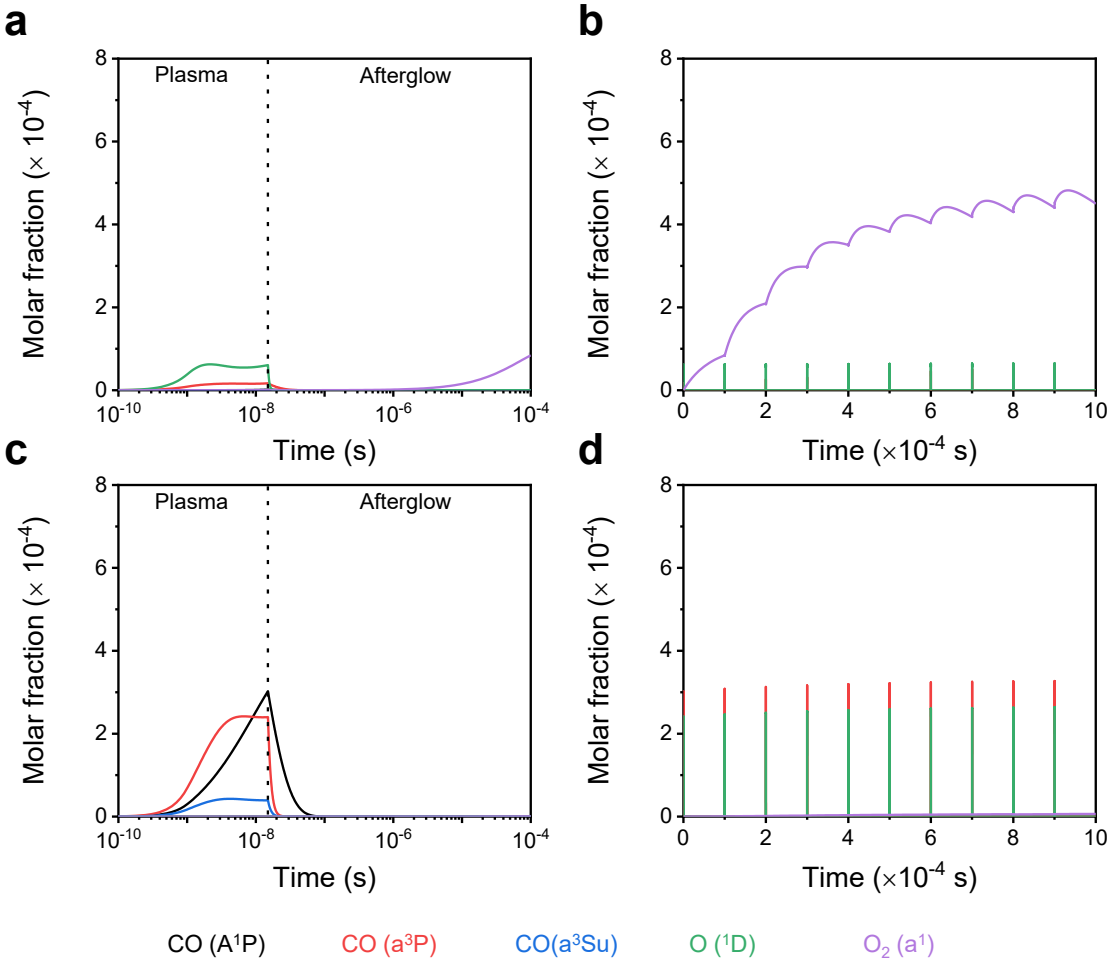
523 **Supplementary Fig. 52 |** Effect of CO_2 addition on vibrational mode of CO (T_{CO}). Simulated time
524 evolution of T_{CO} during the first pulse when CO_2 was added to 60% CO + 40% He. When CO_2 was
525 added, the same amount of CO was removed from the feed gas mixture.

526



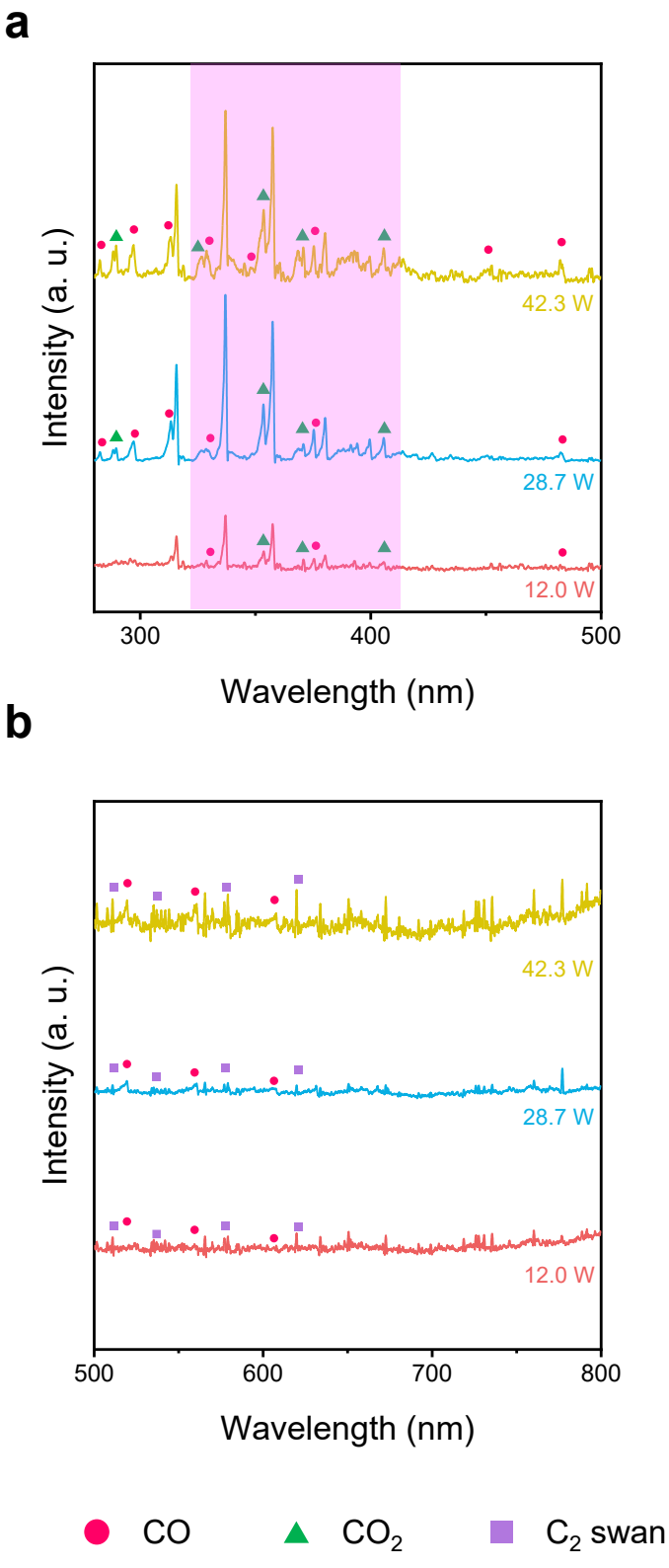
527

528 **Supplementary Fig. 53 |** Relaxation of vibrational mode of CO. Time evolution of T_{CO} in the afterglow
529 after the 10th consecutive pulse for 60% CO + 40% He.

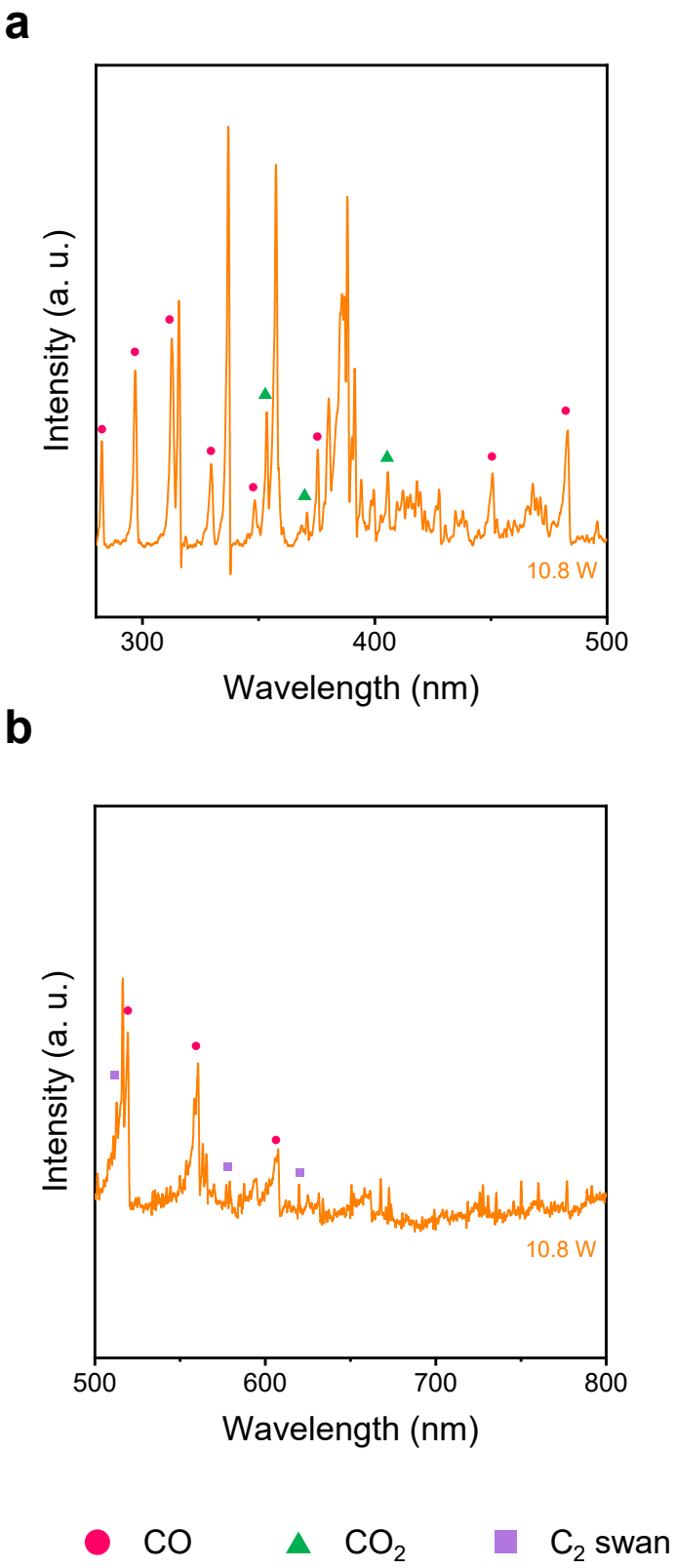


530

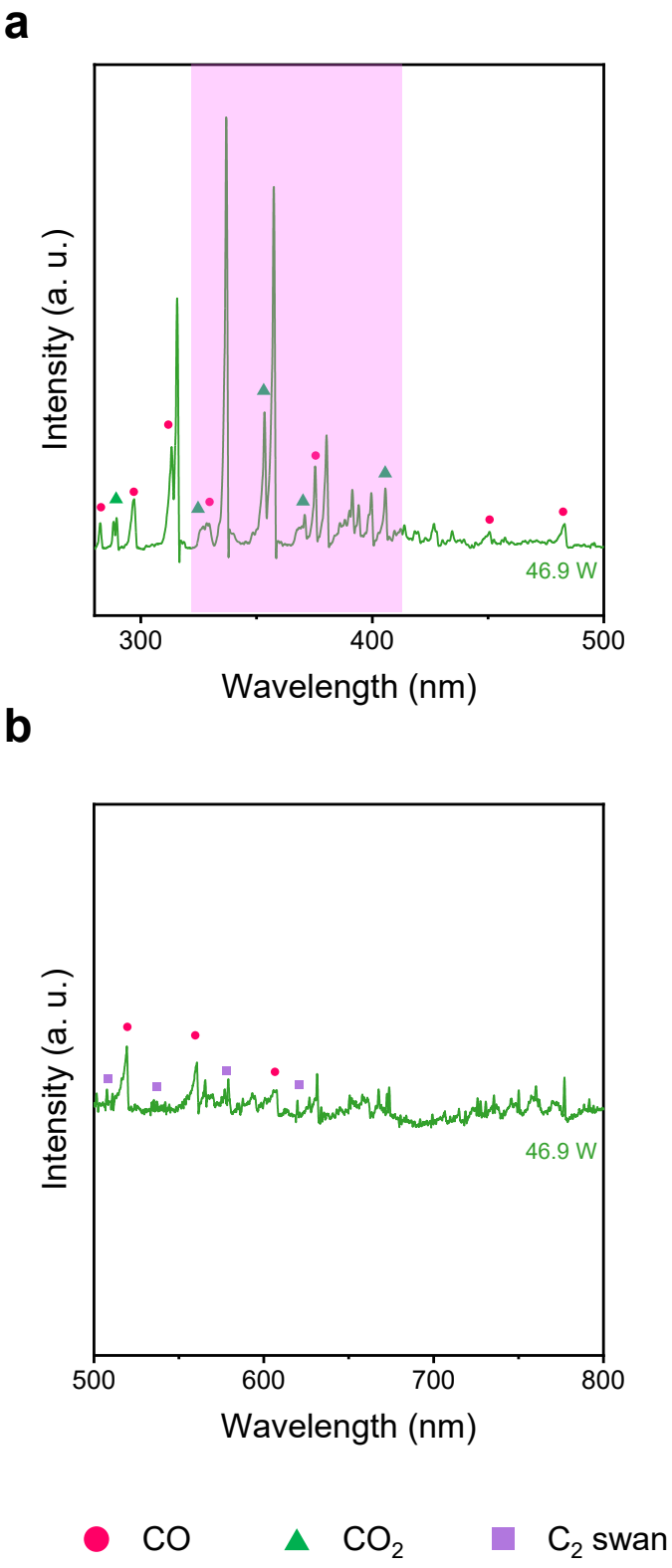
531 **Supplementary Fig. 54** | Simulated molar fractions of the main electronically excited species as a
532 function of time for **a-b,** 80% CO_2 + 20% He and **c-d,** 60% CO + 40% He. (**a, c**) Evolution of
533 electronically excited species during the first pulse and (**b, d**) over 10 consecutive pulses. $CO(A^1P)$,
534 $CO(a^3P)$, $CO(a^3Su)$, $O(^1D)$, and $O_2(a^1)$ stand for $CO(A^1\pi)$, $CO(a^3\pi)$, $CO(a'^3\Sigma^+)$, $O(^1D)$, and $O_2(a^1\Delta_g)$,
535 respectively.



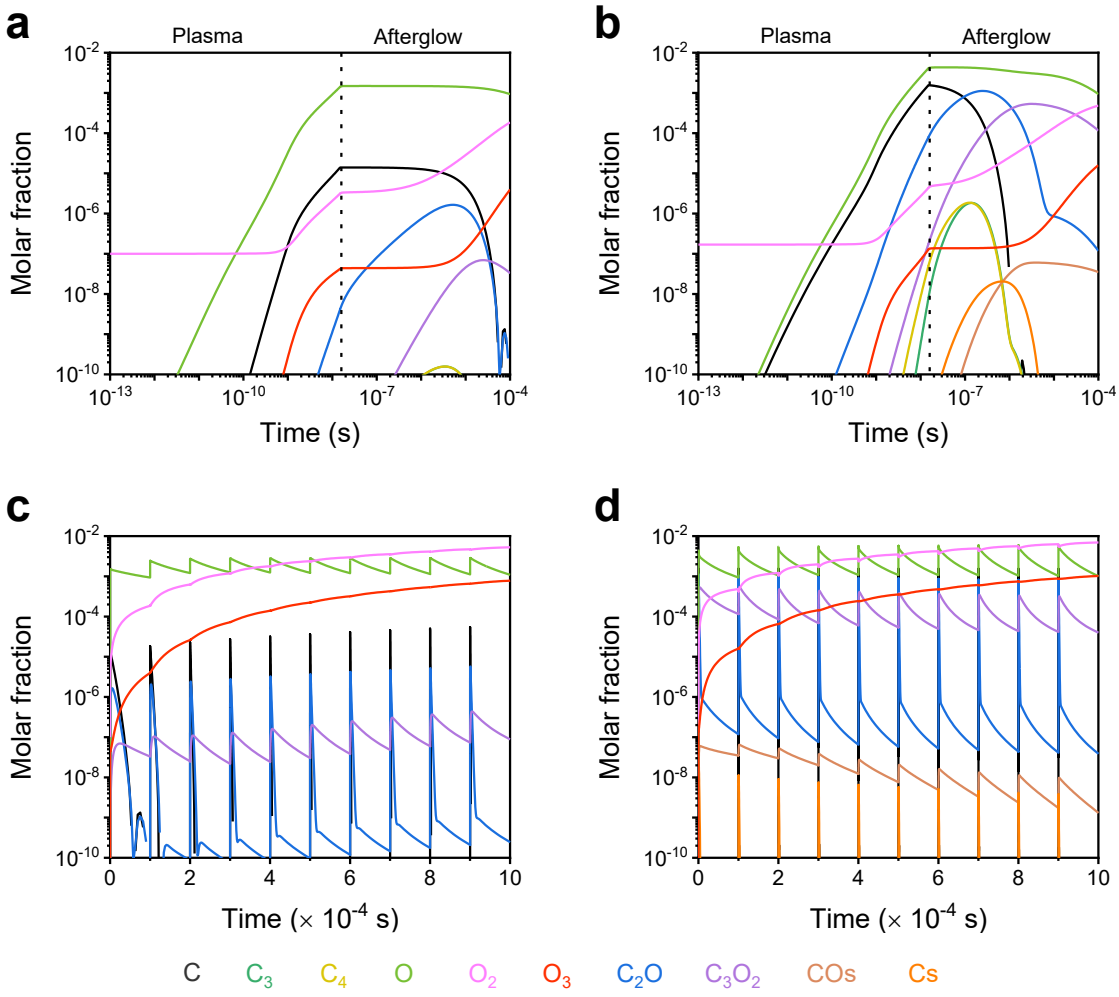
Supplementary Fig. 55 | a-b, (**a**) Optical emission spectra (OES) of plasma-activated CO_2 at different plasma powers. Spectra were acquired in the wavelength range of (**a**) 250 to 500 nm and (**b**) 500 to 800 nm for 500 ms. A mixed gas feed consisting of 40 ml min^{-1} CO_2 and 10 ml min^{-1} He was supplied. Highlighted region in pink indicates electrically excited CO_2 band.



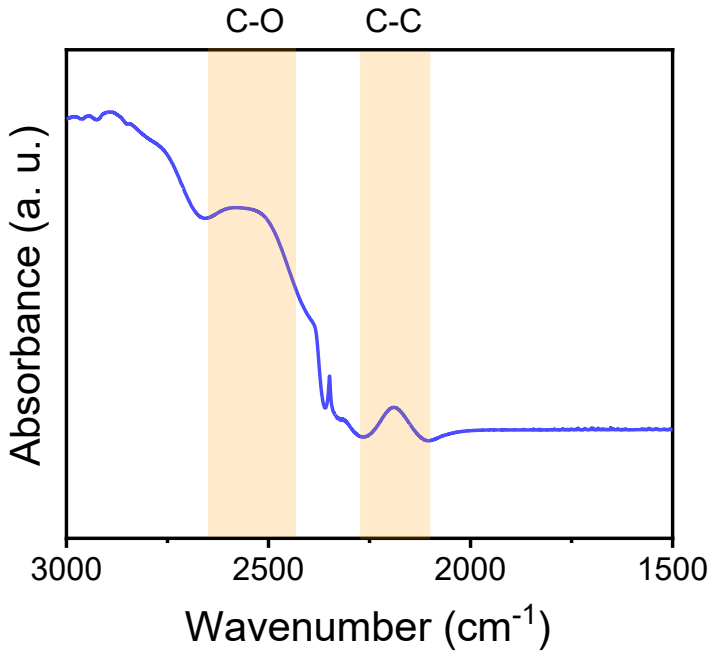
Supplementary Fig. 56 | a-b, (**a**) OES of plasma-activated CO at 10.8 W plasma power. Spectra were acquired in the wavelength range of (**a**) 250 to 500 nm and (**b**) 500 to 800 nm for 500 ms. A mixed gas feed consisting of 30 ml min^{-1} CO and 20 ml min^{-1} He was supplied.



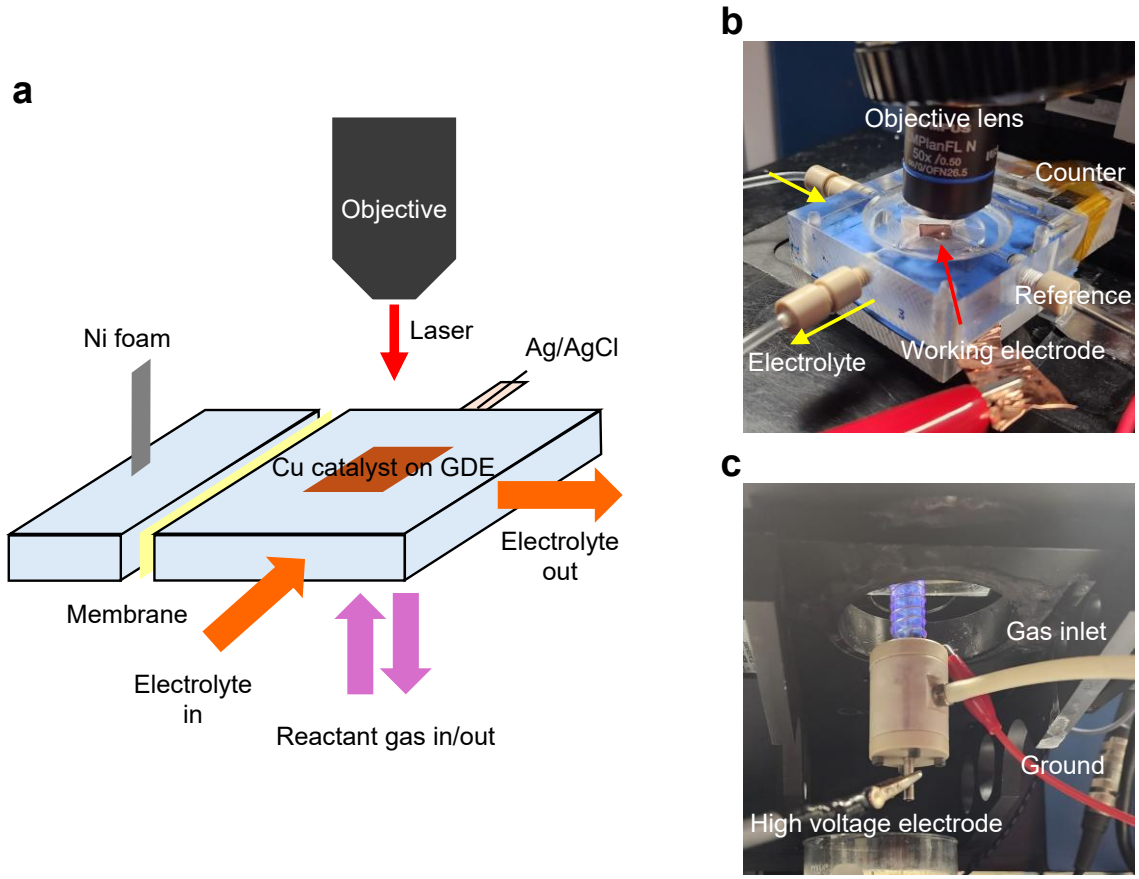
Supplementary Fig. 57 | **a-b,** (**a**) OES of plasma-activated CO_2 + CO at 46.9 W plasma power. Spectra were acquired in the wavelength range of (**a**) 250 to 500 nm and (**b**) 500 to 800 nm for 500 ms. A mixed gas feed consisting of 30 ml min^{-1} CO_2, 10 ml min^{-1} CO, and 10 ml min^{-1} He was supplied. Highlighted region in pink indicates electrically excited CO_2 band.



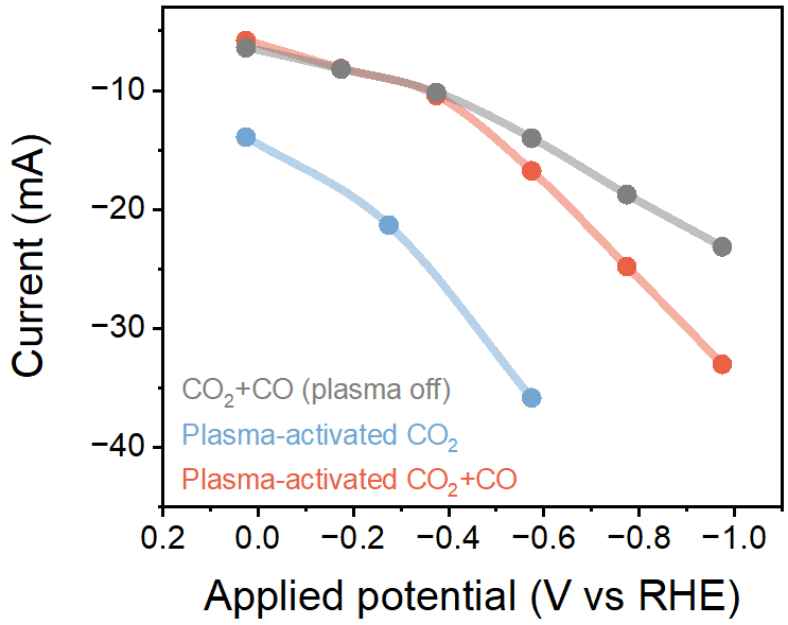
Supplementary Fig. 58 | Simulated ground state species concentrations. Temporal evolution of the molar fractions of the ground state species formed upon CO and CO_2 dissociation and recombination processes, **a-b,** during the first pulse for (**a**) 80% CO_2 + 20% He and (**b**) 60% CO_2 + 20% CO + 20% He, and **c-d,** over 10 consecutive pulses for (**c**) 80% CO_2 + 20% He and (**d**) 60% CO_2 + 20% CO + 20% He.



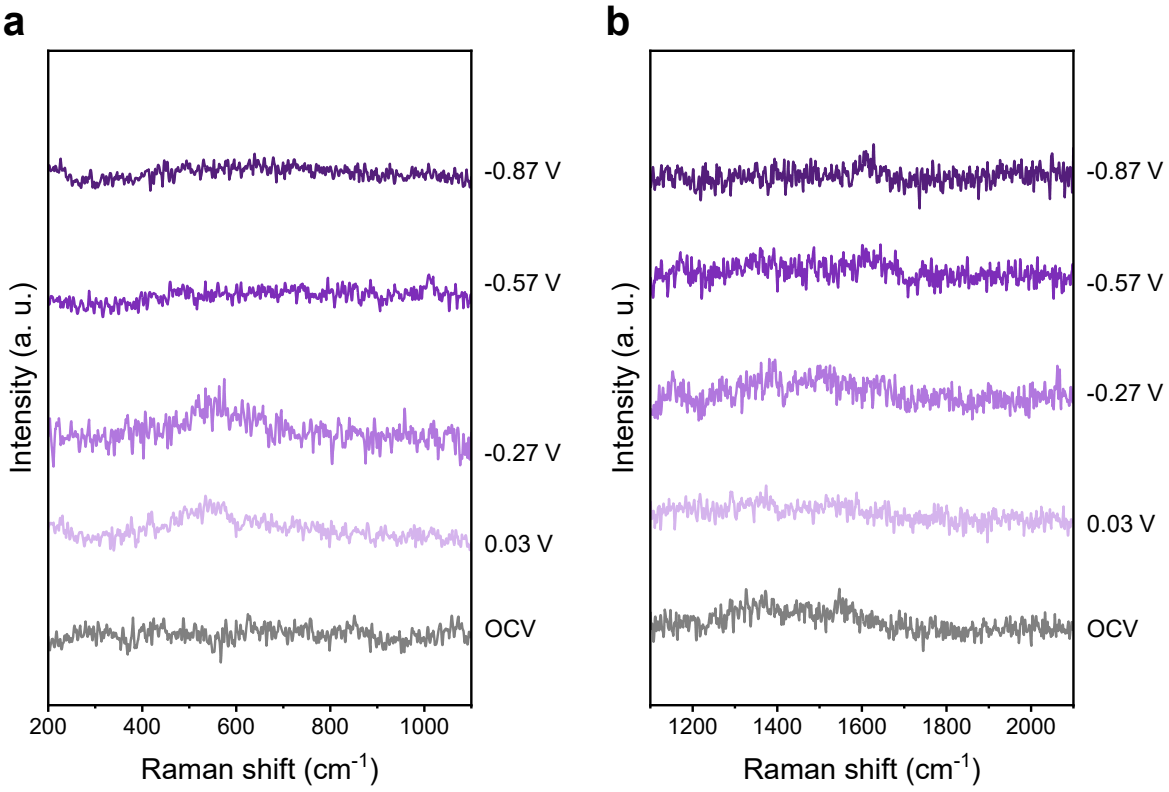
Supplementary Fig. 59 | Fourier transform infrared spectrum of deposited carbonaceous materials on KBr substrate placed in the location of the GDE in the plasma-electrocatalysis cell after ~30 hours of extended CO_2+CO plasma activation. A mixed gas feed consisting of 30 ml min^{-1} CO_2, 10 ml min^{-1} CO, and 10 ml min^{-1} He was supplied. The spectrum was baseline subtracted using a pristine substrate.



Supplementary Fig. 60 | Reactor setup for in situ Raman analysis in plasma-electrocatalysis. a, Schematic illustration of the plasma-electrocatalysis reactor configured for in situ Raman spectroscopy. Cu powder was loaded onto a commercial carbon GDE and was used as the working electrode. Ag/AgCl electrode and Ni foam were used as reference and counter electrodes, respectively. The cathode and anode compartments were separated by an anion exchange membrane to prevent possible oxidation of Cu during reactions. Aqueous 1 M KOH electrolyte was circulated through the cathode compartment. Plasma-activated or ground-state CO_2 + CO (mixed ratio = 3:1) was supplied from the bottom of the reactor. **b-c,** Photographs of the reactor showing the (**b**) upper and (**c**) lower parts in the Raman setup. Horiba LabRAM HR Evolution was used. The excitation source was a 633 nm laser with a power of 12.5 mW.



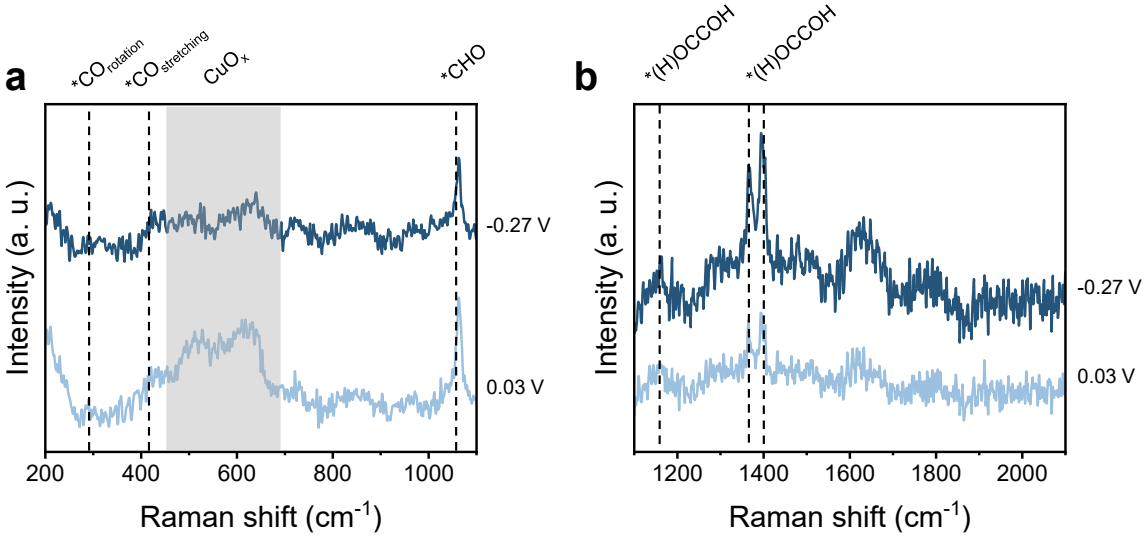
Supplementary Fig. 61 | Current for electrocatalytic CO_2+CO reduction (plasma off), CO_2 and CO_2+CO plasma-electrocatalysis in *in situ* Raman reactor. Reaction activity was evaluated by measuring total current under a series of constant potentials ranging from 0 to -1 V (vs RHE, before IR compensation). All measurements were performed in 1 M KOH electrolyte. Mixed gas feeds of CO_2+CO+He (ratio of 3:1:1) and CO_2 +He (ratio of 4:1) were supplied.



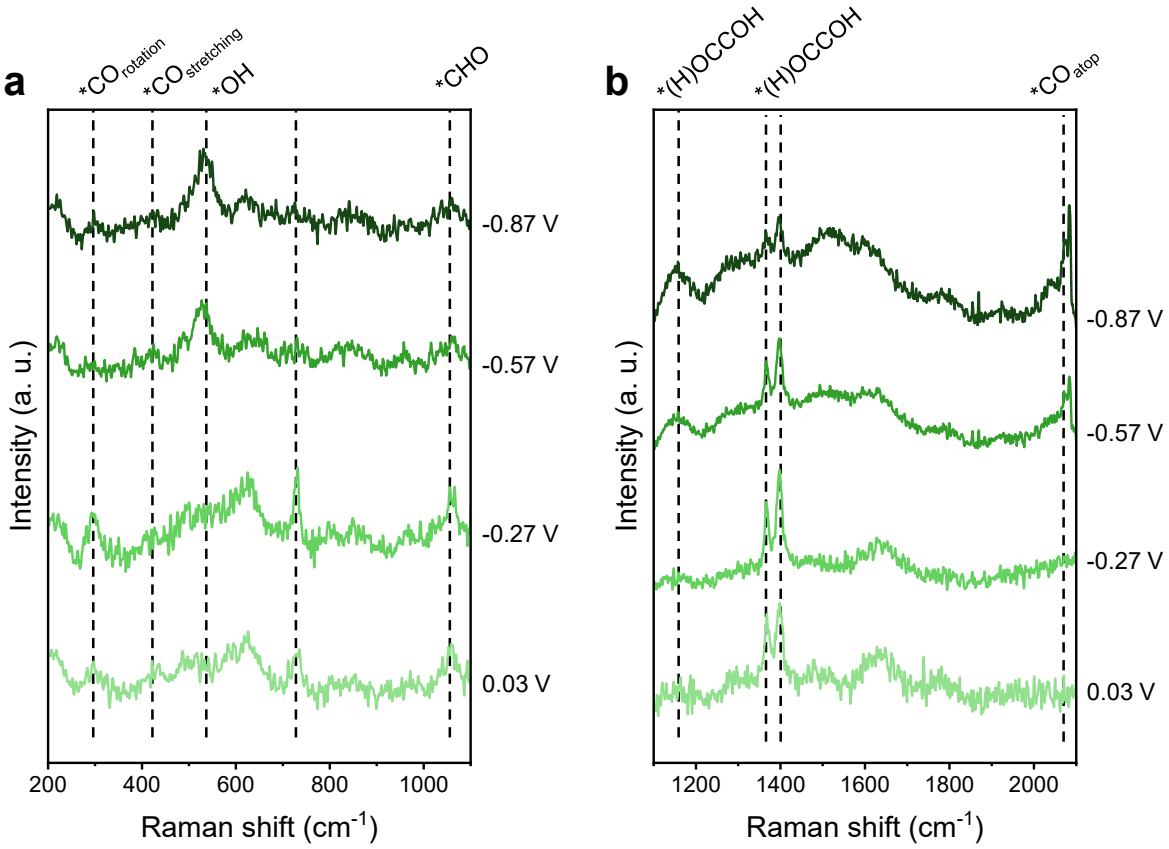
583

584 **Supplementary Fig. 62 | *In situ* spectroscopic investigation of surface intermediates in plasma-**
585 **activated He electroreduction. a-b,** *In situ* Raman spectra were collected to probe adsorbed reaction
586 intermediates on Cu catalysts in plasma-activated He electroreduction collected in the range of (**a**) 200-
587 1100 and (**b**) 1100-2100 cm^{-1}. Spectra were acquired at OCV and under applied potentials ranging from
588 0.03 to -0.87 V (vs. RHE, before IR compensation). Pure He was supplied during all measurements. 1
589 M KOH solution was used as electrolyte. The laser source was 633 nm.

590



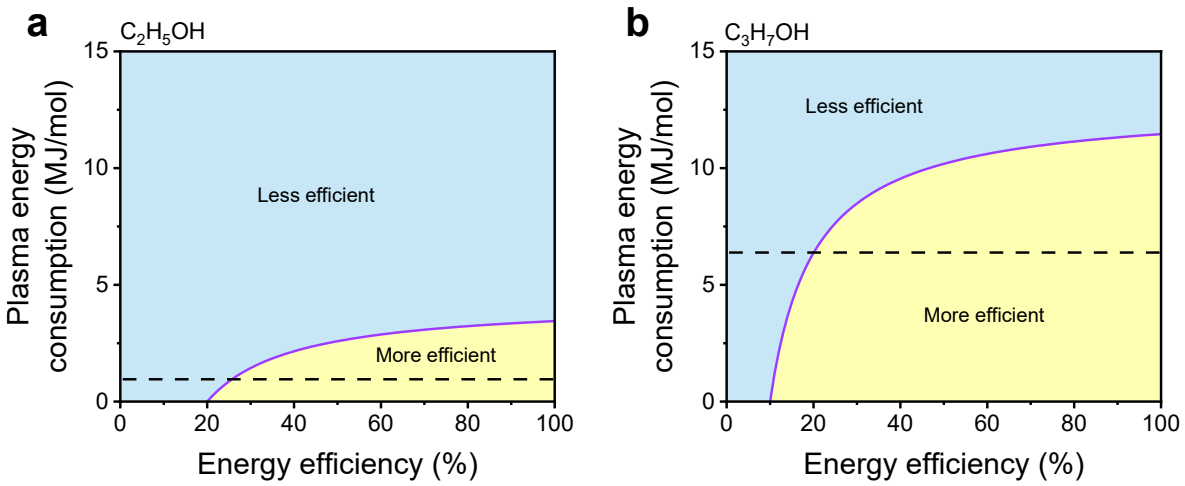
Supplementary Fig. 63 | *In situ* spectroscopic investigation of surface intermediates in plasma-activated CO_2 electroreduction. a-b, *In situ* Raman spectra were collected to probe adsorbed reaction intermediates on Cu catalysts in plasma-activated CO_2 electroreduction collected in the range of (**a**) 200-1100 and (**b**) 1100-2100 cm^{-1}. Spectra were acquired under applied potentials ranging from 0.03 to -0.27 V (vs. RHE, before IR compensation). A mixed CO_2+He gas feed with a ratio of 4:1 was supplied during all measurements. 1 M KOH solution was used as electrolyte. The laser source was 633 nm.



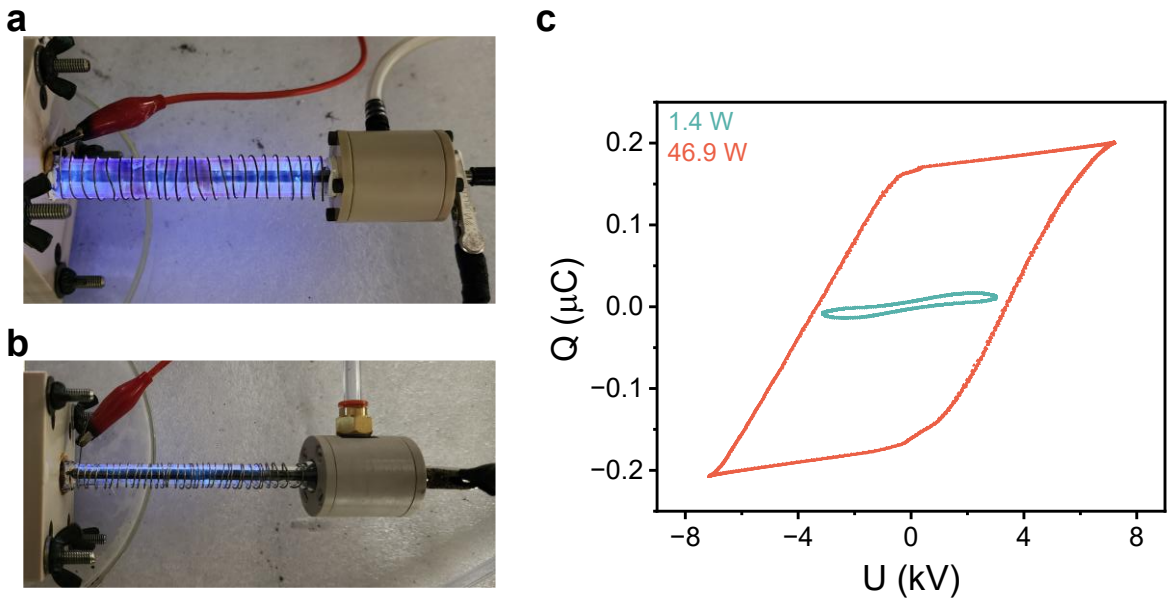
599

600 **Supplementary Fig. 64 | *In situ* spectroscopic investigation of surface intermediates in plasma-**
601 **activated CO electroreduction. a-b,** *In situ* Raman spectra were collected to probe adsorbed reaction
602 intermediates on Cu catalysts in plasma-activated CO electroreduction collected in the range of (**a**) 200-
603 1100 and (**b**) 1100-2100 cm^{-1}. Spectra were acquired under applied potentials ranging from 0.03 to -
604 0.87 V (vs. RHE, before IR compensation). A mixed CO+He gas feed with a ratio of 3:2 was supplied
605 during all measurements. 1 M KOH solution was used as electrolyte. The laser source was 633 nm.

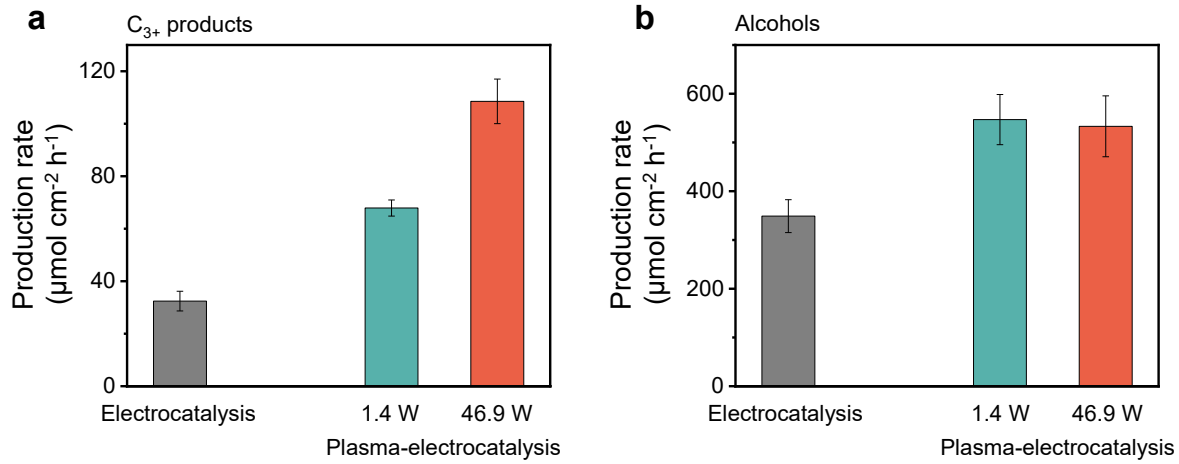
606



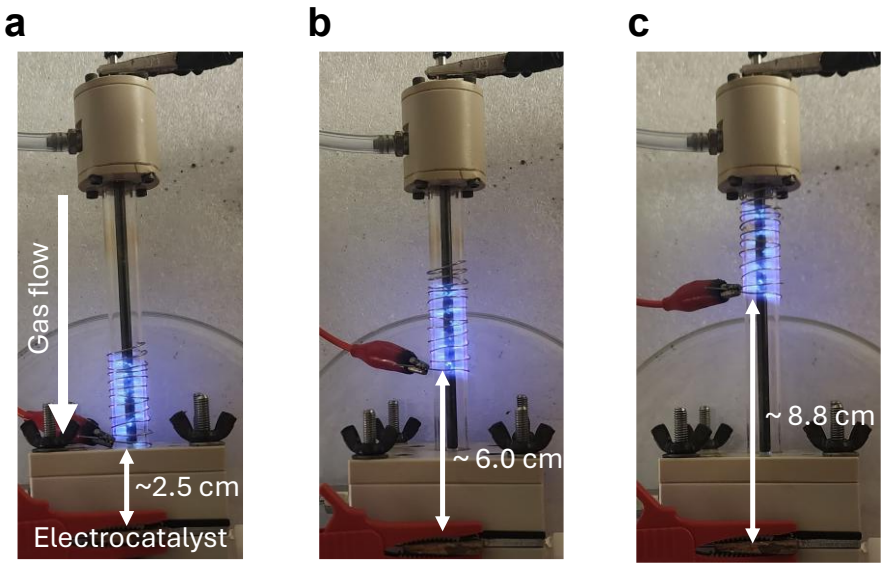
Supplementary Fig. 65 | Evaluation of overall energy efficiency of the plasma-electrocatalysis process considering the additional energy overhead introduced by plasma activation. a-b, The analysis was performed for two alcohols: (**a**) C_2H_5OH and (**b**) C_3H_7OH. The blue region indicates conditions where the overall process becomes less energy efficient due to the extra energy consumption of plasma activation, assuming that the overall plasma-electrochemical reaction operates at the corresponding energy efficiency. In contrast, the yellow region represents cases where plasma coupling enhances energy efficiency of the overall electrochemical reactions, making the overall plasma-electrocatalysis process more energy efficient compared to current electrocatalysis-only conversion technology (i.e., the plasma energy consumption is justified by the enhanced efficiency of product generation during electrocatalysis). The dashed lines represent the plasma energy consumption per unit product, calculated based on the C_2H_5OH and C_3H_7OH production rates reported in this work, assuming an active area of 10 cm^2 and a plasma power of 1.4 W. The underlying calculations used for this analysis compare energy consumption of electrocatalysis-only conversion ($\frac{\Delta G_{product}}{Current\ energy\ efficiency\ of\ product}$) and that of plasma-electrocatalysis ($\frac{\Delta G_{product}}{Enhanced\ energy\ efficiency\ (x)} + plasma\ energy\ consumption\ (y)$), where *Enhanced energy efficiency* is a variable that represents the overall energy efficiency for generating a given product using plasma-electrocatalysis, and $\Delta G_{product}$ is the theoretical reaction energy to generate a specific product.



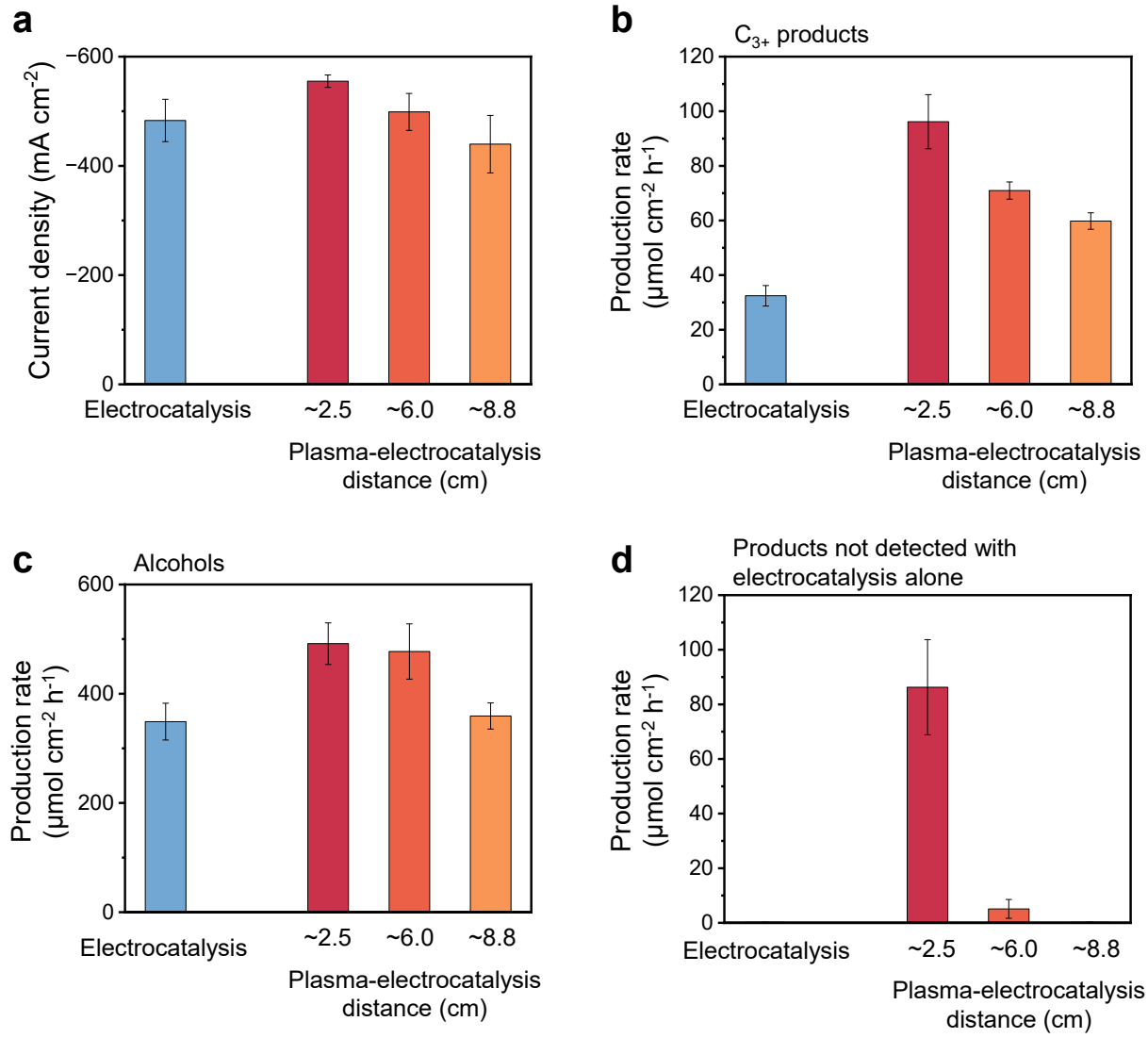
Supplementary Fig. 66 | Reduction of plasma power consumption via plasma reactor discharge gap engineering. a, Photograph of the plasma reactor configuration used for results reported in the main text figures, featuring a discharge gap of 3 mm. **b,** Photograph of the modified plasma reactor in which the quartz tube for the plasma region was thinned to reduce the discharge gap to 1 mm. **c,** Lissajous plots for power measurement, corresponding to energy consumption of 46.9 W for the 3 mm discharge gap and 1.4 W for the 1 mm discharge gap. A mixed gas feed of CO_2 (30 mL min^{-1}), CO (10 mL min^{-1}), and He (10 mL min^{-1}) was supplied. The applied alternating voltage had a frequency of 19.1 kHz.



Supplementary Fig. 67 | Evaluation of electrocatalytic CO_2 + CO conversion using varying plasma reactor discharge gap. a-b, Electrocatalytic conversion of plasma-activated CO_2 + CO was evaluated using a 1 mm discharge gap (1.4 W plasma) and 3 mm discharge gap (46.9 W plasma). Production rates for (**a**) C_{3+} products and (**b**) alcohols. C_{3+} products include C_3H_6, C_3H_7OH, C_3H_8, CH_3COCH_3, and C_4H_{10}. Alcohols include CH_3OH, C_2H_5OH, and C_3H_7OH. Electrocatalysis-only conversion was used as a control. A constant potential of -2 V (vs. RHE, before IR compensation) was applied. 1 M KOH was used as an electrolyte. A mixed gas feed of CO_2 (30 mL min^{-1}), CO (10 mL min^{-1}), and He (10 mL min^{-1}) was supplied. Each data point represents the mean and standard deviation of at least three independent measurements.



Supplementary Fig. 68 | Distance-dependent plasma coupling effects in plasma-electrocatalytic CO_2 + CO conversion. a-c, Plasma-electrocatalytic coupling was systematically modulated by adjusting the position of the ground coil, thereby controlling the transport distance for plasma species between the plasma and the GDE. The distance from the plasma end to the GDE was set to (**a**) ~2.5 cm, (**b**) ~6.0 cm, and (**c**) ~8.8 cm. A mixed gas feed of CO_2 (30 mL min^{-1}), CO (10 mL min^{-1}), and He (10 mL min^{-1}) was supplied during all measurements.



Supplementary Fig. 69 | Dependence of CO_2 + CO conversion on plasma-electrocatalyst distance. **a-d,** Effect of the distance between the end of the plasma and the GDE on reaction activity and product generation rates. Plasma-electrocatalytic conversion was compared with electrocatalysis-only as a control. (**a**) Total current density. Production rates for (**b**) C_{3+} products, (**c**) alcohols, and (**d**) products not detected with electrocatalysis alone. C_{3+} products include C_3H_6, C_3H_7OH, C_3H_8, CH_3COCH_3, and C_4H_{10}. Alcohols include CH_3OH, C_2H_5OH, and C_3H_7OH. Products not detected with electrocatalysis alone include CH_3OH, C_2H_2, C_2H_6, C_3H_8, and C_4H_{10}. 30 ml min^{-1} CO_2 + 10 ml min^{-1} CO + 10 ml min^{-1} He was supplied. A 400 nm thick Cu film on PTFE membrane was used as an electrode, with the PTFE side facing the plasma, and the Cu film contacting the electrolyte. 1 M KOH aqueous solution was used as an electrolyte. Constant potential of -2.0 (V vs RHE, before IR compensation) was applied for 1 hour. Each data point represents the mean and standard deviation of three independent measurements.

Supplementary Table 1 | Comparison between our work and previous research on electrocatalytic conversion of CO_2/CO to C_{3+} products. FE and partial *J* in this work were calculated assuming products were generated from CO_2. For studies where cathodic EE was not explicitly reported, the values were calculated based on the potential and FE provided in the corresponding works.

Catalysts	Reactant	Products	Reactor type	FE (%)	Cathodic EE (%)	Partial *J* (mA cm^{-2})	Reference
Cu GDE	CO_2 + CO	C_3H_6, C_3H_8, CH_3COCH_3, C_3H_7OH, C_4H_{10}	Plasma-coupled flow reactor	15.4±1.5 (estimated)	~6 (estimated)	53.2±4.4 (estimated)	This work
Ni phosphide	CO_2	Methylglyoxal 2,3-furandiol	H-cell	71	-	< 0.5	[27]
CuOD-Cu	CO_2	C_3H_7OH	H-cell	17.9	<10	8.51	[28]
Ag-Ru-Cu	CO	C_3H_7OH	Membrane electrode assembly	36±3	24	108	[29]
Cu nanocavity	CO	C_3H_7OH	Flow reactor	21±1	~10	7.8±0.5	[30]
Fragmented Cu	CO	C_3H_7OH	Flow reactor	20	10.8 (full cell)	8.5	[31]
Cu_2S-Cu-V	CO_2	C_3H_7OH	H-cell	7	~18	28	[32]
Metal ion cycled Cu	CO_2	C_3H_7OH	H-cell	14	~20	15	[33]
Cu_3N-derived Cu	CO_2	C_3H_7OH, allyl alcohol	H-cell	12.2	~8	2.3	[34]
2D Cu nanosheet	CO	C_3H_7OH	Flow reactor	9.8	~1	0.98	[35]
Ni phosphate-derived Ni	CO_2	C_3-C_6 products	H-cell	6.5	~1	0.9	[36]
$Au_{0.02}Cu_{0.98}$	CO_2	C_3H_7OH	H-cell	18.2±0.6	~17	16.6	[37]
Pb-rich Cu	CO	C_3H_7OH	Flow reactor	47±3	25, 18 (full cell)	38±2	[38]
LSN-Cu	CO	C_3H_7OH	Flow reactor	54	29	71	[39]
Sn-Cu	CO	C_3H_7OH	Membrane electrode assembly	47	24 (full cell)	70.5	[40]
ZnSnAuBiCuO	CO	C_3H_7OH	Flow reactor	47	20.9	47	[41]

Supplementary Table 2 | Comparison between our work and previous research on electrocatalytic conversion of CO_2/CO to alcohols. FE and partial *J* in this work were calculated assuming products were generated from CO_2. For studies where cathodic EE was not explicitly reported, the values were calculated based on the potential and FE provided in the corresponding works.

Catalysts	Reactant	Products	Reactor type	FE (%)	Cathodic EE(%)	Partial *J* (mA cm^{-2})	Reference
Cu GDE	CO_2 + CO	CH_3OH, C_2H_5OH, and C_3H_7OH	Plasma-coupled flow reactor	48.1±0.9 (estimated)	23.4 (estimated)	199.2±14.7 (estimated)	This work
Supersaturated Ag-Cu	CO_2	C_2H_5OH	Membrane electrode assembly	40.4	14.4 (full cell)	51.6	[42]
NGQ/Cu-nr	CO_2	C_2H_5OH and C_3H_7OH	Flow reactor	52.4	~12	147.8	[43]
Cu-Zn film	CO_2	C_2H_5OH	Flow reactor	25	11 (full cell)	93	[44]
Functionalized Ag-Cu	CO_2	C_2H_5OH	Flow reactor	16.5	~17	54.5	[45]
Cu/BaO	CO_2	C_2H_5OH and C_3H_7OH	Flow reactor	61	30	244	[46]
$Ag_{0.14}/Cu_{0.86}$	CO_2	C_2H_5OH	Flow reactor	41.4	~20	103.5	[47]
N-C/Cu	CO_2	C_2H_5OH and C_3H_7OH	Flow reactor	52±1	31	156	[48]
Defect-site-rich Cu	CO_2	C_2H_5OH and C_3H_7OH	Flow reactor	~60	~17	~100	[49]
FeTPP[Cl]-Cu	CO_2	C_2H_5OH	Flow reactor	41	~23	124	[50]
Cu/C-0.4	CO_2	C_2H_5OH	Rotating disk electrode	91	~30	1.1	[51]
SnS_2/Sn_1-O_3G	CO_2	C_2H_5OH	H-cell	82.5	~27	17.8	[52]
Im-MoP	CO_2	C_2H_5OH	Flow reactor	77.4	63.3	54.9	[53]
Cu_2O/Ag	CO_2	C_2H_5OH	Flow reactor	40.8	22.3	326.4	[54]
CoPc	CO	CH_3OH	Flow reactor	84	39.5	20	[55]
Cu/Cu_2O	CO	C_2H_5OH	Flow reactor	68.8	40.9	111	[56]

Supplementary Table 3 | Maximum cathodic conversion efficiency of ground state CO_2 (plasma off), plasma-activated CO_2 at different powers, and 46.9 W plasma-activated CO_2+CO for C_2H_5OH and C_3H_7OH production. Energy efficiency was calculated assuming products were generated from CO_2. Efficiency (*Energy efficiency*$_{cathodic\ half\text{–}cell}$) was calculated based on equation (11):

$$Energy\ efficiency_{cathodic\ half-cell} = \frac{1.23-E_i^{\circ}}{1.23-E_{applied}} \times Faradaic\ efficiency_i \quad (11)$$

where E_i° is the standard reduction potential for the cathodic reaction i, and $E_{applied}$ is the applied cathodic potential.

Half-cell conversion efficiency / Reactant	C_2H_5OH (%)	C_3H_7OH (%)
CO_2 (plasma off)	16.1	1.9
CO_2 (12.0 W plasma on)	16.9	2.3
CO_2 (28.7 W plasma on)	15.8	2.7
CO_2 (42.3 W plasma on)	12.6	2.7
CO_2+CO (46.9 W plasma on)	18.1	5.3

Supplementary Table 4 | Molar fraction of vibrationally excited CO_2/CO molecules. Molar fraction of vibrationally excited CO_2 and CO molecules, calculated at the end of the last microdischarge after 100 µs, based on the ratio of excited state number densities of CO + CO_2, over the total number density of gas molecules, for different CO_2:CO ratios and vibrational temperatures (which define the extent of vibrational excitation, assuming a Boltzmann vibrational distribution). Calculated with a pseudo-1D model, thus not accounting for mass transport and interactions with the gas diffusion electrode, hence only providing qualitative estimates.

CO_2:CO ratio	**Vibrational Temperature (K)**	**Total density (m^{-3})**	**Excited density (m^{-3})**	**Molar fraction of vibrational excitation**
10:90	300	2.45×10^{25}	7.56×10^{20}	3.09×10^{-5}
5:95	500	1.47×10^{25}	2.92×10^{22}	1.99×10^{-3}
2:98	760	9.66×10^{24}	1.64×10^{23}	1.7×10^{-2}
1:99	900	8.15×10^{24}	2.63×10^{23}	3.22×10^{-2}
0:100	1200	6.12×10^{24}	4.69×10^{23}	7.68×10^{-2}

Supplementary Table 5 | Rate coefficients added or modified in this work compared to previous research.[11] The electron-impact processes, described by energy-dependent cross sections and the electron energy distribution function (EEDF), are taken from specific databases within the LxCat database, as detailed in the reference column. M is a colliding partner, which includes all neutral species, unless specified differently.

Reaction	Rate coefficients (s^{-1}, $cm^3\ s^{-1}$, $cm^6\ s^{-1}$, for unimolecular, bimolecular and trimolecular reactions, respectively)	Reference
$e + CO_2 \rightarrow 2e + CO_2^+$	EEDF[a]	[57]
$e + CO_2 \rightarrow 2e + CO + O^+$	EEDF	[57]
$e + CO_2 \rightarrow 2e + O + CO^+$	EEDF	[57]
$e + CO_2 \rightarrow 2e + O_2 + C^+$	EEDF	[57]
$e + CO_2 \rightarrow 2e + C + O_2^+$	EEDF	[57]
$e + C \rightarrow 2e + C^+$	EEDF	[58]
$e + He \rightarrow e + He$	EEDF	[59]
$e + He \rightarrow 2e + He^+$	EEDF	[59]
$e + He \rightarrow e + He(S)$	EEDF[b]	[59]
$e + He \rightarrow e + He(T)$	EEDF[b]	[59]
Electronic relaxation		
$CO(a^3\pi) + He \rightarrow CO + He$	1×10^{-14}	[60]
$O(^1D) + He \rightarrow O + He$	3×10^{-16}	[60]
$O_2(a^1\Delta_g) + He \rightarrow O_2 + He$	$8 \times 10^{-21}\ (T_g/300)^{0.5}$	[61]
$O_2(b^1\Sigma_g^+) + He \rightarrow O_2(a^1\Delta_g) + He$	$1 \times 10^{-17}\ (T_g/300)^{0.5}$	[61]
$He(S) \rightarrow He$	1.27×10^{-4}	[62]
$He(S) + M \rightarrow He + M$	8×10^{-15}	[63]
Penning ionization		
$He(T) + CO \rightarrow e + He + CO^+$	9.4272×10^{-11}	[64]
$He(T) + O_2 \rightarrow e + He + O_2^+$	6.39×10^{-11}	[65]
$He(T) + CO_2 \rightarrow e + He + CO_2^+$	6.9×10^{-10}	[63]
Penning dissociation		
$He(T) + CO \rightarrow C + O + He$	3.93×10^{-12}	[64]
$He(T) + O_2 \rightarrow 2O + He$	4.548×10^{-11}	[65]
Thermal chemistry		
$2O + He \leftrightarrow O_2 + He$	1×10^{-33}	[61]
$2O + He \leftrightarrow O_2(a^1\Delta_g) + He$	9.88×10^{-35}	[61]
$O + O_2 + He \leftrightarrow O_3 + He$	$3.4 \times 10^{-34}\ (T_g/300)^{-1.2}$	[61]
$O + O_2 + O_3 \leftrightarrow 2O_3$	$2.3 \times 10^{-35}\ e^{(-1057/Tg)}$	[61]
$C + CO + M \leftrightarrow C_2O + M$[c]	1.5×10^{-31}	[66]
$C + CO + He \leftrightarrow C_2O + He$	6.3×10^{-32}	[67]
$C + CO \leftrightarrow C_2 + O$	$3.32 \times 10^{-7}\ (1/T_g)\ e^{(-58000/Tg)}$	[68]
$2C + M \leftrightarrow C_2 + M$	$2.76 \times 10^{-32}\ T_g^{-0.5}$	[63]
$C + C_2O \leftrightarrow C_2 + CO$	$7.47 \times 10^{-13}\ T_g^{0.5}$	[69]
$2C_2 \leftrightarrow C_3 + C$	$8.3 \times 10^{-13}\ T_g^{0.5}$	[63]
$2C_2 + M \leftrightarrow C_4 + M$	$2.76 \times 10^{-21}\ T_g^{-3}$	[14]
$C_2 + O_2 \leftrightarrow CO_2 + C$	6.6×10^{-13}	[70]

$C_2 + O_2 \leftrightarrow 2CO$	1.83×10^{-12}	[70]
$C_2O + O \rightarrow 2CO$	1.2×10^{-11}	[71]
$C_2O + CO(a^3\pi) \rightarrow 2CO + C$	2×10^{-9}	[71]
$C_2O + O_2 \rightarrow CO + CO_2$	3.3×10^{-13}	[72]
$C_2O + C_2O \leftrightarrow C_2 + 2CO$	$9.96 \times 10^{-12} e^{(-2770/Tg)}$	[69]
$C_2O + C_2 \leftrightarrow C_3 + CO$	$7.47 \times 10^{-13} T_g^{0.5}$	[69]
$C_2O + C_3 \leftrightarrow C_4 + CO$	$7.47 \times 10^{-13} T_g^{0.5}$	[69]
$C_3O_2 + M \leftrightarrow C_2O + CO + M$	$2.49 \times 10^{-9} e^{(-29470/Tg)}$	[69]
$C_3O_2 + C \leftrightarrow C_2 + 2CO$	$5.98 \times 10^{-10} e^{(-2770/Tg)}$	[69]
$C_3O_2 + C_2 \leftrightarrow C_3 + 2CO$	$7.47 \times 10^{-13} T_g^{0.5} e^{(-10200/Tg)}$	[69]
$C_3O_2 + C_3 \leftrightarrow C_4 + 2CO$	$7.47 \times 10^{-13} T_g^{0.5} e^{(-10200/Tg)}$	[69]
$C_3O_2 + O \leftrightarrow 3CO$	5.2×10^{-13}	[73]
$C_3O_2 + O \leftrightarrow C_2O + CO_2$	4.1×10^{-14}	[73]
$C_3 + M \leftrightarrow C_2 + C + M$	$6.64 \times 10^{-8} e^{(-75480/Tg)}$	[14]
$C_3 + O \leftrightarrow C_2 + CO$	$5 \times 10^{-11} T_g^{0.5}$	[70]
$C_3 + O_2 \leftrightarrow C_2 + CO + O$	1×10^{-12}	[70]
$C_3 + O_2 \leftrightarrow C_2 + CO_2$	1×10^{-12}	[70]
$C_4 + O \leftrightarrow C_3 + CO$	$5 \times 10^{-11} T_g^{0.5}$	[70]
$C_4 \rightarrow 4Cs$	8×10^{3}	[14]
Ion-neutral reactions		
$O^- + He(S, T) \rightarrow O + He + e$	3×10^{-10}	[61]
$O_2^- + He(S, T) \rightarrow O_2 + He + e$	3×10^{-10}	[61]
$O_3^- + He(S, T) \rightarrow O_3 + He + e$	3×10^{-10}	[61]
$O_4^- + He(S, T) \rightarrow 2O_2 + He + e$	3×10^{-10}	[61]
$CO_3^- + He(S, T) \rightarrow CO_2 + O + He + e$	3×10^{-10}	[61]
$CO_4^- + He(S, T) \rightarrow CO_2 + O_2 + He + e$	3×10^{-10}	[61]
$He^+ + O \leftrightarrow He + O^+$	$5 \times 10^{-11} (T_g/300)^{0.5}$	[61]
$He^+ + O_2 \leftrightarrow He + O + O^+$	$1.07 \times 10^{-9} (T_g/300)^{0.5}$	[74]
$He^+ + O_2 \leftrightarrow He + O_2^+$	$3.3 \times 10^{-11} (T_g/300)^{0.5}$	[61]
$He^+ + O_3 \leftrightarrow He + O_2 + O^+$	$1.07 \times 10^{-9} (T_g/300)^{0.5}$	[61]
$He^+ + C \leftrightarrow He + C^+$	$3.25 \times 10^{-17} T_g^{0.968}$	[75]
$He^+ + CO \leftrightarrow He + C + O^+$	$1.4 \times 10^{-16} T_g^{-0.5}$	[70]
$He^+ + CO \leftrightarrow He + O + C^+$	1.4×10^{-9}	[76]
$He^+ + C_2O \leftrightarrow He + CO + C^+$	$1 \times 10^{-9} (T_g/300)^{-0.5}$	[70]
$He^+ + CO_2 \leftrightarrow He + CO_2^+$	5×10^{-12}	[74]
$He^+ + CO_2 \leftrightarrow He + O + CO^+$	7.7×10^{-10}	[74]
$He^+ + CO_2 \leftrightarrow He + CO + O^+$	1.8×10^{-10}	[74]
$He^+ + CO_2 \leftrightarrow He + O_2 + C^+$	4×10^{-11}	[74]
$He^+ + CO_2 \leftrightarrow He + C + O_2^+$	5×10^{-12}	[74]

[a]Includes ionization to electronically excited CO_2^+, with instantaneous relaxation to ground state CO_2^+

[b]Excitation to triplet (T) and singlet (S) states are lumped together

[c]M = all neutrals, except He

Supplementary References

1 Yang, L.-P *et al.* Copper–Carbon: An Efficient Catalyst for Oxygen Reduction. *ACS Appl. Energy Mater.* **2**, 6295-6301 (2019).

2 Jiang, Z. *et al.* Atomic interface effect of a single atom copper catalyst for enhanced oxygen reduction reactions. *Energy & Environ. Sci.* **12**, 3508-3514 (2019).

3 Wang, X. *et al.* Mechanistic reaction pathways of enhanced ethylene yields during electroreduction of CO_2–CO co-feeds on Cu and Cu-tandem electrocatalysts. *Nat. Nanotech.* **14**, 1063-1070 (2019).

4 Möller, T. *et al.* A CO_2 electrolyzer tandem cell system for CO_2-CO co-feed valorization in a Ni-NC/Cu-catalyzed reaction cascade. *Nat. Commun.* **14**, 5680 (2023).

5 Obi, D. *et al.* Review of recent process developments in the field of carbon dioxide (CO_2) capture from power plants flue gases and the future perspectives. *Int. J. Sustain. Energy* **43**, 2317137 (2024).

6 Biondo, O *et al.* Coupling a CO_2 plasma with a carbon bed: The closer the better. *Chem. Eng. J.* **507**, 160190 (2025).

7 O'Modhrain, C. *et al.* Post-plasma carbon bed design for CO_2 conversion: Does size and insulation matter? *J. Energy Chem.* **104**, 312-323 (2025).

8 Van 't Veer, K. *et al.* Plasma-catalytic ammonia synthesis in a DBD plasma: role of microdischarges and their afterglows. *J. Phys. Chem. C* **124**, 22871-22883 (2020).

9 Fridman, A. *Plasma Chem*. (Cambridge university press, 2008).

10 Mehta, P. *et al.* Catalysis Enabled by Plasma Activation of Strong Chemical Bonds: A Review. *ACS Energy Lett.* **4**, 1115-1133 (2019).

11 Tsonev, I. *et al.* Simulation of a pulsed CO_2 plasma based on a six-temperature energy approach. *Plasma Sources Sci. Tech.* (2025).

12 Billing, G. D. & Cacciatore, M. Semiclassical calculation of vibrational relaxation of CO colliding with 4He and 3He. *Chem. Phys. Lett.* **86**, 20-25 (1982).

13 Kozák, T. & Bogaerts, A. Splitting of CO_2 by vibrational excitation in non-equilibrium plasmas: a reaction kinetics model. *Plasma Sources Sci. Tech.* **23**, 045004 (2014).

14 Kruse, T. & Roth, P. Kinetics of C_2 reactions during high-temperature pyrolysis of acetylene. *J. Phys. Chem. A* **101**, 2138-2146 (1997).

15 Girard-Sahun, F. *et al.* Carbon bed post-plasma to enhance the CO_2 conversion and remove O_2 from the product stream. *Chem. Eng. J.* **442**, 136268 (2022).

16 McBride, B. J. *NASA Glenn coefficients for calculating thermodynamic properties of individual species*. (National Aeronautics and Space Administration, John H. Glenn Research Center (2002).

17 Mahdikia, H., Brüser, V., Schiorlin, M. & Brandenburg, R. CO_2 Dissociation in Barrier Corona Discharges: Effect of Elevated Pressures in CO_2/Ar Mixtures. *Plasma Chem. Plasma Process.* **43**, 2035-2063 (2023).

18 Ozkan, A. *et al.* The influence of power and frequency on the filamentary behavior of a flowing DBD—application to the splitting of CO_2. *Plasma Sources Sci. Tech.* **25**, 025013 (2016).

19 Odeyemi, F. *et al.* Non Equilibrium Plasma Assisted Conversion of Fossil Fuels without CO_2 Release. *Green and Sustain. Chem.* **2**, 18999 (2012).

20 Kobe, K. A. & Reyerson, L. H. The Catalytic Hydrogenation of Carbon Suboxide. *J. Phys. Chem.* **35**, 3025-3035 (1931).

21 Odziomek, M. *et al.* "Red Carbon": A Rediscovered Covalent Crystalline Semiconductor. *Adv. Mater.* **34**, 2206405 (2022).

22 Geiger, R. & Staack, D. Analysis of solid products formed in atmospheric non-thermal carbon monoxide plasma. *J. Phys. D: Appl. Phys.* **44**, 274005 (2011).

23 Li, X. *et al.* Electrochemical CO_2 reduction to liquid fuels: Mechanistic pathways and surface/interface engineering of catalysts and electrolytes. *Innovation* **6** (2025).

24 Zhu, P. & Wang, H. High-purity and high-concentration liquid fuels through CO_2 electroreduction. *Nat. Catal.* **4**, 943-951 (2021).

25 Fan, L. *et al.* Electrochemical CO_2 reduction to high-concentration pure formic acid solutions

in an all-solid-state reactor. *Nat. Commun.* **11**, 3633 (2020).

26 De Meyer, R. *et al.* Importance of plasma discharge characteristics in plasma catalysis: Dry reforming of methane vs. ammonia synthesis. *Chem. Eng. J.* **488**, 150838 (2024).

27 Calvinho, K. U. D. *et al.* Selective CO_2 reduction to C_3 and C_4 oxyhydrocarbons on nickel phosphides at overpotentials as low as 10 mV. *Energy & Environ. Sci.* **11**, 2550-2559 (2018).

28 Long, C. *et al.* Regulating reconstruction of oxide-derived Cu for electrochemical CO2 reduction toward n-propanol. *Sci. Adv.* **9**, eadi6119 (2023)

29 Wang, X. *et al.* Efficient electrosynthesis of n-propanol from carbon monoxide using a Ag–Ru–Cu catalyst. *Nat. Energy* **7**, 170-176 (2022).

30 Zhuang, T.-T. *et al.* Copper nanocavities confine intermediates for efficient electrosynthesis of C_3 alcohol fuels from carbon monoxide. *Nat. Catal.* **1**, 946-951 (2018).

31 Pang, Y. *et al.* Efficient electrocatalytic conversion of carbon monoxide to propanol using fragmented copper. *Nat. Catal.* **2**, 251-258 (2019).

32 Zhuang, T.-T. *et al.* Steering post-C–C coupling selectivity enables high efficiency electroreduction of carbon dioxide to multi-carbon alcohols. *Nat. Catal.* **1**, 421-428 (2018).

33 Jiang, K. *et al.* Metal ion cycling of Cu foil for selective C–C coupling in electrochemical CO_2 reduction. *Nat. Catal.* **1**, 111-119 (2018).

34 Ebaid, M. *et al.* Production of C_2/C_3 Oxygenates from Planar Copper Nitride-Derived Mesoporous Copper via Electrochemical Reduction of CO_2. *Chem. Mater.* **32**, 3304-3311 (2020).

35 Luc, W. *et al.* Two-dimensional copper nanosheets for electrochemical reduction of carbon monoxide to acetate. *Nat. Catal.* **2**, 423-430 (2019).

36 Zhou, Y. *et al.* Long-chain hydrocarbons by CO_2 electroreduction using polarized nickel catalysts. *Nat. Catal.* **5**, 545-554 (2022).

37 Jeong, S. *et al.* Facet-Defined Dilute Metal Alloy Nanorods for Efficient Electroreduction of CO_2 to n-Propanol. *J. Am. Chem. Soc.* **146**, 4508-4520 (2024).

38 Niu, W. *et al.* Pb-rich Cu grain boundary sites for selective CO-to-n-propanol electroconversion.

787 *Nat. Commun.* **14**, 4882 (2023).
788 39 Niu, W. *et al.* High-efficiency C_3 electrosynthesis on a lattice-strain-stabilized nitrogen-doped
789 Cu surface. *Nat. Commun.* **15**, 7070 (2024).
790 40 Chen, Y. *et al.* Electrified synthesis of n-propanol using a dilute alloy catalyst. *Nat. Catal.* **8**,
791 239-247 (2025).
792 41 Wang, Y. *et al.* ZnSnAuBiCuO-Derived Electrocatalysts Rich in Grain Boundaries for CO
793 Reduction to n-Propanol. *J. Am. Chem. Soc.* **147**, 35471-35480 (2025).
794 42 Kim, J.-Y. *et al.* Selective hydrocarbon or oxygenate production in CO_2 electroreduction over
795 metallurgical alloy catalysts. *Nat. Synth.* **3**, 452-465 (2024).
796 43 Chen, C. *et al.* Highly Efficient Electroreduction of CO_2 to C_{2+} Alcohols on Heterogeneous
797 Dual Active Sites. *Angew. Chem. Int. Ed.* **59**, 16459-16464 (2020).
798 44 Baek, Y. *et al.* Electrochemical carbon dioxide reduction on copper–zinc alloys: ethanol and
799 ethylene selectivity analysis. *J. Mater. Chem. A* **10**, 9393-9401 (2022).
800 45 Wu, H. *et al.* Improved electrochemical conversion of CO_2 to multicarbon products by using
801 molecular doping. *Nat. Commun.***12**, 7210 (2021).
802 46 Xu, A. *et al.* Copper/alkaline earth metal oxide interfaces for electrochemical CO_2-to-alcohol
803 conversion by selective hydrogenation. *Nat. Catal.* **5**, 1081-1088 (2022).
804 47 Li, Y. C. *et al.* Binding Site Diversity Promotes CO_2 Electroreduction to Ethanol. *J. Am. Chem.*
805 *Soc.* **141**, 8584-8591 (2019).
806 48 Wang, X. *et al.* Efficient electrically powered CO_2-to-ethanol via suppression of deoxygenation.
807 *Nat. Energy* **5**, 478-486 (2020).
808 49 Gu, Z. *et al.* Efficient Electrocatalytic CO_2 Reduction to C_{2+} Alcohols at Defect-Site-Rich Cu
809 Surface. *Joule* **5**, 429-440 (2021).
810 50 Li, F. *et al.* Cooperative CO_2-to-ethanol conversion via enriched intermediates at molecule–
811 metal catalyst interfaces. *Nat. Catal.* **3**, 75-82 (2020).
812 51 Xu, H. *et al.* Highly selective electrocatalytic CO_2 reduction to ethanol by metallic clusters
813 dynamically formed from atomically dispersed copper. *Nat. Energy* **5**, 623-632 (2020).

814 52 Ding, J. *et al.* A tin-based tandem electrocatalyst for CO_2 reduction to ethanol with 80%
815 selectivity. *Nat. Energy* **8**, 1386-1394 (2023).
816 53 Esmaeilirad, M. *et al.* Efficient electrocatalytic conversion of CO_2 to ethanol enabled by
817 imidazolium-functionalized ionomer confined molybdenum phosphide. *Appl. Catal. B:*
818 *Environ.* **317**, 121681 (2022).
819 54 Wang, P. *et al.* Boosting electrocatalytic CO_2–to–ethanol production via asymmetric C–C
820 coupling. *Nat. Commun.* **13**, 3754 (2022).
821 55 Li, J. *et al.* Mechanism-guided realization of selective carbon monoxide electroreduction to
822 methanol. *Nat. Synth.* **2**, 1194-1201 (2023).
823 56 Ma, G. *et al.* A hydrophobic Cu/Cu_2O sheet catalyst for selective electroreduction of CO to
824 ethanol. *Nat. Commun.* **14**, 501 (2023).
825 57 Biagi database, www.lxcat.net, retrieved on January 28, 2025.
826 58 Wang, Y. *et al.* B-spline R-matrix-with-pseudostates calculations for electron-impact excitation
827 and ionization of carbon. *Phys. Rev. A* **87**, 012704 (2013).
828 59 Biagi-v7.1 database, www.lxcat.net, retrieved on January 28, 2025.
829 60 Cenian, A. *et al.* Modeling of plasma-chemical reactions in gas mixture of CO_2 lasers. II.
830 Theoretical model and its verification. *Contri. Plasma Phys.* **35**, 273-296 (1995).
831 61 Murakami, T. *et al.* Chemical kinetics and reactive species in atmospheric pressure helium–
832 oxygen plasmas with humid-air impurities. *Plasma Sources Sci. Tech.* **22**, 015003 (2012).
833 62 Hodgman, S. *et al.* Metastable helium: A new determination of the longest atomic excited-state
834 lifetime. *Phys. Rev. Lett.* **103**, 053002 (2009).
835 63 Saifutdinov, A. & Sysoev, S. Numerical simulation and experimental diagnostics of fast
836 electron kinetics and plasma parameters in a microhollow cathode discharges in helium. *Plasma*
837 *Sources Sci. Tech.* **32**, 114001 (2023).
838 64 Hurt, W. & Grable, W. Excitation Transfer and Penning Ionization Reactions between Helium
839 Metastables and Carbon Monoxide. *J. Phys. Chem.* **57**, 734-737 (1972).
840 65 Chang, R. *et al.* Assignment of rate constants to exit channels from quenching of He (23S)

metastable atoms. *Chem. Phys.* **35**, 201-214 (1978).

66 Gosse, F. *et al.* Study of mechanisms producing C_2*($A^3\Pi_g$) molecules in a CO afterglow. *Chem. Phys. Lett.* **13**, 557-560 (1972).

67 Husain, D. & Kirsch, L. Reactions of atomic carbon C (2^3P_J) by kinetic absorption spectroscopy in the vacuum ultra-violet. *Trans. Faraday Soc.* **67**, 2025-2035 (1971).

68 Park, C. *et al.* Review of chemical-kinetic problems of future NASA missions. II-Mars entries. *J. Thermophys. Heat. Transf.* **8**, 9-23 (1994).

69 Sojka, J. *et al.* Kinetic modeling of carbon suboxide thermal decomposition and formation of soot-like particles behind shock waves. *Combust. Sci. Tech.* **158**, 439-460 (2000).

70 Millar, T. J. *et al. The UMIST Database for Astrochemistry 2022*. *A&A* **682**, A109 (2024).

71 Grigorian, G. & Kochetov, I. Balance of CO molecules in the plasma of a sealed-off CO laser. *Plasma Phys. Rep.* **30**, 788-796 (2004).

72 Cenian, A. *et al.* Modeling of Plasma-Chemical Reactions in Gas Mixture of CO_2 Lasers I. Gas Decomposition in Pure CO_2 Glow Discharge. *Contrib. Plasma Phy.* **34**, 25-37 (1994).

73 Liuti, G. *et al.* Reaction of carbon suboxide with oxygen atoms and active nitrogen. *J. Am. Chem. Soc.* **89**, 5542-5545 (1967).

74 Anicich, V. *et al.* Product distributions for some thermal energy charge transfer reactions of rare gas ions. *J. Chem. Phys.* **67**, 4340-4350 (1977).

75 Glover, S. & Jappsen, A.-K. Star formation at very low metallicity. I. Chemistry and cooling at low densities. *Astrophys. J.* **666**, 1 (2007).

76 Bolden, R. *et al.* Measurements of thermal-energy ion-neutral reaction rate coefficients for rare-gas ions. J. Phys. B: At. Mol. Phys. **3**, 45 (1970).